Computational Insight into Homogeneous Organopalladium Catalysis

Thesis by
John A. Keith

In Partial Fulfillment of the Requirements
for the Degree of
Doctor of Philosophy

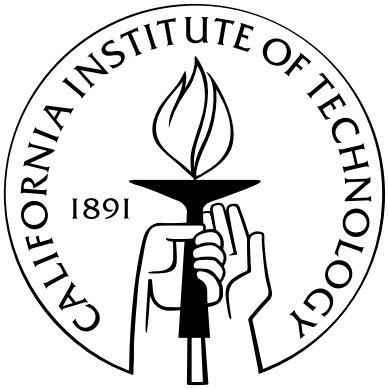

California Institute of Technology
Pasadena, California

2008
(Defended September 21, 2007)

Acknowledgements

My advisor, Bill Goddard, has been an extremely positive and helpful person during my time at Caltech. Besides *always* being a source for great insight, he is gifted at simultaneously encouraging, challenging, and teaching his students. My undergraduate research advisor at Wesleyan University, George Petersson, a colleague of Bill's dating back to the late 1960s, strongly directed me towards enrolling at Caltech to work for Bill. During a year between academic programs at the University of Minnesota, Don Truhlar, another colleague of Bill and George, further solidified my interest in computational simulations. I am fortunate to have worked for and learned from three brilliant, established, and orthogonally-minded quantum mechanics, all who are products of Caltech from the same decade.

Bill's group provided a professional yet nurturing environment where I could learn how to be a productive and competent scientist. Darryl Willick deserves much credit for maintaining the group's computers. My manager, Jonas Oxgaard, groomed me into a fearless quantum chemist, and my graduate colleagues, Robert (Smith) Nielsen and Julius Su gracefully helped me whenever I sought additional insight or direction. There is no project that I worked on that has not directly benefitted from one or more of those three individuals.

I also am thankful to Professor Brian Stoltz and members of his group, Doug Behenna, J.T. Mohr, Sandy Ma, Smaranda Marinescu, and other members of *"Team Tsuji,"* collaborators who were generous with their time and expertise during our collaboration in the Tsuji allylation project. Their devotion to chemistry and dedication to their craft is unparalleled.

As important as my professional colleagues have been to my research, my other friends at Caltech have been equally responsible for keeping me focused (and less focused) at times. Dan Fisher, a classmate and coworker since our time at Wesleyan, and Victor Kam, the virtuoso pianist and Perl coder, have been good friends with whom I spent many memorable hours studying, grading, and making music. Delores Bing, Justin Bois, Christie Canaria, Dave Ebner, Claire Jacobs, Jason Keith, Pete Kekenes-Huskey, James Maloney, Brian Leigh, Rachel Niemer, Christina Vizcarra, Don Walker, and Heather Wiencko highlight many of the genuinely helpful and encouraging people I fondly associate with my time at Caltech.

I thank also my parents, Philip and Sandy, for always taking the time to give encouraging advice while deftly balancing their roles as parents and occupations as teachers, and providing every possible opportunity to benefit my education. My siblings, George and Natasha, have always being available and helpful whenever I could possibly need them, particularly whenever I needed a comfortable place to stay during chemistry conferences.

Lastly, this work was supported with grants for our computational facilities from ARO-DURIP, ONR-DURIP, IBM-SUR, and the Beckman Institute. My graduate tenure has been supported by generous grants Chevron-Texaco Energy Research and Technology Company.

Abstract

An investigation of modern computational simulation techniques and their results in describing two notable organopalladium reactions are discussed. First, a methodology for computational quantum chemistry simulations of homogeneous catalysis is presented. We find that through careful consideration of electronic and thermodynamic energy contributions, practical methods are available to accurately study complicated reaction mechanisms and to make educated predictions about their chemistry. We apply this technique to develop the first full analysis of the Wacker Process, olefin oxidation by $PdCl_2$ catalysts, effectively uniting nearly 50 years of research into one mechanistic model. Key findings include the identification of competitive rate determining steps that are dependent on ion concentrations and the inaccessibility of β-hydride elimination during product formation. The second analysis addresses the unique performance of the enantioselective Tsuji-allylation reaction, a reaction the great potential in the fields of asymmetric catalysis and natural product synthesis. In this reaction, calculations point towards enantioselectivity determined after the rate determining step. Intriguingly, we find that C-C coupling is facile in a variant to canonical reductive elimination containing characteristics of both reductive cheletropic and Claisen rearrangements. Lastly, a model is presented to direct improved catalyst design. In total, this dissertation presents an outline for practical quantum chemical simulation of complicated and elaborate organopalladium reactions.

List of Figures

List of Tables

Contents

Chapter 1

Introduction

1.1 A Preface to this dissertation

To present the material herein as clearly as possible, this synopsis provides the reader with a summary of the chapters and their contents.

- **Chapter 1** provides a succinct overview to the physical and mathematical framework of the computational methods utilized in this work. Most of the information presented is simply a summary of standard material covered in most undergraduate physical chemistry courses and in 1^{st} year graduate quantum mechanics. Interested readers looking for greater depth are encouraged to pursue the following references:[1, 2, 3].

- **Chapter 2** describes technical details necessary to apply the information laid out in Chapter 1 to obtain accurate thermochemical data for species in gas and condensed phases. These details are followed by a summary of results that serve as a benchmark for the calculations that are utilized in this thesis.

- **Chapter 3** is thorough analysis of the olefin oxidation cycle of Wacker process reaction. This investigation resolves long-standing controversy with one of the most historically relevant industrial chemical processes of the 20th century. The chapter contains a summarized review of previous experimental and theoretical

findings. The author's own work in the context of previous experimental and theoretical work follows. Key results are that interpretations of previous experiments may not fully describe the true Wacker mechanism—specifically the identity of the *syn*-addition rate determining step and the ion concentration dependence on inner- and outer-sphere mechanisms is elaborated. Additionally, it is found that a widely accepted chemical process, β-hydride elimination from an alcohol functional group, is prohibitively high in energy and should be regarded as possible in only extraordinary circumstances.

- **Chapter 4** is a mechanistic overview of the enantioselective Tsuji allylation reaction with allyl-enol-carbonates. This investigation seeks to explain the reaction's effective and versatile performance that would not be explained with current understandings of previous literature. Notably, we determine that this reaction proceeds via an innersphere process. Key to this mechanism is the identification of a unique class of reductive elimination. The topology of the catalyst is then described to outline possible directions for improvements to the catalytic system.

- **Conclusions** provides a summary of this thesis and presents an outline for future work that naturally follows this work.

1.2 Why use computational chemistry?

Because it works![1]

[1]It is hoped that the reader is familiar with and finds humor in both the infamous chapter "Exceptions" in *The Conservation of Orbital Symmetry* by R.B. Woodward and R. Hoffmann, and the work of the cartoonist, Randall Munroe, (found at http://xkcd.com/54/) before judging the boldness of the author too severely.

1.3 Calculating microscopic properties

1.3.1 Electrons and nuclei, wavefunctions and Hamiltonians

The description of the reactivity of microscopic systems is a non-trivial process that usually requires quantum mechanics (QM) to treat the electronic structure of atoms and molecules. With information about the particles in the system along with necessary physical operators, it is possible to make chemical predictions. The Time-Independent Schrödinger equation (TISE), (1.1), returns the energy of a configuration of electrons and nuclei as the eigenvalue E. The positions of electrons and nuclei in *ab initio* methods are described with the molecular wavefunction, Ψ.

$$H\Psi = E\Psi \tag{1.1}$$

It is the Hamiltonian operator, H, (1.2), that contains the energy contributions necessary to calculate the energy of the system. Typically, we consider the Born-Oppenheimer approximation for the Hamiltonian to be the sum of four operators that calculate four energy terms: the electronic kinetic energies, nuclear-nuclear repulsions, electron-nuclear attractions, and electron-electronic repulsions.

$$H = -\sum_i \frac{1}{2}\nabla_i^2 + \sum_{A\neq B} \frac{Z_A Z_B}{r_{AB}} - \sum_i \sum_A \frac{Z_A}{r_{iA}} + \sum_{i\neq j} \frac{1}{r_{ij}} \tag{1.2}$$

Here, i and j are indexes for electrons, A and B are indexes for nuclei, ∇ is the Laplacian operator, Z is the atomic number of an atom, and r_{ab} is the distance between particles a and b.

The other component of the TISE is the wavefunction, Ψ. While one-electron systems can be solved exactly, the Heisenberg Uncertainty Principle complicates our understanding of multi-electron wavefunctions, and the TISE for multi-electron sys-

tems can only be solved approximately. While one cannot simply guess an exact wavefunction for a multi-electron system, there is a process to construct an approximate wavefunction and iteratively improve it. This process involves creating a trial wavefunction, ϕ, made up from a linear combination of orthonormal *atomic* basis functions, φ_i.

$$\phi = \sum_{i=1}^{N} a_i \varphi_i \tag{1.3}$$

The set of functions φ_i, (1.3), are called a 'basis set.' The larger the span of φ_i, the better ϕ is capable of modeling the exact Ψ.[2] Although we know neither the individual coefficients c_i nor the exact wavefunction Ψ, we use the Variational Principle of QM to make good approximations of ϕ, by modifying the coefficients c_i until we obtain a minimum energy result. That is, using the expression of the trial wavefunction in eq. (1.3), we can minimize the energy in the Secular equation with the requirement:

$$\frac{\int \phi H \phi d\mathbf{r}}{\int \phi^2 d\mathbf{r}} \geq E_0. \tag{1.4}$$

Combining eq. (1.3) with eq. (1.4) we solve

$$E = \frac{\int (\sum_i a_i \varphi_i) H (\sum_j a_j \varphi_j) d\mathbf{r}}{\int (\sum_i a_i \varphi_i)(\sum_j a_j \varphi_j) d\mathbf{r}} = \frac{\sum_{ij} a_i a_j \int \varphi_i H \varphi_j d\mathbf{r}}{\sum_{ij} a_i a_j \int \varphi_i \varphi_j d\mathbf{r}} = \frac{\sum_{ij} a_i a_j H_{ij}}{\sum_{ij} a_i a_j S_{ij}} \tag{1.5}$$

where H_{ij} and S_{ij} are the 'resonance' and 'overlap' integrals, respectively. Since we seek coefficients that yield the minimum value of E, one equates the derivative of eq. (1.5) with respect to all a_i to be zero. After doing so, one is left with N variables (a_i)

[2] Atoms containing many protons in their nuclei (such as transition metals) typically use an electronic core potential (ECP), which is a set of basis functions describing valence electrons combined with a set of analytic functions describing core electrons (implicitly tuned to treat relativistic effects). These ECPs are similarly treated as basis sets for the atoms they represent.

spanning over N equations that need to be satisfied according to

$$\sum_{i=1}^{N} a_i(H_{ki} - ES_{ki}) = 0 \tag{1.6}$$

for all k. This results in optimized coefficients:

$$\phi_j = \sum_{i=1}^{N} a_{ij}\varphi_i. \tag{1.7}$$

This process of optimizing coefficients for basis functions under a given criteria is generally referred to as a self-consistent field (SCF) calculation.

One requirement of multi-electron wavefunctions is that they be *antisymmetric*, meaning that whenever the coordinates of two electrons are exchanged, the sign of the wavefunction changes. Determinants make for practical representations of anti-symmetric wavefunctions, and the simplest form for an antisymmetric wavefunction is a Slater determinant of spin orbitals.

$$\Psi(\mathbf{x}_1, \mathbf{x}_2, \ldots, \mathbf{x}_N) = \frac{1}{\sqrt{N!}} \begin{vmatrix} \phi_1(\mathbf{x}_1) & \phi_2(\mathbf{x}_1) & \ldots & \phi_N(\mathbf{x}_1) \\ \phi_1(\mathbf{x}_2) & \phi_2(\mathbf{x}_2) & & \phi_N(\mathbf{x}_2) \\ & \vdots & \ddots & \vdots \\ \phi_1(\mathbf{x}_N) & \phi_2(\mathbf{x}_N) & \cdots & \phi_N(\mathbf{x}_N) \end{vmatrix} = \forall[\phi_1(\mathbf{x}_1)\phi_2(\mathbf{x}_2)\ldots\phi_N(\mathbf{x}_N)] \tag{1.8}$$

1.3.2 Hartree-Fock Theory

The Slater determinants mentioned in the previous section are particularly useful in representing Hartree-Fock (HF) wavefunctions—the first approximation and basis for most utilized quantum chemistry calculations. Of great practical importance is that HF wavefunctions can be optimized in a self-consistent manner carried out in basis set representations for ϕ with matrix algebra.

Solving the HF equations with N basis functions involves solving the secular equation for the roots, E_j, which are the energies of every electron in the system.

$$\begin{vmatrix} F_{11} - ES_{11} & F_{12} - ES_{12} & \dots & F_{1N} - ES_{1N} \\ F_{21} - ES_{21} & F_{22} - ES_{22} & \dots & F_{2N} - ES_{2N} \\ \vdots & \vdots & \ddots & \vdots \\ F_{N1} - ES_{N1} & F_{N2} - ES_{N2} & \dots & F_{NN} - ES_{NN} \end{vmatrix} = 0 \tag{1.9}$$

Since this equation is computing energies from basis functions within a molecular orbital (MO), one typically uses a notation where indexes for basis functions are referenced by lower-case Greek letters and references to MOs are by lower-case Roman letters. Thus, $F_{\mu\nu}$ are elements in the Fock matrix, $S_{\mu\nu}$ are elements in the overlap matrix, all of which need to be explicitly calculated. The Fock matrix elements involve three terms.[3]

$$F_{\mu\nu} = \left\langle \mu \left| -\frac{1}{2}\nabla^2 \right| \nu \right\rangle - \sum_{k}^{nuclei} Z_k \left\langle \mu \left| \frac{1}{r_k} \right| \nu \right\rangle + \sum_{\lambda\sigma} P_{\lambda\sigma}[(\mu\nu|\lambda\sigma) - \frac{1}{2}(\mu\lambda|\nu\sigma)] \tag{1.10}$$

The first term is a particular basis function's contribution to the one-electron kinetic energy. The second term is a particular basis function's contribution to the Coulombic energy between an electron and the nuclei. The last term considers electron-electron interactions, albeit in a very approximate way where each electron sees other electrons in the system as a static field of point charges. Also,

$$(\mu\nu|\lambda\sigma) = \iint \phi_\mu(1)\phi_\nu(1)\frac{1}{r_{12}}\phi_\lambda(2)\phi_\sigma(2)d\mathbf{r}(1)d\mathbf{r}(2)$$

[3]The reader should note that this representation specifies a wavefunction where the number of α and β spin electrons are equal and form a closed shell. In this case the wavefunction is called *restricted*. A different formulation of Hartree-Fock theory is required when the number of α and β spin electrons are not equal or are not perfectly matched into doubly occupied MOs in an open-shell. In this case an *unrestricted* wavefunction calculation is required.

represents the Coulombic interactions between all electrons, and

$$(\mu\lambda|\nu\sigma) = \iint \phi_\mu(1)\phi_\lambda(1)\frac{1}{r_{12}}\phi_\nu(2)\phi_\sigma(2)d\mathbf{r}(1)d\mathbf{r}(2)$$

represents exchange interactions between only same-spin electrons. In closed-shell systems, only half the total number of electrons in the system are the same spin (and thus the prefactor of 1/2 in (1.10)). The third term of (1.10) contains a special weighting factor that is an index of $\mathbf{P}$, the *density matrix*, an entity that describes the degree by which a particular basis function contributes to the many-electron wavefunction. At every cycle of orbital optimization, a new density matrix can be generated with

$$P_{\lambda\sigma} = 2\sum_{i}^{N} a_{\lambda i}a_{\sigma i}$$

where N is the number of occupied orbitals and coefficients $a_{\zeta i}$ are the normalized contribution of the basis function ζ to the MO i in a restricted wavefunction calculations. It follows that the integrity of each new density matrix improves as the coefficients of corresponding basis functions are improved. Once a new density matrix has reached a pre-defined set of criteria compared to the last calculated density matrix, the SCF calculation is said to have converged.

There are two points worth mentioning. First, SCF calculations under HF theory iteratively optimize orbitals in (1.7) under the pretext of minimizing the energy in (1.9). Under a different formalism, SCF procedures can be used to minimize other types of orbitals. Second, note that the last term of (1.10) contains two four-index integrals referring to μ, λ, ν, and σ. These four-indexes cause most computational calculations to scale as N^4, where N is the number of basis functions the four indexes are running over.[4]

[4]Fast-running software packages such as Jaguar[4], however, utilize a pseudospectral method enabling these four-index integrals to be solved numerically on a 3-D grid, effectively downscaling HF theory to an N^3 problem.

A benefit to the HF method is its pure *ab initio* nature where nothing in its design involves any empirical data for the purpose of obtaining a desired calculated result. Thus, errors in *ab initio* methods are the result of inherent errors of the theory itself rather than spurrious errors associated with poor parameterization of empirical data. For applications this is not necessarily a benefit nor a problem, however for method development, this is a very favorable characteristic.

A critical shortcoming of HF theory is its lack of *electronic correlation*, i.e., the treatment systems of electrons interacting with each other. This correlation is often times broken into a double-sided problem between *dynamical* and *non-dynamical* electronic correlation. Dynamical correlation refers to the impact of electronic energy due to electrons dynamically interacting with each other. Non-dynamical correlation refers to the impact of the energy of a real system being the combination of several accessible electronic states. HF theory treats neither (apart from small amounts of dynamical correlation due to electronic exchange) and is not accurate enough to make reliable chemical determinations, so other theories have been developed. The majority of these methods are under the umbrella of fully first-principle methods, *ab initio* wavefunction methods that incorporate no empirical data in their calculation.

1.3.3 Higher-level electronic correlation methods

- Perturbative approaches: The most commonly used higher-level wavefunction approach is perturbative Möller-Plesset (MPn) methods. These methods consider the whole of electronic correlation treatable through a perturbative approach where the HF energy is the first-order perturbative correction to an infinitely large solution to the exact electronic energy. Second-, third-, fourth-, (etc.) order corrections are found using MP2, MP3, MP4, (etc.) methods, and each is expected to systematically improve the calculated energy of a particular electronic state.

Perturbation theory is also the most efficient way to determine accurate energies for weakly-bound van der Waals complexes and hydrogen bonding. MP2 theory involves one extra correction to the HF energy, and thus typically scales as N^5. Each additional perturbation results in an extra factor of cost, and so high levels of perturbation theory are rarely considered in calculations of large molecules.

- Configuration-Interaction methods: An advanced treatment of dynamic correlation involves calculating energy contributions through explicit electronic excitations. Configuration Interaction (CI) calculations consider optimizing MOs under the field of excited electrons. These corrections are in terms of single- (S), double- (D), triple- (T), etc., electron excitations and treated with CIS, CISD, CISDT, etc., methods. These treatments provide quantitatively accurate results in excitation spectra, but are also expensive, scaling similarly to MPn methods.

  Related techniques go about solving dynamic correlation more completely with a single-reference Quadratic Configuration Interaction (QCI-) and Coupled Cluster (CC-) methods. These methods invoke mathematical formalisms to further improve calculation accuracy, however, these methods are equivalently costly.

- Multi-reference methods: Multi-Configuration (MC-), Complete Active Space (CAS-), and Generalized Valence Bond (GVB) approaches all treat electronic correlation by addressing non-dynamical correlation explicitly through solving for the electronic energy as a weighted average of two or more reference electronic states. The basis for MC- and CAS- methods involves computing the HF energy of several difference states, and so in that sense, the treatment of dynamical correlation is improved implicitly.

  Multi-reference methods are particularly useful in accurately calculating energies of systems with a multitude of low-lying MOs. There are several drawbacks

to these methods however. First, as already mentioned, these methods often times insufficiently treat dynamical correlation and yield inaccurate results (unless an approach such as CASPT2[5], which is a multi-reference method incorporating an MP2 treatment of dynamical correlation is used). Another problem with multi-reference methods is the complexity of the calculation in requiring the user to know which MOs are considered low lying. GVB methods treat this problem by identifying only the anti-bonding orbital pairs for bonding orbitals, and thus are the most practical of multi-reference methods.

As outlined, there are many possible theoretical approaches that can accurately treat complicated chemical systems involving electronic excitations, van der Waals complexes, and resonances between a multitude of different states. Unfortunately, all of these wavefunction approaches are computationally expensive, and the cost of quantitatively accurate calculations typically is prohibitively expensive for transition metals and large molecules.

1.3.4 Density Functional Theory

A dramatic shift in philosophy from the previous *ab initio* methods leads to the methods ubiquitously utilized in this thesis. One of the elegant differences between *ab initio* wavefunction theory and DFT theory is that while *ab initio* methods are built up from HF theory, an approximate theory insomuch as electron-electron interactions in the electronic Hamiltonian of the TISE can never be solved exactly; DFT *is an exact theory*, and some of its formulations are also *ab initio*.

Rather than seeking the solution of the TISE with molecular wavefunctions, DFT calculations solve energy functionals (functions of other functions) all in terms of the electron density of the molecule, ρ. Integration of ρ over all space will result in the

total number of electrons, N.

$$N = \int \rho(\mathbf{r}) d\mathbf{r}$$

In terms of ρ, the density functional energy equation is

$$E[\rho(\mathbf{r})] = T_{1e}[\rho(\mathbf{r})] + V_{\text{nuc-elec}}[\rho(\mathbf{r})] + V_{\text{elec-elec}}[\rho(\mathbf{r})] + \Delta T_{2e}[\rho(\mathbf{r})] + \Delta V_{\text{elec-elec}}[\rho(\mathbf{r})] \quad (1.11)$$

with the terms:

- $T_{1e}[\rho(\mathbf{r})]$ is the total kinetic energy of all electrons assuming they are not interacting with each other. Simply, this is equivalent to the sum of one-electron kinetic energies, $\frac{1}{2}\nabla^2$.

- $V_{\text{elec-nuc}}[\rho(\mathbf{r})]$ is the classical electronic-nuclear attraction in terms of ρ:

$$V_{\text{elec-nuc}}[\rho(\mathbf{r})] = \sum_{k}^{nuclei} \int \frac{Z_k}{|\mathbf{r} - \mathbf{r}_k|} \rho(\mathbf{r}) d\mathbf{r}.$$

- $V_{\text{elec-elec}}[\rho(\mathbf{r})]$ is the classical electron-electron interaction in terms of ρ:

$$V_{\text{elec-elec}}[\rho(\mathbf{r})] = \frac{1}{2} \iint \frac{\rho(r_1)\rho(r_2)}{|r_1 - r_2|} dr_1 dr_2.$$

- $\Delta T_{2e}[\rho(\mathbf{r})] + \Delta V_{\text{elec-elec}}[\rho(\mathbf{r})]$ is the sum of the inherent errors associated with treating electrons as non-interacting particles (as was done in the first term) plus all non-classical corrections to electron-electron repulsions (as was done in the third term). This sum, the only non-trivially simple expression in DFT, is typically cast into a single term to isolate the difficulties of calculating 2-electron exchange and correlation (xc) terms, $E_{xc}[\rho(r)]$.

It should be noted that all the prior terms have nothing about them that prevent their exact calculation. Additionally, it is possible to express (1.11) in terms of Kohn-Sham

orbitals, χ_i (non-equivalent analogs to MOs, ϕ_i) so that this energy is solvable in a self-consistent fashion similar to HF theory. Of chief practical importance is the ability to cast DFT into an SCF calculation similar to HF theory. In fact, the procedure for solving for DFT energies is the same as the procedure for solving HF energies, with the exception that (1.10) is replaced with (1.12).

$$K_{\mu\nu} = \left\langle \phi_\mu \left| -\frac{1}{2}\nabla^2 - \sum_k^{nuclei} \frac{Z_k}{|r - r_k|} + \int \frac{\rho(r')}{|r - r'|} dr' + V_{xc} \right| \phi_\nu \right\rangle \tag{1.12}$$

There are numerous treatments available for $E_{xc}[\rho(r)]$. The oldest and simplest treatment of E_{xc} is the local spin density approximation (LSDA). *ab initio* improvements on this treatment lead to a class of generalized gradient approximation (GGA) fuctionals. The label of *ab initio* becomes trickier to define when classifying DFT methods that incorporate combinations of LSDA, GGA, and even HF energies(!)[5] into their descriptions of E_{xc}. The treatment most popular in quantum chemistry calculations is the B3LYP exchange-correlation functional. B3LYP uses a scheme that incorporates a hodge-podge of five functionals scaled with three empirical parameters.

$$E_{xc}^{B3LYP} = (1 - a)E_x^{LSDA} + aE_x^{HF} + b\Delta E_x^B + (1 - c)E_c^{VWN} + cE_c^{LYP} \tag{1.13}$$

The terms of the B3LYP functional[6] are a combination of exchange functions: the local spin-density approximation (LSDA), exact exchange from HF theory[7] and gradient exchange corrections by Becke (B)[8], and a combination of correlation functionals by Vosko, Wilk, and Nussair (VWN)[9] and Lee, Yang, and Parr (LYP)[10]. Although functionally messy, the B3LYP hybrid functional is very popular for reasons that will be apparent in Chapter 2. Other DFT 'flavors' the author promotes are *ab initio* PBE[11, 12] and hybrid *m*PW1PW91[13].

[5] Actually, incorporation of HF exchange (which typically over-estimates exchange contributions) is a natural fit to be paired with LSDA exchange (which typically under-estimates exchange energy). Calculations involving a component of HF exchange are referred to as "hybrid" DFT methods.

1.4 Useful things from QM calculations

1.4.1 Potential energy surfaces

To discuss properties of atoms in particular configurations, it is helpful to start by considering a Born-Oppenheimer potential energy surface (PES). The PES is a hypersurface (typically denoted as U) defined as the potential energy of a set of fixed atoms over all possible arrangements of other atoms. The PES has $3N$ coordinate dimensions, which come from the fact that all atoms have unique Cartesian coordinates in 3-space.[6] Every point on the PES depicts a configuration of atoms, each of which can be described as a vector, $\tilde{\mathbf{r}}$,

$$\tilde{\mathbf{r}} = (r_{x1}, r_{y1}, r_{z1}, \ldots, r_{xN}, r_{yN}, r_{zN})$$

where r_{ai} represents the Cartesian coordinates of an atom i. It is also equally correct to express:

$$\tilde{\mathbf{r}} = (r_1, r_2, r_3, \ldots, r_{3N})$$

for generality. With atomic coordinates as a vector, we can express the whole PES as the function:

$$\mathbf{U}(\tilde{\mathbf{r}}) = E(r_1, r_2, r_3, \ldots, r_{3N})$$

where E has been calculated through either the solution of the TISE or with DFT. We can then define a gradient, $\mathbf{g}(\tilde{\mathbf{r}})$, of the PES to be the vector of partial derivatives of U that identifies the path of steepest descent.

$$\mathbf{g}(\tilde{\mathbf{r}}) = \left(\frac{\partial U}{\partial r_1}, \frac{\partial U}{\partial r_2}, \frac{\partial U}{\partial r_3}, \ldots, \frac{\partial U}{\partial r_{3N}}\right) \tag{1.14}$$

[6]Note that this is not describing an *internal* coordinate system where one omits 6 coordinates related to system translations and rotations to result in $3N - 6$ coordinates.

We can also define a second-derivative 'Hessian' matrix that contains information needed for vibrational frequencies.

$$H(U) = \begin{bmatrix} \frac{\partial^2 U}{\partial r_1 \partial r_1} & \frac{\partial^2 U}{\partial r_1 \partial r_2} & \cdots & \frac{\partial^2 U}{\partial r_1 \partial r_{3N}} \\ \frac{\partial^2 U}{\partial r_2 \partial r_1} & \frac{\partial^2 U}{\partial r_2 \partial r_2} & \cdots & \frac{\partial^2 U}{\partial r_2 \partial r_{3N}} \\ \vdots & \vdots & \ddots & \vdots \\ \frac{\partial^2 U}{\partial r_{3N} \partial r_1} & \frac{\partial^2 U}{\partial r_{3N} \partial r_2} & \cdots & \frac{\partial^2 U}{\partial r_{3N} \partial r_{3N}} \end{bmatrix} \tag{1.15}$$

While gradient calculations are typically manageable for large-scale calculations, Hessian calculations can be enormously time-consuming.

1.4.2 Geometry optimizations

Once the electronic energy, E, of a system of atoms is calculated, a gradient calculation can be undertaken as outlined in the previous section. With an obtained gradient, it is possible to use any number of algorithms to change the atomic positions of the molecule, $\tilde{\mathbf{r}}$, until the gradient has reached a point where its magnitude is sufficiently small, thereby indicating a stationary point on the PES. This process of calculating a gradient (1.14) (and then adjusting the atomic positions accordingly) from an energy determined from optimized basis set coefficients is called a geometry optimization step.[7]

Geometry optimizations can be run for stable intermediates (which should be at a local minimum of the PES) or for a transition state (TS) (which by TS-theory, should be the point where all but one internal normal coordinates are at a minimum.) Geometry optimizations greatly benefit from knowledge of the force constants associated with normal modes of the species at different points of the PES, and these force

[7]Common procedures for geometry optimizations include 'steepest descent,' 'conjugate gradient,' and Newton-Raphson, each of which have favorable characteristics, but all of which are simply algorithms to reach the desired state faster in lieu of troublesome regions of the topology of the PES.

constants can be obtained from the Hessian. To avert the expense of calculating a Hessian at every geometry iteration, processes are available to construct approximate Hessians from gradient calculations. The integrity of these Hessians is not always ideal, however, and a fully calculated Hessian at the end of a geometry optimization is warranted.

1.4.3 Vibrational frequencies

Vibrational frequencies can be calculated from U using the harmonic oscillator approximation, and solving the TISE in terms of nuclear coordinates. The one dimensional case uses the familiar spring constant $\frac{1}{2}kx^2$ form for its potential energy function.

$$\left[-\frac{1}{2\mu}\frac{\partial^2}{\partial r^2} + \frac{1}{2}k(r - r_{eq})^2\right]\Xi(r) = E\,\Xi(r) \tag{1.16}$$

The multidimensional case is more complex, but still solvable:

$$\left[-\sum_{i}^{3N}\frac{1}{2m_i}\frac{\partial^2}{\partial r_i^2} + \frac{1}{2}(\vec{r} - \vec{r}_{eq})^t H(U)(\vec{r} - \vec{r}_{eq})\right]\Xi(\vec{r}) = E\,\Xi(\vec{r}) \tag{1.17}$$

where $\vec{r}_{eq}$ represents the equilibrium structure and $H(U)$ is the Hessian matrix calculated in the previous section. A transformation of (1.17) allows for an efficient solution of $3N$ independent TISEs of the form of (1.16). The eigenfunctions of these equations are:

$$E = \left(n + \frac{1}{2}\right)h\omega$$

where n is the vibrational quantum number and ω, the vibrational frequency, is:

$$\omega = \frac{1}{2\pi}\sqrt{\frac{k}{\mu}} \tag{1.18}$$

where k is the force constant of the normal mode. When a force constant is positive, the mode of that molecule at that point in the PES is in a region of positive curvature. When a force constant is negative, the mode is in a region of negative curvature. Because of this, vibrational frequencies can serve as a quality-control checks for the user to insure that a structure optimized to either a stable intermediate or a TS has the appropriate number of positive normal modes. Indeed, vibrational frequencies should be calculated at the end of every geometry optimization for this very purpose.

Calculated vibrational frequencies also correlate to the same frequencies one observes in a molecular infrared spectrum. These frequencies are not expected to perfectly match with experiment, however, since the harmonic oscillator approximation used in Hessian calculations sometimes cannot adequately treat anharmonicities of vibrational modes. In the context of thermodynamics, which we will now proceed to, the zero-point vibrational energy (ZPVE) is defined as half of the sum of all vibrational normal modes, ω_i:

$$\text{ZPVE} = \frac{1}{2}\sum_i h\omega_i.$$

1.5 Calculating macroscopic contributions

1.5.1 Thermodynamic treatments of molecules

In order to build the energies of microscopic systems up into energies of macroscopic systems we employ traditional statistical thermodynamics with the ideal gas assumption. The rudimentary function that describes macroscopic properties is the partition function. The partition function is separable into electronic, translational, rotational, and vibrational components, each of which contribute to the total energy

of the macroscopic system.

$$E_{total} = \epsilon_{elec} + \epsilon_{trans} + \epsilon_{rot} + \epsilon_{vib}$$

Each ϵ_i in turn has internal energy components, U, and entropy, S, which are also separable into components:

$$U_{total} = U_{elec} + U_{trans} + U_{rot} + U_{vib}$$

$$S_{total} = S_{elec} + S_{trans} + S_{rot} + S_{vib}.$$

For simplicity, all expressions are in terms of molar quantities where $(N_A \cdot k_B \cdot T) = RT$, and where R is the molar gas constant.[8]

- Electronic energies: We employ the standard practice of defining all macroscopic energies in terms of electronic energy, ϵ_{elec}. Thus, we set ϵ_{elec} to be zero in instances without electronic degeneracies. In situations involving electronic degeneracies (i.e., doublet, triplet, etc., states), $S_{elec} = R \cdot \ln(2S+1)$ where S is the spin multiplicity of the molecular state (1/2 for doublet, 1 for triplet, etc.).

- Translational energies: The temperature dependent internal energy associated with molecular translations is $\frac{1}{2}RT$ for every translational degree of freedom for the molecule. In Cartesian space, this leads to $U_{trans} = \frac{3}{2}RT$. The entropy of translation is

$$S^{\circ}_{trans} = R\left\{\ln\left[\left(\frac{2\pi M k_B T}{h^2}\right)^{\frac{3}{2}} \frac{V^{\circ}}{N_A}\right] + \frac{5}{2}\right\}$$

  where V° is the molar volume of a gas at its standard state: 24.5 L. A note of caution is extended as this energy term is not usually reliable in calculations of species trapped in an aqueous cavities, nor in calculations involving transition

[8] RT equals 0.592 kcal/mol at 298K.

metals. In simulations on molecules in aqueous phase, a value of $60\% \cdot S^{\circ}_{trans}$ is sometimes employed, as is simply omitting S°_{trans} entirely. This basis for the latter correction is the assumption that these terms will roughly cancel on a relative energy scale for similarly-sized molecules. The latter treatment is used by the author in all data presented in this thesis.

- Rotational energies: As was the case with U_{trans}, the temperature dependent internal energy associated with molecular rotations is $\frac{1}{2}RT$ for each rotational degree of freedom. Single atoms receive no rotational energy, linear molecules receive RT, and non-linear molecules receive $\frac{3}{2}RT$. The entropy of rotation is:

$$S_{rot} = R\left\{\ln\left[\frac{\sqrt{\pi I_A I_B I_C}}{\sigma}\left(\frac{8\pi^2 k_B T}{h^2}\right)^{\frac{3}{2}}\right] + \frac{3}{2}\right\}$$

where σ is the rotational symmetric number for the molecule's point group, and I_A, I_B, and I_C are the molecule's three principle moments of inertia. As was the case with S_{trans}, the ideal gas S_{rot} is difficult to predict for aqueous species. Whatever treatment was chosen for S_{trans} should be the same treatment for S_{rot}.

- Vibrational energies: Thermodynamic energy contributions from molecular vibrations are calculated per vibrational frequency, ω_i. Thus, they can only be calculated once vibrational frequencies are obtained from a Hessian calculation. Vibrational energies must be summed over all $i = 3N - 6$ molecular vibrations.

$$U_{vib} = R\sum_i \frac{h\omega_i}{k_B(e^{h\omega_i/k_B T} - 1)} \tag{1.19}$$

and

$$S_{vib} = R\sum_i \left[\frac{h\omega_i}{k_B T(e^{h\omega_i/k_B T} - 1)} - \ln(1 - e^{-h\omega_i/k_B T})\right] \tag{1.20}$$

Using these energy contributions in addition to calculated E, we can build up data along the following energy surfaces and compare relative energies of two or more species:

$$H_{0K} = E + ZPVE \tag{1.21}$$

$$H_T = H_{0K} + U_T \text{ (+RT if in gas phase)} \tag{1.22}$$

$$G_T = H_T - TS_T. \tag{1.23}$$

1.5.2 Treatment of solvation

Studying molecules in aqueous phases requires understanding how the charge distribution of the solute responds to the dielectric of the solvent. Implicit solvation techniques use a continuous electric field to represent a statistical average of the dielectric effects of the solvent over all the solvent degrees of freedom. The Poisson equation (1.24) allows for the relation between the electrostatic potential inside a defined cavity, ϕ, the dielectric constant of the solvent outside of the cavity, ϵ, and the charge density of the solute, ρ.

$$\nabla\epsilon(r) \cdot \nabla\phi(r) = -4\pi\rho(r) \tag{1.24}$$

In Jaguar, the charge density is expressed as separate point charges corresponding to atomic nuclei. Using (1.24) it is possible to solve the free energy associated with the electronic relaxation.

$$E_{solv} = -\frac{1}{2}\int \rho(r)\phi(r)d(r) \tag{1.25}$$

The procedure for determining the cavity for this calculation is referred to as a Poisson-Boltzmann solver calculation.[14, 15] Furthermore, MOs can be optimized in an SCF procedure under the effects of the Poisson equation until both the density

matrix *and* the dipole moment have been rendered stationary. Thus, it is possible to obtain structures of molecules under the effect of any solvent (with a given dielectric constant and some means of generating ρ, e.g., a probe radius), albeit approximately.

1.6 Summary

This chapter presented the bare essentials to understand the tools utilized in calculating both microscopic properties (through wavefunction and DFT techniques) and macroscopic properties (through statistical thermodynamics and implicit solvation). For reference, Figure 1.1 is a schematic that illustrates the simple but multilayered processes involved in QM calculations. Chapter 2 will present how these tools do under tests of obtaining chemically relevant information.

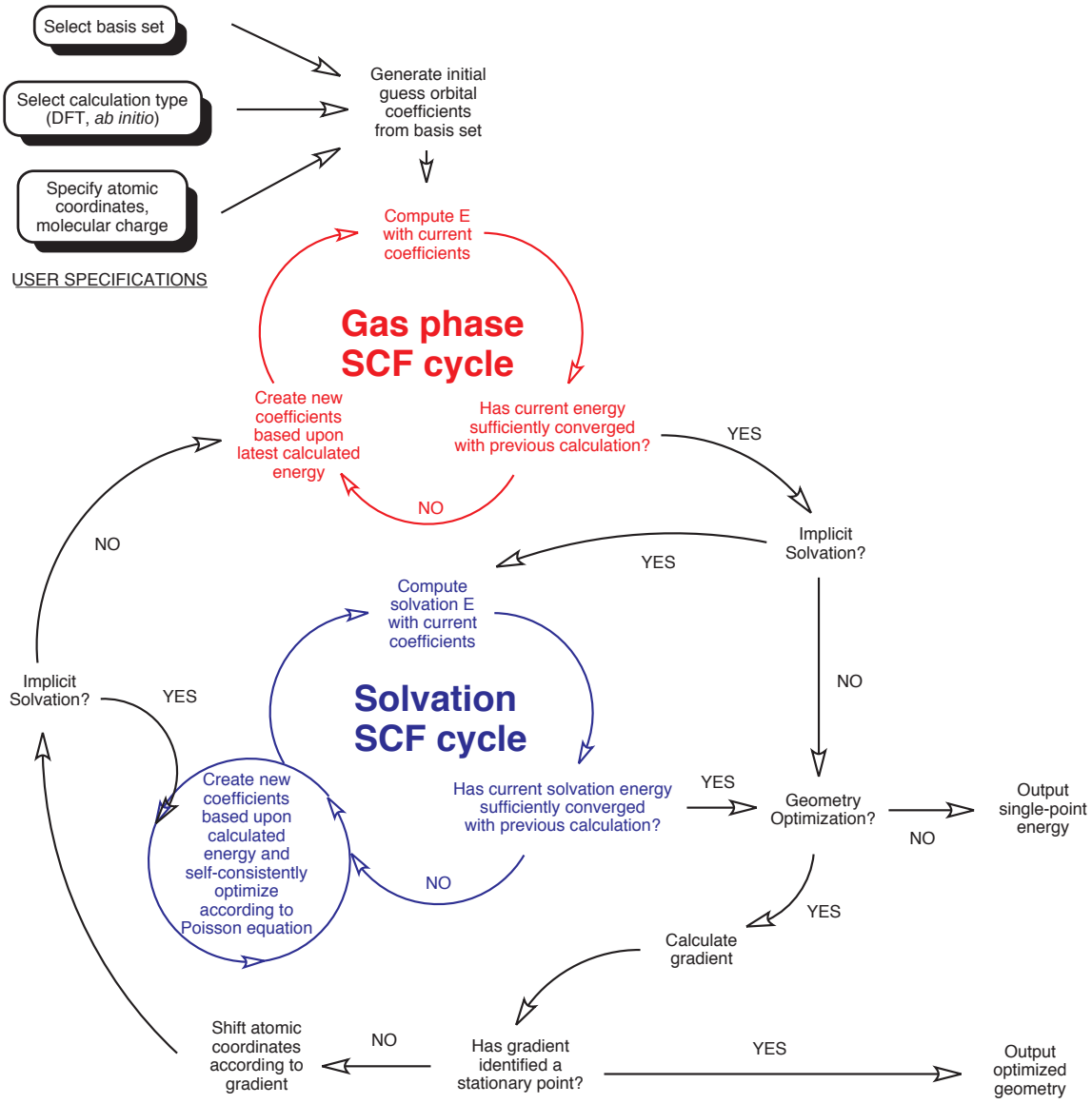

Figure 1.1: Routines and procedures for QM calculations

Chapter 2

How to Obtain Accurate Thermochemistry from Quantum Chemistry Calculations

2.1 Maximizing accuracy in calculations

2.1.1 Gas phase simulations

With the tools in place from in Chapter 1, we can now go about applying these methods to reproduce known observables. We know that the first step to obtaining an observable is calculating the electronic energy, from which vibrational frequencies and macroscopic thermodynamic quantities can be calculated. Quantum chemistry software packages have a multitude of different methods and algorithms for doing this. It is the user's responsibility to be aware which methods are best suited for the investigations that have warranted the need for calculations. Luckily, most modern density functional theory (DFT) methods suffice to obtain insightful data with semi-quantitative accuracy. With careful analysis, chemical accuracy (errors < 2 kcal/mol) are attainable.

Recall from Chapter 1 that solving (1.11) requires the use of a basis set to express electronic density. However, the basis set utilized to obtain an electronic energy does

not always need to be the same basis set used for a geometry optimization. Indeed, most moderately sized basis sets can be used to predict structures of molecules. For geometry optimizations most gas-phase species can be optimized with a double-ζ quality basis set (such as 6-31G) including a set of d and p polarization functions (denoted by *s) on all heavy and non-heavy atoms, respectively. In cases involving anionic species and weakly bound van der Waals and hydrogen-bound complexes added p diffuse functions (denoted by +s) on heavy atoms is usually justified, though not always necessary. For geometry optimizations on larger systems (such as those in Chapter 4) one should use the **midi!** basis set[16] on all non-reactive atoms and atoms not directly bound to polarizing transition metals. This basis set reduces the number of basis functions in the calculation without greatly reducing the integrity of the calculated geometry.

As mentioned in Chapter 1, calculated geometries must be confirmed with vibrational frequency calculations using the same method and basis set as the geometry optimization calculation. Since the vibrational frequencies are the eigenvalues of the second-derivative Hessian matrix, the force constants in the frequencies (see eq. (1.18)) correspond to second-derivative maximization/minimization tests common in calculus. Fully optimized stable intermediates should have all their internal coordinates at a minimum, so it follows that these calculations should result in only positive-valued vibrational frequencies. Fully optimized transition states are defined to have all internal coordinates at a local minimum, except for one coordinate which should be at a maximum. A fully optimized transition state should have only one imaginary frequency. The normal mode of this imaginary frequency should correspond to the reaction path of the transition between intermediates.

Furthermore, transition states should go through one more verification process to ensure that the determined transition state links two expected stable intermediates. In practice, minimum energy optimization of structures obtained from 'nudging' a

transition state in the forward and backward directions of the imaginary frequency usually result in expected stable intermediates. A more robust test is an Intrinsic Reaction Coordinate (IRC) calculation. IRC calculations start at a TS structure and then calculate a series of geometries optimizations at mass-weighted coordinates along the forward and reverse directions of the reaction path. IRC calculations are preferred to 'nudging' practices, as IRC calculations provide analysis along the more kinetically relevant mass-weighted coordinate system.

After a suitable geometry has been obtained, it is best to follow-up with a single-point energy calculation on the optimized structure with a larger basis set, usually one that is triple-ζ in quality (such as 6-311G), but always one with added polarization and diffuse functions (**++). While diffuse functions typically play an inconsequential role in geometry optimizations, they play a crucial role in accurate energies and must be used to ensure accurate energies in reactions.

In general, since the outcome of a simulation is some insight on multiple molecular structures or on relative energies of species along a reaction path, it is best to use one consistent method for all calculations. It is the author's experience that unexpected errors of more than 30 kcal/mol are almost always due to user-defined errors, either from method or basis set inconsistencies.

2.1.2 Condensed phase simulations

Calculations on molecules in condensed phases present a slightly more difficult problem than gas phase calculations. This problem is only slightly more complex though. While molecules in aqueous solution obviously do not physically behave as gas phase molecules, most thermodynamic properties of solvated molecules can be predicted by considering the electronic relaxation of the solute in the solvent as if it were a particle in a polarizing electric field. Implicit solvation methods do just this and calculate the relaxation energy of gas-phase molecules as if they were placed into an infinitely

large solvent bath.

It should be noted that the solvation energy returned by the Poisson-Boltzmann continuum solver and similar methods include a free-energy correction incorporating a finite amount of solvent entropy into the calculation. While the entropic contribution is generally considered to be small, it is not small enough to truthfully state that ΔE or ΔH values with added solvation energy are free of some implicit entropy contributions.

Sometimes, it is expected that a highly polarizing solvent (such as water) will substantially stabilize molecular geometries not expected to be stabilized in the gas phase. Modern computing allows for geometry optimizations that use gradients calculated from solvent-relaxed density matrices, however these calculations can take 3–5 times as long to complete (due to the additional 3–5 solvent SCF cycles at each geometry iteration.) Molecular structures optimized in solvent should also be verified with vibrational frequencies calculated in the presence of the solvent continuum. However, these calculations are very computationally expensive for most quantum chemical software packages. As such, solvent-optimized structures should only be considered if there is good reason for doing so. Under most circumstances not involving zwitterionic complexes or multiply charged systems, a single-point solvent energy taken at the gas-phase optimized geometry will suffice for chemical predictions.

Occasionally, when calculating vibrational frequencies under the presence of implicit solvation, vibrational frequencies of an apparently optimized complex will have low-energy imaginary frequencies corresponding to ligand torsions. In reality, these torsions should be periodic but QM programs identify these motions as harmonic, and thus contribute towards the vibrational partition function in eqs. (1.19) and (1.20). A straightforward solution to this problem is to recalculate these expressions with a modified list of frequencies where each frequency with a value lower than 50cm^{-1} is replaced with a frequency with a value of 50cm^{-1}. This correction is mostly for con-

tinuity purposes and eliminates discontinuities with calculations involving imaginary frequencies (which are omitted entirely from thermodynamic calculations) and low frequencies (< 50 cm^{-1}) (which have dramatic consequences to overall free energies.)

2.1.3 Keeping track of thermodynamics

With the gas phase and solvent phase energies obtained, expressions for relative energies on a ΔE potential energy surface are obtainable. However, ΔE energies are rarely of use in comparison to experiment, so additional thermodynamic properties are added.

The zero-point vibrational energy (ZPVE) is obtained from vibrational frequency calculations. So too are expressions for the thermal enthalpy and entropy contributions at a given temperature. It is important to note that all thermodynamic values are made with the ideal gas approximation at a standard state of one atmosphere, even those involving implicit solvation. It is consideration of this standard state that requires some additional attention. When running implicit solvation calculations, the resulting solvation energy is that associated with the electronic relaxation of the gas phase species at a particular standard state **to the same standard state** in aqueous phase. The free energy contribution of moving from one concentration, c_0, to another, c, is:

$$\Delta G = +RT \ln \left(\frac{c}{c_0} \right). \tag{2.1}$$

Additionally, in the context of enthalpy, gas phase species contain an additional intrinsic energy contribution of $+pV = RT$ while aqueous species do not.

These corrections are necessary to keep track of while comparing energies referenced at standard states of gases (1 atm at 298K), compared to those in aqueous solution (1 M at 298K), or compared to species at any particular concentration, such as water, (55.5 M at 298K). Solvation energies from experimental thermochemical

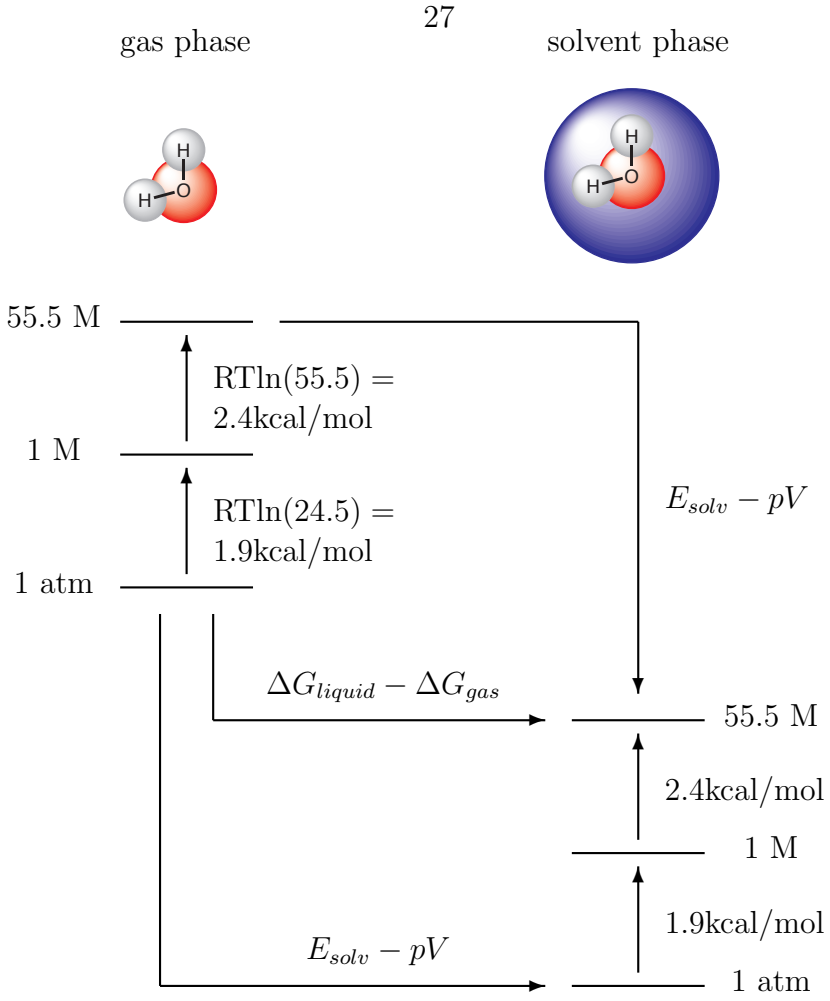

Figure 2.1: Schematic depicting free energy changes across standard states

data can be used in concordance with calculation data so long as these corrections are kept in mind. Unfortunately, failure to correctly account for these reference states is not uncommon[17, 18], and conceptualizing a consistent thermochemical cycle similar to that shown in Figure 2.1 is usually the best way to ensure that the treatment of these corrections is correct.

2.2 An investigation on the performance of DFT calculation methods with implicit solvation

2.2.1 Survey of density functional methods

Many DFT methods are available for usage and are generally regarded as sharing similar accuracies, however their mathematical formulae can all be quite different. Elaborate benchmark studies have been made for organics, organics in solution, and monatomic aqueous transition metal ions. A benchmark study has not yet been presented showing general accuracy for DFT methods in applications relating to mechanism investigation.

The belief that most DFT methods are well suited for calculations of inorganic molecules in condensed phases is put to the test through an investigation of properties that can be obtained through first-principles calculations. We compare a total of six DFT methods that span from GGA DFT methods (BP86[8, 19], PBE[11, 12]) through hybrid DFT methods that include minimal parameterization (B3LYP[6], mPW1PW91[13]), moderate parameterization (SB98[20, 21]), and heavy parameterization (M06[22]). Two methods, M06 and SB98, also include an additional term in the functionals to account for kinetic energy gradients. This kinetic energy correction is finding itself more prevalent in modern DFT methods, though its utility in the scope of applied inorganic reactions is not yet known. This benchmarking investigation will identify areas where DFT methods are adequately treating energetics of inorganic complexes in solution and areas where there is room for improvement.

All calculations were run using Jaguar 6.5[23] except M06 calculations which used Jaguar 7.0.[4] In order to minimize computational expense, we make an approximation by calculating all thermodynamic contributions of ZPVE, $\Delta H_{0\rightarrow 298K}$, and $\Delta S_{0\rightarrow 298K}$ from B3LYP/LACVP** gas phase calculations. Errors associated with

this approximation are expected to be minimal based on calculations showing small (< 1 kcal/mol) differences between total calculated thermodynamics. From this optimized gas phase structure, subsequent solvent-optimized structures are obtained for the six DFT methods. From these solvent-optimized structures, single point energy calculations with the LACVP**++ basis set obtain more accurate values for gas phase energies.

2.2.2 Associative ligand exchange reactions

We evaluate the relative energetics and the forward and reverse barrier heights for reactions presented in Figure 2.2.2. These represent all possible H_2O/Cl^- ligand exchange reactions involving square-planar Pd(II) and Pt(II) and most of this data, with a few exceptions, is well-established in the literature[24]. We report relative free

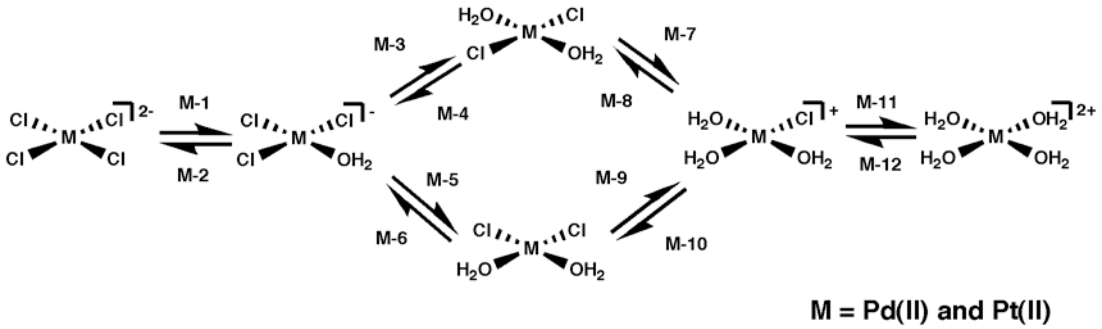

Figure 2.2: Investigated associative ligand exchange reactions

energies as differences between the calculated absolute free energy, G, of two species. For species involving transition metals, we define G as:

$$\mathbf{G_{mol} = E_{gas} + E_{solv} + ZPVE + H_{vib_{298K}} + 3 * RT - T * S_{vib_{298K}} + RT * ln(24.5)}$$

where RT = .592 kcal/mol at 298K. For H_2O:

$$\mathbf{G_{H_2O} = -47962.6\,kcal/mol}$$

This value is obtained by taking our gas phase absolute free energy,

$$G_{H_2O_{gas}} = E_{gas} + ZPVE + H_{vib_{298K}} + 3 * RT + pV - T * S_{tot_{298K}} = -47960.6\,\text{kcal/mol}$$

and adding -2.05 kcal/mol (the experimental free energy of vaporization for H_2O[25]). For Cl^-:

$$\mathbf{G_{Cl^-} = -288908.8\,kcal/mol}$$

This value is obtained by taking our gas phase absolute free energy:

$$G_{Cl^-} = E_{gas} + \frac{3}{2} * RT + pV - T * S_{tot_{298K}}$$

using $S_{tot_{298K}}$ = 36.7 cal/mol*K,[26] and adding -74.6 kcal/mol (the experimental free energy of solvation for Cl^-.[27])

Sample calculation:

For the associative ligand exchange reaction barrier, **Pd-1**:

$$[Pd(II)(Cl)_4]^{2-} + H_2O \rightarrow [Pd(II)(Cl)_4(H_2O)]^{\ddagger 2-}$$

we calculate:

H_2O

$E_{gas} = -76.43312825144\,E_h = -47962.5\,\text{kcal/mol}$

$ZPVE = 13.4\,\text{kcal/mol}$

$H_{vib_{298K}} + 3 * RT + pV = 2.4\,\text{kcal/mol}$

$-298K * S_{H_2O} = -13.9\,\text{kcal/mol}$

$\Delta G_{solv} = -2.1\,\text{kcal/mol}$

$\mathbf{G = -47962.6\,kcal/mol}$

$$[\mathbf{Pd(II)(Cl)_4}]^{\mathbf{2-}}$$
$$E_{gas} = -1967.726836\ E_h = -1234767.3\ \text{kcal/mol}$$
$$E_{solv} = -0.3009667\ E_h = -188.9\ \text{kcal/mol}$$
$$\text{ZPVE} = 2.3\ \text{kcal/mol}$$
$$H_{vib_{298K}} + 3 * RT = 5.2\ \text{kcal/mol}$$
$$-T * S_{vib_{298K}} = -6.9\ \text{kcal/mol}$$
$$RT * \ln(24.5) = 1.9\ \text{kcal/mol}$$
$$\mathbf{G = -1234953.7\ kcal/mol}$$

$$[\mathbf{Pd(II)(Cl)_4(H_2O)}]^{\mathbf{\ddagger 2-}}$$
$$E_{gas} = -2044.156212\ E_h = -1282727.4\ \text{kcal/mol}$$
$$E_{solv} = -0.29941731\ E_h = -187.9\ \text{kcal/mol}$$
$$\text{ZPVE} = 17.9\ \text{kcal/mol}$$
$$H_{vib_{298K}} + 3 * RT = 6.5\ \text{kcal/mol}$$
$$-T * S_{vib_{298K}} = -9.6\ \text{kcal/mol}$$
$$RT * \ln(24.5) = 1.9\ \text{kcal/mol}$$
$$\mathbf{G = -1282898.6\ kcal/mol}.$$

Thus, the barrier has a calculated $\Delta G^{\ddagger}_{298K}$ = (-1282898.6 kcal/mol) -[(-1234953.7 kcal/mol) + (-47962.6 kcal/mol)] = +17.7 kcal/mol, which is in fairly good agreement with the experimental barrier of $\Delta G^{\ddagger}_{298K}$ = +16 kcal/mol. Using similar calculations, we can obtain the data compiled in Tables 2.1 and 2.2; errors across both tables are presented in Table 2.3.

Before delving into large numbers of data, it should be noted that this approach to calculating data is the quick-and-dirty solution to difficult quantum mechanics simulations. It is known that implicit solvation methods are typically insufficient, treating solvation energies of singly charged systems without explicit water molecules present in the simulation to delocalize charges. Also, fairly vague assumptions have been made in the parameterization of transition metals in the PBF solvation model. That said, the expected accuracy of DFT calculations under ideal circumstances is 3–5 kcal/mol errors for barrier heights and 2–3 kcal/mol errors for relative thermodynamics. Since these simulations are far removed from ideal conditions, one might expect substantially worse errors.

Table 2.1 shows calculated data for ligand exchange reactions involving Pd(II) complexes. Substantial thermochemical data is missing from this table, and modern experimental investigations would provide the final pieces of missing information. Across this test set of Pd(II) complexes, it is difficult to distinguish a clear-cut front runner since a large amount of data is missing for reactions **Pd-7** through **Pd-10**. Of the data that is available, it is surprising that the non-parameterized BP86 and PBE functionals do quite well predicting barrier heights of Pd(II) reactions to within 2.5 kcal/mol and 2.4 kcal/mol, respectively; while errors in relative thermodynamics are 1.3 kcal/mol and 1.2 kcal/mol, respectively. Also noticeably, the highly parameterized M06 functional does not do particularly well in predicting barrier heights for Pd(II) reactions, but it does appear to be substantially better than all other functionals in calculating the barrier for reaction **Pd-12**. Generally speaking, calculations fall towards the high end of expectation of accuracies for DFT methods, though there is clear room for improvement starting with the treatment of the barrier in **Pd-12**.

Table 2.2 shows calculated data for ligand exchange reactions involving Pt(II) complexes. Likewise, calculations show similar accuracies across the larger data set, though M06 and PBE functionals yield substantially worse enthalpic barriers (RMS = 6.3 kcal/mol and 4.3 kcal/mol, respectively) than in Pd(II) enthalpic barriers (RMS = 1.9 kcal/mol and 0.9 kcal/mol). In terms of free energy barriers, errors between Pd(II) and Pt(II) are consistent to within 1 kcal/mol.

Table 2.3 shows RMS errors in calculations across different sets of data. Interestingly, all the DFT methods except M06 do very well at predicting barriers for anionic transition states, while M06 is quite poor. However, for cationic transition states, M06 is the only method that exceeds expected accuracies. Since consistent errors in barrier heights should cancel out when comparing relative energies of intermediates, one should expect that DFT methods should have smaller errors in calculating relative energies than in barrier heights. We see this to be the case. That enthalpic

barriers and enthalpic relative energies are usually on par with free energy barriers and free energy relative energies shows that the entropic contribution intrinsically treated in PBF solvation is minor.

In summary, calculations on associative ligand exchange reactions can be done adequately by DFT methods with appropriate free energy corrections and experimental solvation energies when available. Although by far the most popular of DFT methods, B3LYP does not display itself in an outstanding light in this study. The overall errors in B3LYP can fairly easily be attributed to its larger errors in cationic transition states. It is the versatility of B3LYP that still makes it a desirable choice when using DFT calculations, and still arguably superior to PBE and BP86 in multipurpose calculations.

The benefit to BP86 and PBE functionals is their faster performance in addition to their mathematical purity. B3LYP and *m*PW1PW91 hybrid functionals are roughly equivalent to *m*PW1PW91, winning out over B3LYP slightly. There are no apparent gains in using kinetic operator gradients, as in the cases with M06 and SB98 functionals. Lastly, the M06 functional appears to be unreliable in these classes of calculations despite its heavy parameterization, though its unreliability could be due to its heavy parameterization.

2.2.3 Deprotonation reactions—pK_a calculations

Besides ligand exchange reactions, another difficult calculation involves deprotonation reactions which are necessary for pK_a calculations. Very limited experimental data involving inorganic complexes is available for such calculations, however[25]. We have taken available data (Figure 2.2.3) and compared the same calculations from the previous study. All calculations are done in a similar manner. The deprotonation

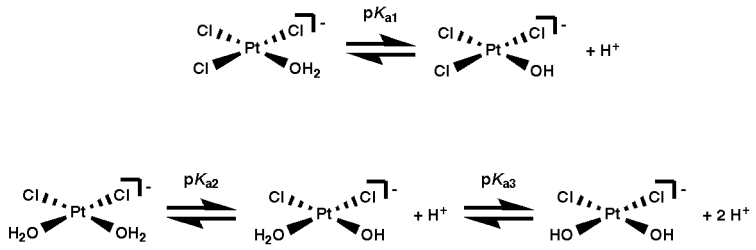

Figure 2.3: Investigated deprotonation reactions

reactions add an additional hurdle from the standpoint of simulation, and that is treatment of a proton solvated in solution. The difficulty in treating protons is two-fold: (1) it is impossible to calculate E or E_{solv} from a species with no electrons, and (2) the compact charge of a proton in solvent is very difficult to model with implicit solvation.[1] We present three different approaches to this problem:

1. **All-QM simulations involving explicit $\mathbf{H_3O^+}$:** To calculate deprotonation reactions entirely with QM, the most straightforward approach would be to include an explicit H_2O to the left side and an explicit hydronium ion (H_3O^+) to the right side of the balanced reaction. This allows all solvation energies to be calculated from QM.

Sample calculation:

The following reaction (which has a experimental $\Delta G = 9.6$ kcal/mol)

$$[\mathrm{Pt(Cl)_3(H_2O)}]^- + \mathrm{H_2O} \rightarrow [\mathrm{Pt(Cl)_3(OH)}]^{2-} + \mathrm{H_3O^+}$$

has the following computed values:

$$[\mathbf{Pt(Cl)_3(H2O)}]^-$$
$$\mathrm{E_{gas}} = -1576.385745\,\mathrm{E_h} = -989197.0\,\mathrm{kcal/mol}$$
$$\mathrm{E_{solv}} = -0.10808\,\mathrm{E_h} = -67.8\,\mathrm{kcal/mol}$$
$$\mathrm{ZPVE} = 18.1\,\mathrm{kcal/mol}$$
$$\mathrm{H_{vib_{298K}}} + 3 * \mathrm{RT} = 5.4\,\mathrm{kcal/mol}$$

[1] Recent studies within our group indicate that implicit solvation energies converge after adding 18 explicit waters to a QM simulation of proton, however most of this solvation energy is captured with 4 explicit waters.

$$-\mathrm{T} * \mathrm{S}_{\mathrm{vib}_{298\mathrm{K}}} = -7.0\,\mathrm{kcal/mol}$$
$$\mathrm{RT} * \ln(24.5) = 1.9\,\mathrm{kcal/mol}$$
$$\mathbf{G = -989246.5 kcal/mol}$$

$$[\mathbf{Pt(Cl)_3(OH)}]^{\mathbf{2-}}$$
$$\mathrm{E_{gas}} = -1575.727198\,\mathrm{E_h} = -988783.8\,\mathrm{kcal/mol}$$
$$\mathrm{E_{solv}} = -0.31737\,\mathrm{E_h} = -199.2\,\mathrm{kcal/mol}$$
$$\mathrm{ZPVE} = 10.2\,\mathrm{kcal/mol}$$
$$\mathrm{H}_{\mathrm{vib}_{298\mathrm{K}}} + 3 * \mathrm{RT} = 5.1\,\mathrm{kcal/mol}$$
$$-\mathrm{T} * \mathrm{S}_{\mathrm{vib}_{298\mathrm{K}}} = -6.4\,\mathrm{kcal/mol}$$
$$\mathrm{RT} * \ln(24.5) = 1.9\,\mathrm{kcal/mol}$$
$$\mathbf{G = -988972.1\,kcal/mol}$$

$$\mathbf{H_2O}$$
$$\mathbf{G = -47962.6\,kcal/mol}$$

$$\mathbf{H_3O^+}$$
$$\mathrm{E_{gas}} = -76.70581677\,\mathrm{E_h} = -48133.6\,\mathrm{kcal/mol}$$
$$\mathrm{E_{solv}} = -0.16034881\,\mathrm{E_h} = -100.6\,\mathrm{kcal/mol}$$
$$\mathrm{ZPVE} = 22.0\,\mathrm{kcal/mol}$$
$$\mathrm{H}_{\mathrm{vib}_{298\mathrm{K}}} + 3 * \mathrm{RT} = 1.8\,\mathrm{kcal/mol}$$
$$-\mathrm{T} * \mathrm{S} = -3.7\,\mathrm{kcal/mol}\ (\mathrm{S\ obtained\ from}\ (45.9\,\mathrm{cal/mol} * \mathrm{K})[26] + (-33.6\,\mathrm{cal/mol} * \mathrm{K})[27])$$
$$\mathrm{RT} * \ln(24.5) = 1.9\,\mathrm{kcal/mol}$$
$$\mathbf{G = -48212.2\,kcal/mol}.$$

Thus, the relative free energy is:

$$\Delta\mathrm{G} = [(-988972.1\,\mathrm{kcal/mol}) + (-48212.2\,\mathrm{kcal/mol})]$$
$$-[(-989246.5\,\mathrm{kcal/mol}) + (-47962.6\,\mathrm{kcal/mol})]$$
$$= 24.8\,\mathrm{kcal/mol!}$$

This result thus has an error of 15.6 kcal/mol, an obviously grave deficiency in this type of calculation, and likely the result of a poor description of the solvation energy of H_3O^+.

2. **Simulations using experimental H_3O^+ solvation energies:** As we believe the description of H_3O^+ solvation is poor, we examined whether using the experimental solvation energy of H_3O^+ would improve the accuracy of the test calculations. For the same deprotonation reaction as above we calculate the relative energies:

Sample calculation:

$$[\mathbf{Pt(Cl)_3(H_2O)}]^-$$
$$\mathbf{G = -989246.5\ kcal/mol}$$

$$[\mathbf{Pt(Cl)_3(OH)}]^{\mathbf{2-}}$$
$$\mathbf{G = -988972.1\ kcal/mol}$$

$$\mathbf{H_2O}$$
$$\mathbf{G = -47962.6\ kcal/mol}$$

$$\mathbf{H_3O^+}$$
$$\mathrm{E_{gas} = -76.70581677\ E_h = -48133.6\ kcal/mol}$$
$$\mathrm{ZPVE = 21.6\ kcal/mol}$$
$$\mathrm{H_{vib_{298K}} + 3 * RT + pV = 2.4\ kcal/mol}$$
$$\mathrm{-T * S = -14.4\ kcal/mol}$$
$$\mathrm{G_{solv} = -110.2\ kcal/mol}$$
$$\mathbf{G = -48234.2\ kcal/mol}.$$

In this approach, calculating the deprotonation of $[Pt(Cl)_3(H_2O)]^-$ leads to a free energy difference of

$$\begin{aligned}\Delta G = &[(-988972.1\ \mathrm{kcal/mol}) + (-48234.2\ \mathrm{kcal/mol})] \\ &-[(-989246.5\ \mathrm{kcal/mol}) + (-47962.6\ \mathrm{kcal/mol})] \\ &= 2.8\ \mathrm{kcal/mol}.\end{aligned}$$

While this is a noticeable improvement over the QM solvation energy calculations, this ~ 7 kcal/mol error is not satisfactory for the purposes of mechanistic investigations.

3. **Simulations using experimental H^+ solvation energies** An alternate approach would be to use the experimental energies for H^+ instead of the explicit hydronium. For the deprotonation reaction:

$$[Pt(Cl)_3(H_2O)]^- \rightarrow [Pt(Cl)_3(OH)]^{2-} + H^+$$

we calculate the relative energies:

Sample calculation:

$$[\mathbf{Pt(Cl)_3(H_2O)}]^-$$
$$\mathbf{G = -989246.5\ kcal/mol}$$

$$[\mathbf{Pt(Cl)_3(OH)}]^{\mathbf{2-}}$$
$$\mathbf{G = -988972.1\ kcal/mol}$$

$$\mathbf{H^+}$$
$$H_{gas} = 3 * RT = 1.8\ kcal/mol$$
$$-T * S_{gas} = -7.82\ kcal/mol$$
$$G_{solv} = -254.0\ kcal/mol[27]$$
$$\mathbf{G_{H^+} = -270.3\ kcal/mol}.$$

In this approach, calculating the deprotonation of $[Pt(Cl)_3(H_2O)]^-$ leads to a free energy difference of

$$G = [(-988972.1\ kcal/mol) + (-270.3\ kcal/mol)]$$
$$-(-989246.5\ kcal/mol)$$
$$= 4.1\ kcal/mol$$

which is thus far the best agreement with the experimental value, 9.6 kcal/mol.

We now present data on calculations of the various DFT methods. At first glance, it should be clear how difficult deprotonation reactions can be in simulations. Errors in these cases are far above expected errors for stable intermediates, and even with treatments using experimental solvation energies, all calculations are underestimated by at least 5 kcal/mol. Interestingly, across the three deprotonation reactions, the absolute value of the mean error and the RMS error are essentially identical. This suggests that while an large error is present, a single empirical correction could be used to reduce the large errors in these specific calculations. The empirical correction would simply be the value of the mean error for that specific DFT method. Employing such a correction reduces errors to an RMS error of ~ 1 kcal/mol. While this is not a long-term solution, this result suggests that a critical shortcoming of DFT simulations can

be identified. Further investigations of deprotonation reactions involving transition metals are strongly warranted.

Reaction	ref.	Thermo.	Barrier Heights (kcal/mol)						
			Exp.	Density Functionals					
				B3LYP	BP86	M06	mPW	PBE	SB98
Pd-1	[28]	$\Delta H^{\ddagger}$	12	12.9	12.7	10.7	13.7	10.8	12.7
		$\Delta G^{\ddagger}$	16	17.7	17.6	15.0	18.2	15.8	17.3
Pd-2	[28]	$\Delta H^{\ddagger}$	10	13.0	11.4	7.1	12.5	9.8	11.8
		$\Delta G^{\ddagger}$	14	15.2	13.6	9.3	14.7	12.0	14.0
Pd-3	[29]	$\Delta H^{\ddagger}$	–	13.1	11.9	10.9	12.9	10.5	12.3
		$\Delta G^{\ddagger}$	19	18.5	17.5	15.9	18.0	16.3	17.6
Pd-4	[29]	$\Delta H^{\ddagger}$	–	12.3	9.9	5.8	10.8	8.4	10.7
		$\Delta G^{\ddagger}$	14	16.2	13.8	9.6	14.6	12.3	14.5
Pd-5	[29]	$\Delta H^{\ddagger}$	–	16.7	15.9	14.3	17.4	14.4	16.4
		$\Delta G^{\ddagger}$	20	21.1	20.4	18.2	21.4	19.1	20.6
Pd-6	[29]	$\Delta H^{\ddagger}$	–	15.9	13.4	8.4	15.0	11.8	14.7
		$\Delta G^{\ddagger}$	15	17.8	15.3	10.3	16.9	13.6	16.5
Pd-7	–	$\Delta H^{\ddagger}$	–	15.8	15.4	14.1	16.3	14.0	15.4
		$\Delta G^{\ddagger}$	–	22.3	22.0	20.1	22.4	20.8	21.7
Pd-8	–	$\Delta H^{\ddagger}$	–	15.1	12.5	8.0	13.6	11.0	13.7
		$\Delta G^{\ddagger}$	–	18.8	16.3	11.7	17.3	14.7	17.4
Pd-9	–	$\Delta H^{\ddagger}$	–	14.5	14.1	13.2	14.4	12.7	14.0
		$\Delta G^{\ddagger}$	–	20.3	20.0	18.5	19.9	18.8	19.6
Pd-10	–	$\Delta H^{\ddagger}$	–	13.9	11.8	7.8	12.0	10.2	12.4
		$\Delta G^{\ddagger}$	–	17.8	15.7	11.7	15.9	14.1	16.3
Pd-11	[28]	$\Delta H^{\ddagger}$	14	16.1	15.7	15.2	16.8	14.5	16.0
		$\Delta G^{\ddagger}$	18	22.5	22.2	21.1	22.8	21.1	22.2
Pd-12	[28]	$\Delta H^{\ddagger}$	10	15.0	12.5	8.4	14.0	11.1	14.1
		$\Delta G^{\ddagger}$	12	18.7	16.3	12.2	17.8	14.9	17.8

Reaction	ref.	Thermo.	Relative thermodynamics (kcal/mol)						
			Exp.	Density Functionals					
				B3LYP	BP86	M06	mPW	PBE	SB98
Pd-1 $\rightleftharpoons$ Pd-2	[28]	ΔH	2	-0.1	1.3	3.6	1.2	1.0	0.9
		ΔG	2	2.5	4.0	5.7	3.4	3.8	3.3
Pd-3 $\rightleftharpoons$ Pd-4	[29]	ΔH	–	0.7	2.0	5.1	2.1	2.2	1.7
		ΔG	5	2.3	3.7	6.3	3.4	4.0	3.1
Pd-5 $\rightleftharpoons$ Pd-6	[29]	ΔH	–	0.8	2.5	5.9	2.4	2.7	1.7
		ΔG	5	3.3	5.2	8.0	4.6	5.5	4.0
Pd-7 $\rightleftharpoons$ Pd-8	–	ΔH	–	0.7	2.9	6.1	2.8	3.1	1.6
		ΔG	–	3.5	5.8	8.4	5.1	6.1	4.2
Pd-9 $\rightleftharpoons$ Pd-10	–	ΔH	–	0.6	2.3	5.4	2.4	2.5	1.6
		ΔG	–	2.5	4.3	6.7	3.9	4.7	3.3
Pd-11 $\rightleftharpoons$ Pd-12	[28]	ΔH	4	1.2	3.2	6.8	2.7	3.3	2.0
		ΔG	6	3.7	5.9	8.9	5.0	6.2	4.3

Table 2.1: Calculated thermochemical data for associative ligand exchange reactions involving Pd(II)

Reaction	ref.	Thermo.	Barrier Heights (kcal/mol)						
			Exp.	Density Functionals					
				B3LYP	BP86	M06	mPW	PBE	SB98
Pt-1	[30]	$\Delta H^{\ddagger}$	21	18.6	18.4	15.8	19.7	16.9	18.8
		$\Delta G^{\ddagger}$	23	23.1	23.0	19.7	23.9	21.6	23.0
Pt-2	[30]	$\Delta H^{\ddagger}$	18.4	17.4	15.5	11.0	17.0	13.9	16.5
		$\Delta G^{\ddagger}$	21	19.4	17.4	12.9	18.9	15.9	18.4
Pt-3	[30]	$\Delta H^{\ddagger}$	20	18.8	17.9	16.6	18.9	16.3	18.2
		$\Delta G^{\ddagger}$	23	24.0	23.2	21.3	23.8	21.8	23.2
Pt-4	[30]	$\Delta H^{\ddagger}$	17.7	17.2	14.3	10.9	15.3	12.7	15.5
		$\Delta G^{\ddagger}$	19	19.5	16.7	13.3	17.7	15.1	17.8
Pt-5	[30]	$\Delta H^{\ddagger}$	24	23.2	22.7	19.9	23.8	21.4	23.9
		$\Delta G^{\ddagger}$	28	27.6	27.3	23.8	28.0	26.2	28.2
Pt-6	[30]	$\Delta H^{\ddagger}$	22.8	21.6	18.8	13.7	21.0	17.2	21.6
		$\Delta G^{\ddagger}$	23	23.3	20.6	15.4	22.7	19.0	23.4
Pt-7	[30]	$\Delta H^{\ddagger}$	–	22.8	21.7	19.9	23.1	20.8	22.8
		$\Delta G^{\ddagger}$	26	27.8	27.0	24.6	27.9	26.2	27.7
Pt-8	[30]	$\Delta H^{\ddagger}$	–	22.3	18.9	14.9	20.7	17.6	21.0
		$\Delta G^{\ddagger}$	26	25.8	22.4	18.4	24.2	21.1	24.5
Pt-9	[30]	$\Delta H^{\ddagger}$	–	19.5	18.7	17.7	20.3	17.3	19.9
		$\Delta G^{\ddagger}$	21	24.7	24.1	22.6	25.3	22.9	25.0
Pt-10	[30]	$\Delta H^{\ddagger}$	–	18.9	16.1	13.2	17.2	14.7	17.7
		$\Delta G^{\ddagger}$	18	22.5	19.7	16.8	20.8	18.3	21.3
Pt-11	[30]	$\Delta H^{\ddagger}$	–	24.0	22.8	21.3	24.3	21.8	23.8
		$\Delta G^{\ddagger}$	26	29.7	28.7	26.6	29.7	27.9	29.4
Pt-12	[30]	$\Delta H^{\ddagger}$	–	23.8	20.4	16.8	22.3	19.1	22.6
		$\Delta G^{\ddagger}$	20	26.8	23.5	19.9	25.3	22.2	25.7

Reaction	ref.	Thermo.	Relative thermodynamics (kcal/mol)						
			Exp.	Density Functionals					
				B3LYP	BP86	M06	mPW	PBE	SB98
Pt-1 $\rightleftharpoons$ Pt-2	[30]	ΔH	2.6	1.2	2.9	4.8	2.7	2.9	2.3
		ΔG	2	3.7	5.6	6.9	4.9	5.8	4.6
Pt-3 $\rightleftharpoons$ Pt-4	[30]	ΔH	2.3	1.7	3.6	5.7	3.6	3.6	2.7
		ΔG	4	4.4	6.5	8.1	6.1	6.7	5.4
Pt-5 $\rightleftharpoons$ Pt-6	[30]	ΔH	1.2	1.6	3.9	6.2	2.9	4.2	2.3
		ΔG	5	4.2	6.7	8.5	5.3	7.2	4.8
Pt-7 $\rightleftharpoons$ Pt-8	[30]	ΔH	–	0.5	2.8	5.0	2.4	3.2	1.8
		ΔG	5	2.1	4.6	6.2	3.8	5.1	3.2
Pt-9 $\rightleftharpoons$ Pt-10	[30]	ΔH	–	0.6	2.6	4.5	3.2	2.6	2.2
		ΔG	5	2.3	4.4	5.8	4.6	4.6	3.7
Pt-11 $\rightleftharpoons$ Pt-12	[30]	ΔH	–	0.3	2.4	4.5	2.0	2.7	1.2
		ΔG	6	2.9	5.2	6.7	4.4	5.6	3.7

Table 2.2: Calculated thermochemical data for associative ligand exchange reactions involving Pt

Reaction	Thermo.	No. of Reactions	RMS errors (kcal/mol) Density Functionals B3LYP	BP86	M06	mPW	PBE	SB98
Pd reactions	$\Delta H^{\ddagger}$	4	3.1	1.7	1.9	2.9	0.9	2.5
	$\Delta G^{\ddagger}$	8	3.3	2.5	3.6	3.1	2.4	2.9
Pt reactions	$\Delta H^{\ddagger}$	6	1.3	2.9	6.3	1.5	4.3	1.8
	$\Delta G^{\ddagger}$	12	3.1	2.1	4.1	2.6	2.5	2.7
anionic reactions	$\Delta H^{\ddagger}$	8	1.6	2.5	5.6	1.7	3.8	1.7
	$\Delta G^{\ddagger}$	12	1.2	1.6	4.9	1.2	2.7	1.1
cationic reactions	$\Delta H^{\ddagger}$	2	3.8	2.1	1.4	3.5	0.9	3.2
	$\Delta G^{\ddagger}$	8	4.9	3.0	1.8	4.1	2.0	4.1
all reactions	$\Delta H^{\ddagger}$	10	2.2	2.5	5.1	2.2	3.4	2.1
	$\Delta G^{\ddagger}$	20	3.2	2.3	3.9	2.8	2.5	2.7

Reaction	Thermo.	No. of Reactions	RMS errors (kcal/mol) Density Functionals B3LYP	BP86	M06	mPW	PBE	SB98
Pd reactions	ΔH	2	2.5	0.8	2.3	1.1	0.9	1.6
	ΔG	4	1.9	1.3	3.0	1.2	1.2	1.4
Pt reactions	ΔH	3	0.9	1.7	3.7	1.2	1.9	0.7
	ΔG	6	2.4	2.0	2.9	1.7	2.1	1.9
anionic reactions	ΔH	4	1.3	1.5	3.3	1.1	1.7	0.8
	ΔG	6	1.3	2.1	3.6	1.6	2.2	1.4
cationic reactions	ΔH	1	2.8	0.8	2.8	1.3	0.7	2.0
	ΔG	4	3.1	0.9	1.6	1.5	0.6	2.1
all reactions	ΔH	5	1.7	1.4	3.2	1.2	1.6	1.2
	ΔG	10	2.2	1.7	3.0	1.6	1.8	1.7

Table 2.3: RMS errors for associative ligand exchange reactions

Reaction	Thermo.	Exp.	Deprotonation Energies (kcal/mol) Density Functionals B3LYP	BP86	M06	mPW	PBE	SB98
Prot-1	ΔG	9.6	1.9	-0.6	3.5	4.3	-0.5	3.9
Prot-2	ΔG	7.1	0.9	-1.1	1.9	2.8	-1.1	2.7
Prot-3	ΔG	11.3	3.4	0.2	4.9	6.0	0.3	5.4
Mean Errors	ΔG	–	-7.3	-9.8	-5.9	-5.0	-9.8	-5.3
RMS Errors	ΔG	–	7.3	9.9	6.0	5.0	9.8	5.4
RMS Errors with correction	ΔG	–	0.7	1.2	0.5	0.5	1.2	0.7

Table 2.4: Calculation results for deprotonation reactions

Chapter 3

The Mechanism of Olefin Oxidation via $Pd(II)Cl_2$: The Wacker Process

3.1 Abstract

The mechanism of aqueous $Pd(II)Cl_2$ mediated olefin oxidation reaction (the Wacker reaction) has been studied with first-principles quantum mechanics with special emphasis on determining competitive pathways that explain the reaction's dependence on reaction conditions. Our studies used density functional theory (DFT) methods, including geometries optimized in Poisson-Boltzmann (PB) continuum solvation, to predict the free energies of structures (including saddle points). Our data, along with our interpretations of seminal experimental work were used in determining the nature of the experimentally determined rate laws for the reaction under high and low $[Cl^-]$ concentrations. Our results indicate that the rate-determining step under low $[Cl^-]$ conditions is not hydroxypalladation as generally believed, but an internal rearrangement that occurs after a concerted internal hydroxypalladation and deprotonation. The rate-determining step (RDS) under high $[Cl^-]$ conditions is chloride dissociation after external attack by water. The switch in mechanisms is caused by the prerequisite dissociation of Cl^- prior to internal attack, which is inhibited by increased $[Cl^-]$.

Post-nucleophilic attack, the reaction proceeds through a series of quasi-isoenergetic rearrangements including facile β-hydride elimination. The last step of the process, formation of acetaldehyde coupled with reduction of Pd(II) to Pd(0), occurs through a previously reported mechanism, best described as a water-catalyzed reductive deprotonation.

3.2 Wacker process historical context

The Wacker process—olefin oxidation via a $Pd(II)Cl_2$ catalyst—was a breakthrough for the fabrication of organic chemicals and palladium catalysts, and today is widely regarded as a historic milestone in industrial homogeneous catalysis[31, 32]. Though the wide use of the reaction has been phased out in favor of other economical and environmentally-friendly processes, the Wacker process has seen a small renaissance over the last decade as chemists investigate analogs of the well-studied reaction in fields mostly relating to natural product synthesis[33, 34, 35].

The Wacker process was first identified by Smidt and co-workers at Wacker Chemie and is summarized as a combination of three known reactions: an efficient olefin oxidation reaction[36] (eq. (3.1a), Figure 3.1) is made catalytic with $Cu(II)Cl_2$[37, 38, 39] and O_2[40, 41, 42] as oxidizing agents (eq. (3.1b) and (3.1c), respectively). Details about reaction procedures can be found in the following references:[39, 43, 44]. Subsequent work over half a century has identified many important points of the

$$C_2H_4 + Pd(II)Cl_2 + H_2O \rightarrow CH_3CHO + Pd(0) + 2HCl \quad (3.1a)$$
$$Pd(0) + 2Cu(II)Cl_2 \rightarrow Pd(II)Cl_2 + 2Cu(I)Cl \quad (3.1b)$$
$$2Cu(I)Cl + 2HCl + 1/2O_2 \rightarrow 2Cu(II)Cl_2 + H_2O \quad (3.1c)$$
$$\text{Net} : C_2H_4 + 1/2O_2 \rightarrow CH_3CHO \quad (3.1d)$$

Figure 3.1: The Wacker process reaction equations

Wacker process[44, 45, 46]; however, some essential aspects remain unexplained.

Chief among these points is the nature of the nucleophilic attack, particularly why experimental evidence indicates that either internal or external nucleophilic attack on the coordinating olefin can occur under different reaction conditions. Well-designed experiments over the past decade have presented the existence of two competing mechanisms with different rate laws that yield different products. A detailed analysis to explain why this phenomenon occurs has not been presented until now.

Though the Wacker process is one of the most extensively studied homogeneous catalytic reaction mechanisms, it still lacks a unifying mechanistic model that addresses and is in full accord with the large body of studies on it. Many journals[47, 48], reviews[49, 50], and even text books[31, 32, 51] have presented misinformation about the complexity of this archetypal organometallic reaction. Recent advances in quantum chemical methods now allow for techniques for accurate determination of homogeneous catalysis mechanisms, including those that contain zwitterionic intermediates and transition states that would only be seen with the application of efficient implicit solvation techniques.

Starting from the results of critically important experiments, we investigated the olefin oxidation cycle of the Wacker process using accurate density function theory (DFT) and implicit solvation to find a mechanistic model that is consistent with experimental work. With our calculation data, we reproduced the crossover point for two competing mechanisms and outline both full mechanisms identifying all key intermediates in the olefin oxidation cycle.

3.3 Previous mechanistic investigations

3.3.1 Evidence of an inner-sphere pathway

Smidt and co-workers originally determined the rate law under industrial conditions to be first-order in catalyst and olefin, inverse first-order in protons, and inverse second-order in chloride ions, (3.2)[39]. The industrial Wacker process is run under low [Cl^-] ([Cl^-] $\leq$ 1.0M), in acidic solution (pH = 0–2), near room temperature (20–25°C), and can yield oxidized products at $\sim$ 90% yields on an industrial scale. Hydrochloric acid is readily formed, and thus the pH of the reaction is quite low.

$$\text{Rate} = \frac{k[PdCl_4^{2-}][\text{olefin}]}{[H^+][Cl^-]^2} \tag{3.2}$$

More experiments brought several interesting points of this reaction to light. First, studies done with C_2H_4 in D_2O solvent showed that all four H atoms from the reactant olefin remain in the final oxidized product, CH_3CHO. Likewise, studies with C_2D_4 in H_2O yielded exclusively CD_3CDO product[39]. This result is relevant as it shows that while H atoms must transfer, an expectedly facile route for product formation via keto-enol tautomerization is impossible.

Second, there was no substantial kinetic isotope effect (KIE) in runs with C_2D_4, k_H/k_D = 1.07[39], however a small but significant competitive KIE (k_H/k_D=1.7) was found when using 1,2 dideuteroethene[52]. The lack of the first KIE identifies that hydride-transfer is almost certainly not the RDS, while the existence of the second KIE shows that the rate-determining step must occur before oxidized product formation in (3.1a).

With the rate law and these experiments in mind, Henry performed additional kinetics studies and determined the activation barriers for the Wacker process ($\Delta H^\ddagger$ = +19.8 kcal/mol, $\Delta S^\ddagger$ = -8.7 e.u., $\Delta G^\ddagger$ = +22.4)[53]. To pin-point the rate-

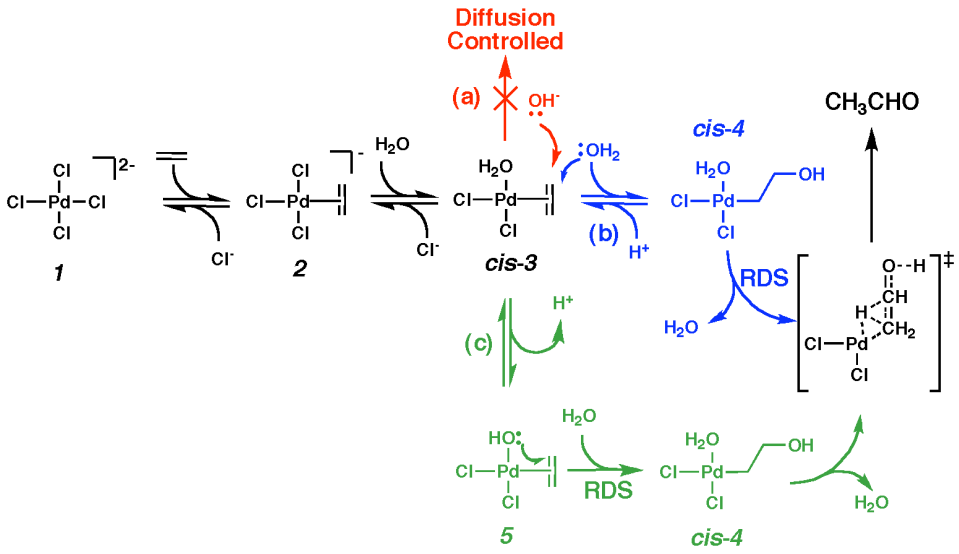

Figure 3.2: Henry's mechanism explaining kinetic observations

determining step, Henry initially considered three possible mechanisms (see Figure 3.2) all starting with fast ligand exchange reactions from **1** → **2** → *cis*-**3** (or *trans*-**3**), and concluding with: (a) external anti-attack by hydroxide on *cis*-**3**, (b) external anti-attack by water on *cis*-**3** (or *trans*-**3**) followed by rate-determining product formation, or (c) an equilibrium deprotonation from *cis*-**3** to **5**, followed by rate-determining internal *syn*-hydroxypalladation, and then fast product formation. A simple kinetics analysis under acidic conditions showed that (a) would need to be faster than a diffusion-controlled process, and is thus impossible. Since the significant competitive isotope effect was found, (b) was ruled out since it implied that product formation could not be rate determining. Thus, by process of elimination, (c) was determined to be the pathway of the Wacker process.

Studies by Moiseev and co-workers found a significant solvent isotope effect was found in D_2O[54]. However, the solvent isotope effect has largely been disregarded as its existence can be rationalized in both pathways (b) and (c).[1]

[1]The same group of investigators also found the rate law depicted in (3.2) is no longer valid when $[PdCl_4^{2-}] > 0.04$ M[55]. The change in rate law was attributed to palladium oligomers that form at higher concentrations of the catalyst, but the existence of this change in rate law is in doubt[44]. Regardless, the experimental conditions required to find this deviation are far removed

Stangl and Jira found that with high concentrations of $CuCl_2$ but with low [Cl^-] and otherwise standard Wacker conditions, chlorohydrin products were formed in small quantities beside oxidized products (with a mass-yield ratio of 1:21)[56]. When [Cl^-] was raised dramatically, generation of chlorohydrin products dominated over oxidized products (mass-yield ratio of 40:9.) This study was later used to recognize a key aspect of the Wacker mechanism which will be discussed later.

3.3.2 Evidence of an outer-sphere pathway

Henry's assertion that the Wacker process proceeds via pathway (c) was put in severe doubt when two independent groups presented different stereochemical studies that apparently showed oxidized products were actually generated via anti-nucleophilic attack. The fact that products were formed in this manner required external attack by water. Although most of these stereochemical studies were drastically removed from normal Wacker conditions and thus not necessarily valid for understanding Wacker oxidation[57, 58, 59, 60], a key study by Bäckvall and coworkers[47] utilized the same medium as the Wacker process, and found that their reaction also underwent *anti*-addition. Follow-up experiments presented additional support for an external attack pathway[61, 48].

The proposed pathway[61] to account for external attack (see Figure 3.3) involved rapid ligand exchange from **1** → **2** → *trans*-**3**, and it followed by external nucleophilic attack to *trans*-**4**, analogous to the first steps of pathway (b) that Henry initially considered feasible. This newer mechanism then involved rate-determining chloride dissociation from *trans*-**4** to *cis*-**6** and then followed an expectedly facile β-hydride elimination (BHE) pathway to form vinyl-alcohol species *cis*-**7**. Subsequent hydride reinsertion from *cis*-**7** results in *cis*-**8** where another expectedly facile BHE was expected to convert to products. Recent calculations found this second BHE

from standard industrial conditions, and so the correction is generally ignored.

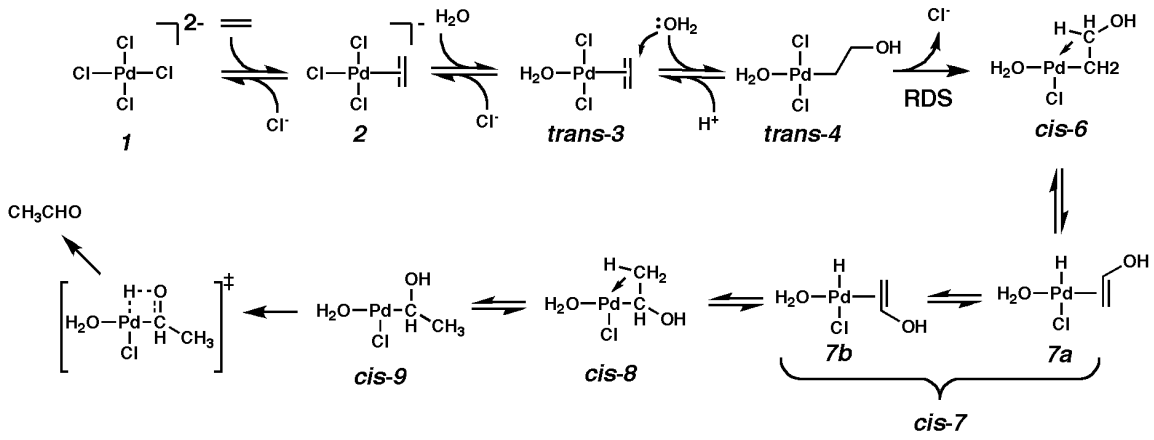

Figure 3.3: Other mechanisms explaining stereochemical observations

reaction to be prohibitively high in energy[62].

At the time, this pathway was attractive in a number of respects, but mostly because they were from elegant stereochemical trapping experiments. Its overall result, that nucleophilic attack occurs via an outer-sphere mechanism, was wholly based on the assumption that reaction conditions do not influence the Wacker mechanism. Despite lingering questions, this mechanism was readily accepted by most of the scientific community, and its impact is still found in the literature and even some modern textbooks.

To show that reaction conditions may play a role in the Wacker mechanism, Henry first designed an allyl-alcohol system that was identified to be oxidized under standard Wacker conditions with the rate law in (3.2)[63]. When used in high [Cl^-] runs, instead of oxidized products, the allyl alcohol isomerized with a different rate law than in normal Wacker oxidation[64]. This new rate law shown by (3.3) is no longer inverse second order in [Cl^-], but inverse first order in [Cl^-], and it also no longer contains a proton inhibition term. In the presence of high [Cl^-] and high [$CuCl_2$], two different products are formed: oxidized products and chlorohydrin. Interpreting this result and the study by Stangl and Jira mentioned earlier, Henry presumed that

$CuCl_2$ played a crucial role in stabilizing the tri-chloro analog of intermediate, **4-Cl**.

$$\text{Rate} = \frac{k[PdCl_4^{2-}][\text{olefin}]}{[Cl^-]} \tag{3.3}$$

3.3.3 Evidence of pathways dependent on experimental conditions

Now aware of the two rate laws, Henry and his coworkers did a barrage of studies and eventually concluded that the Wacker process proceeds via two different pathways dependent on reaction conditions. Three studies in particular elucidated this:

1. Reactions with a specially deuterated allyl-alcohol, $H_2C = CHCD_2OH$, showed no scrambling to form $D_2C = CHCH_2OH$[63]. This would be an expected result if the nucleophilic attack in pathway between *trans*-**3** and *trans*-**4** were indeed in equilibrium at low $[Cl^-]$.

2. Kinetic probe experiments were designed to prevent an equilibrium external nucleophilic attack explicitly[65]. If external attack proceeded through that same equilibrium, a different rate law without proton inhibition would be expected. Instead, this study yielded the same rate law expressed in (3.2).

3. After showing that both rate laws were reproducible in methanol,[66] stereochemical studies in both water and methanol definitively showing that both *syn*- and *anti*- products formed at rates corresponding to (3.2) and (3.3), respectively[65, 67]. These studies were later even further elaborated upon[68].

During the same time frame as many of these experiments were being run, theoretical studies attempted to add new perspectives to the complicated process. It was believed that nucleophilic attack was a substantial driving force for the reaction by the slipping of ethene from an η-2 coordinated to an η-1-coordinated complex,[69, 70]

however, these models were later shown to be insufficient to make even qualitative predictions[71, 72].

One application of a semi-empirical technique identified that nucleophilic attack was likely rate-determining, but it could not definitively specify if internal attack by hydroxide was rate-determining[73]. This study, however, is noted as the lone exception in the body of theoretical work that supported Henry's conclusions that internal nucleophilic attack would occur.

3.3.4 Summary of previous calculations

The most significant contribution from theory during this period came from Siegbahn, who found a model that apparently could accurately treat solvation in the Wacker system using both explicit and implicit solvation[74]. With this model, Siegbahn concluded that the enthalpic barrier for *anti*-attack by external water was lower than for *syn*-attack with an external water. (Internal nucleophilic attack by hydroxide as Henry originally proposed was never calculated in full.) The ramifications of this were that if *anti*-attack pathway was calculated so low in energy, nucleophilic attack might still be an equilibrium process. This result is in apparent disagreement with the results from the three experiments mentioned above. A possible reason for this discrepancy might be because Siegbahn's calculations made no corrections to account for [Cl^-], nor the entropic effects from H_2O. Additionally, his treatment of Cl^- implied reaction conditions of [Cl^-] = 1 M, a value that is relatively close to the experimentally determined cross-over point for [Cl^-] = 2 M, so it is uncertain which conditions his calculations were presenting.

In addition to showing that external nucleophilic attack would be low in energy, Siegbahn also found that the barrier height for the BHE step forming *cis*-**7** was high but it was too close to tell whether it would be the activation barrier for the Wacker process. If it were to be the rate-determining step, that would have been in apparent

disagreement with the first KIE experiment by Smidt and coworkers[39].

Lastly, Siegbahn presented a reason why keto-enol tautomerization does not occur. His calculations showed that the tautomerization barrier was +16 kcal/mol with respect to **5**, but the overall barrier was more than 25 kcal/mol.

Computational simulation of the Wacker process has since been relatively scarce. Apart from the study on BHE mentioned previously, the only other computational mechanistic study on Wacker oxidation involved very different reaction conditions[75, 76].

3.3.5 Challenges for modern calculations

While illuminating, the whole of all experimental and theoretical studies left a sizable question unanswered: Are the barriers for the proposed rate-determining steps for the competing mechanisms presented by Bäckvall (Cl^-dissociation) and Henry (internal nucleophilic attack by hydroxide) realistic? No theoretical calculation had adequately found RDSs at this point, nor were concentration effects ever taken into account to model a reaction clearly dependent on concentration effects.

Another addressable issue is why Siegbahn's simulation showed that external attack by water is low in energy while a multitude of experiments show that this pathway should be prohibitive. Such clear disagreements make for bad relations between theorists and experimentalists.

Lastly, while it was shown that the Wacker process can proceed through two different pathways, a conceptual understanding of the intimate details for what is happening would be of great interest. A thorough mechanistic study was necessary to address these questions and understand the root cause of this switch in mechanisms.

3.4 Modern insight through computational simulations

3.4.1 Simulation methods

Calculations were carried out on the Jaguar suite of programs using the density functional theory (DFT) method, B3LYP[6].

A Los Alamos basis set, LACVP, with effective core potentials (ECP) by Hay and Wadt[77, 78] and additional polarization functions (LACVP**, overall, a variant on Pople's 6-31G** basis set) was applied. This particular basis set is comparable to Dunning's double-zeta basis set for first and second row atoms. Relativistic effects are folded into the ECP applying an [Ar] core for Pd. This method is known to produce good descriptions of reaction profiles for transition metal containing compounds[79, 80, 81, 62].

We treated all species with implicit solvent effects of water that were calculated numerically with the Poisson-Boltzmann continuum approximation[14, 15], using the parameters $\epsilon = 80.37$ and $r_{solvent} = 1.400$Å. The solute cavity is defined by the surface of closest approach as a sphere of radius $r_{solvent}$ is rolled over the van der Waals envelope of the solute. The charge distribution of the solute is represented by a set of electrostatic potential (ESP) fitted charges. In this paradigm, the charge density of the solute is placed inside the solute cavity in the form of ESP charges. Although this is an approximate description of solvent effects, the method is remarkably accurate, and it circumvents some errors related to the penetration of the solute electron density beyond the solute cavity.

Siegbahn's study identified the crucial importance of a good solvation model. Technological advances since Siegbahn's study now permit calculation of solvation corrections at the end of each geometry iteration to account for electronic stabiliza-

tion to obtain the overall lowest energy structure. This process can typically increase the computation time by a factor of ~ 4 compared to a single-point solvation correction added to the gas-phase optimized energy, but it is the purest way to identify zwitterionic species that would otherwise be unstable during gas-phase optimizations. We found that this method was better suited for calculating relative free energies than the 3-water chain model mentioned earlier.

For this study we considered using other forms of density functionals including PBE, MPW1K, and BP86, and considered various basis sets including the triple-zeta LACV3P**. After a comparison of calculations reproducing experimentally known thermodynamics of inorganic species involving Pd and Pt metals with Cl^- and H_2O ligands, we found this method—PBF-solvent optimized structures with the B3LYP/LACVP** level followed by B3LYP/LACVP**++ single point calculations—to be the most effective for reproducing both barrier heights and relative energies of anionic Pd complexes.

Since frequencies calculated in the Poisson-Boltzmann continuum are computed numerically in Jaguar, some small imaginary frequencies corresponding to low-energy torsions of coordinated waters (from -5 to -80 cm^{-1}) could not be avoided. This indicates a flaw in the numerical frequency calculation and thus not necessarily a flaw in the geometry optimization. Furthermore, since the imaginary frequencies in question correspond explicitly to the torsion of water bound to Pd, they should not contribute to the vibrational partition function. Our treatment of these cases involved recalculating all thermodynamic properties dependent on vibrations with vibrations of 50 cm^{-1} substituted in place of all frequencies (positive or negative) below 50 cm^{-1}.

All calculation results are in a standard-state formalism where all calculated species are presumed to be at an infinite dilution limit. With these values we employed the steady-state approximation to analyze the flux of the reaction pathways at varying concentrations of $[Cl^-]$ and $[H^+]$ to reproduce kinetic rate laws. In a test set

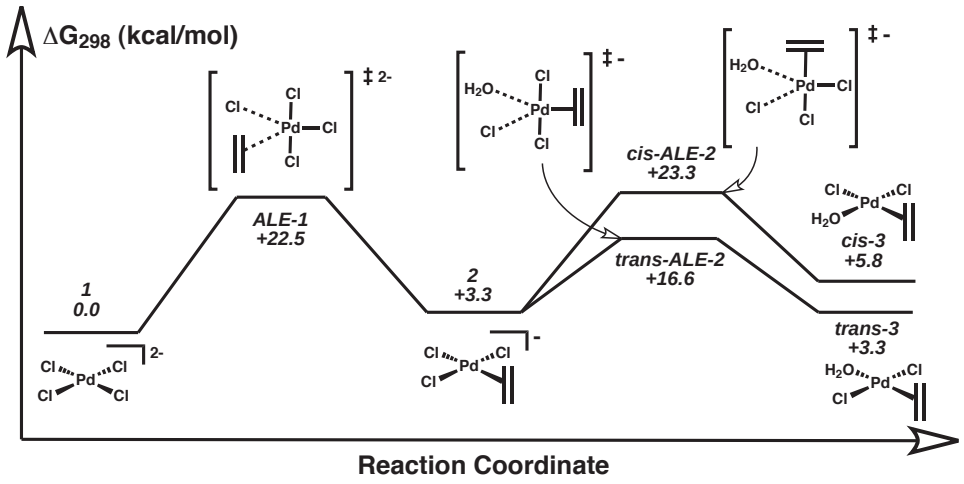

Figure 3.4: Ligand exchange reactions in the Wacker process

of established ligand exchange reactions, our method reproduced both experimental barriers and relative free energies of anionic transition metal complexes in solution with an RMS value of < 1.5 kcal/mol. These errors are considered a best-case expectation, however, and the realistic expectation for DFT methods in solution are 2–3 kcal/mol for relative intermediates and slightly higher for transition states.

3.4.2 Ligand exchange reactions

A summary of calculated data for ligand exchange reactions can be found in Figure 3.4.

We began our simulations with the expected initial reactant **1**, tetrachloropalladate. At standard concentrations and pressures our calculations show that the resting state of the catalyst is **1**, 1.4 kcal/mol more stable than $[Pd(Cl)_3(H_2O)]^-$ and 3.3 kcal/mol more stable than **2**. This is in reasonable agreement with experimental thermochemical value where $[Pd(Cl)_3(H_2O)]^-$ and **2** are both 2 kcal/mol greater in energy than **1**. Olefin exchange occurs with a barrier of +22.5 kcal/mol (via **ALE-1**) to form **2**.

After olefin exchange, **2** can undergo another ligand exchange to make the over-

all species neutral and thus more susceptible to nucleophilic attack. This leads to two possible conformations of the species *cis*-**3** (+5.8 kcal/mol) and *trans*-**3** (+3.3 kcal/mol). We find the process to make *cis*-**3**, *cis*-**ALE-2**, is +6.7 kcal/mol higher than the process to make *trans*-**3**, *trans*-**ALE-2**.

While **ALE-1** and *cis*-**ALE-2** are both calculated higher than the known activation energy of the Wacker process, (+22.4 kcal/mol), the barriers are still within calculated error less than the experimentally observed activation energy. Additionally, *cis*-**ALE-2** is expected to be not rate-determining as the established rate law, (3.2), has second order inhibition in [Cl^-] and corresponds to *syn*-products which is believed to require the existence of *cis*-**3**.

3.4.3 Nucleophilic attack processes leading to *anti*-products

We begin our analysis of the controversial nucleophilic attack process by investigating various external attacks by water on intermediates **2**, *cis*-**3**, and *trans*-**3**. As mentioned earlier, an advantage to using solvent-optimized structures is the capacity of locating intermediates and transition states that normally would not be stable in gas phase. External nucleophilic attack immediately results in a zwitterionic species, and we could effectively simulate these species with one single water molecule, thus reducing conflicts incorporating the explicit solvent molecules. We were unable to determine barrier for external attack by hydroxide, however we note that this pathway was deemed impossible in a previous study. Our results are summarized in Figure 3.5. We find that external nucleophilic attack by water should be considered a feasible rate-determining process under standard Wacker conditions. The overall barrier heights for external attack, **EXT-1**, *cis*-**EXT-2**, and *trans*-**EXT-2** are +22.7 kcal/mol, +23.9 kcal/mol, and +18.2 kcal/mol, respectively. All are calculated within the margin of error in calculations to be in agreement with the activation barrier for

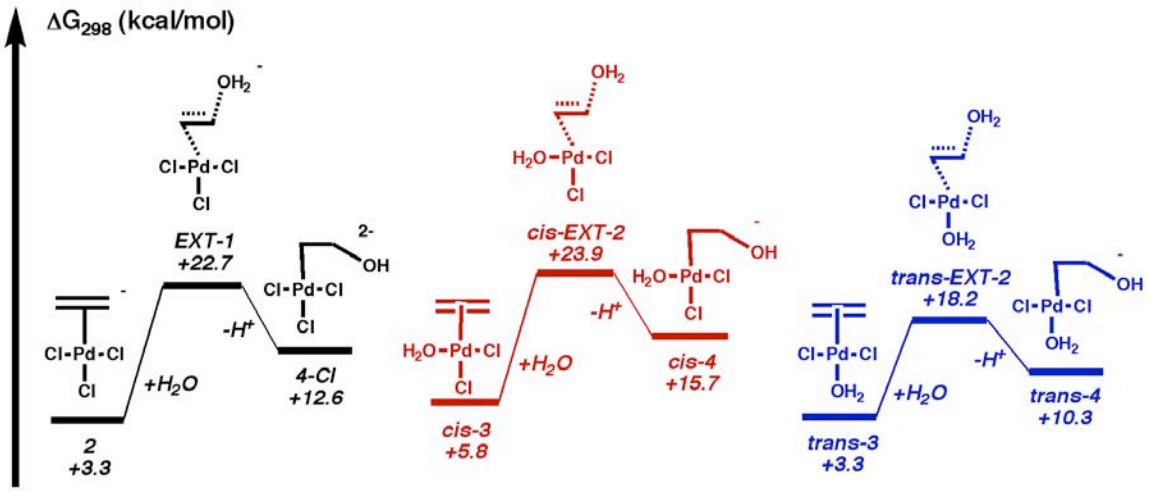

Figure 3.5: *Anti*-nucleophilic attack processes

Wacker process, with the exception of *trans*-**EXT-2** which is lower than we would expect.

Based on (3.2) alone, we know that **EXT-1** *cannot* be rate determining under industrial conditions. However, it is feasible that this process could be rate determining under the conditions that lead to (3.3). Likewise, based on (3.2) alone, it would be possible that either *cis*-**EXT-2**, or *trans*-**EXT-2** could be rate determining, however the observation of *anti*-products rules that out as a possibility, and our calculations must be over stabilizing the energetics of *trans*-**EXT-2**. This associated error would be ~ 4 kcal/mol, which is not outside of the errors in our methods.

We add that it is unlikely that any external attack pathway is lower than the activation energy for the Wacker process since experiments using isotope-substituted vinyl alcohols as the olefin reagent found no scrambling of hydroxide groups (see Figure 3.6). Henry's interpretation of this experiment[63] was that nucleophilic attack by water would need to be rate determining. We do not go so far to say that, but we agree that *external*-nucleophilic attack would need to be rate determining given this observation. Additionally, even if the barrier associated with *trans*-**EXT-2** were slightly lower than **EXT-1**, it is possible that variable [Cl^-] would effect the stability

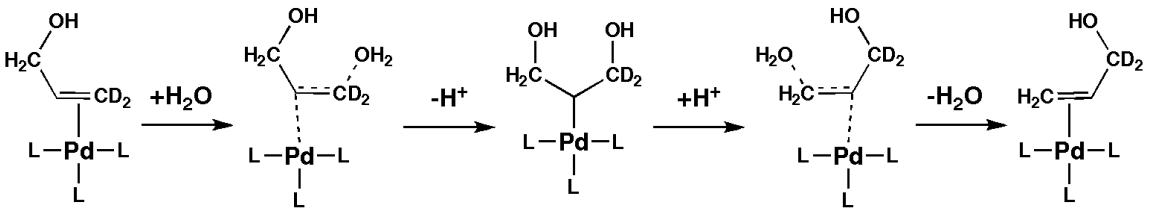

Figure 3.6: Isotope-substituted vinyl-alcohol experiments

of the product *trans*-**4** and thus the degree that scrambling may or may not occur.

Lastly, these calculations resolve an issue with the previous work by Siegbahn. Siegbahn found that the enthalpic barrier for external attack was far too low to be rate-determining ($\Delta H^{\ddagger}_{298} = 5.7$ kcal/mol)[74]. Likewise, we find the enthalpic barrier for this process is similarly low ($\Delta H^{\ddagger}_{298} = 8.7$ kcal/mol). However, neither calculated barrier height treats the entropic effects of water in the transition state which causes the free energy barrier to be +10.1 kcal/mol higher than the enthalpic barrier. Thus, the previous deductions by Siegbahn may not be valid since they were based on only enthalpic quantities.

3.4.4 Nucleophilic attack processes leading to *syn*-products

We now consider internal nucleophilic additions of water to yield *syn*-products in the Wacker process. In Henry's original mechanism (Figure 3.2), *cis*-**3** must undergo a facile deprotonation in order to account for the proton inhibition in (3.2). We find that this deprotonation is uphill by 12.0 kcal/mol, however the new intermediate, **5**, is still energetically lower (+15.3 kcal/mol) than the Wacker process activation energy.

According to Henry's hypothesis, **5** should then undergo hydroxypalladation to form a new intermediate where a C-O bond is formed. The simplest transition would involve the transfer of hydroxide into an intermediate, **10**, where the O atom bound to both Pd and C (Figure 3.7). We find that the energy of **10**, +15.9 kcal/mol, should allow it to be a stable intermediate. However, we were surprised to find that this barrier was prohibitively high in energy (+33.4 kcal/mol). Addition of explicit

water molecules did nothing to further stabilize this transition state.

Henry's original proposal had a concerted process that involved water simultaneously entering the ligand binding site as the hydroxypalladation occurred. Attempts to find this transition state invariably failed, resulting in transition states similar to the previously mentioned hydroxypalladation transition state. However, we considered a process where **5** would undergo external nucleophilic attack by water. The resulting product of this process would be *cis*-**4**. The calculated barrier for this process, +24.6 kcal/mol, is much more likely than hydroxypalladation as Henry hypothesized. For completeness, we also considered external *syn*-nucleophilic attacks from **2**, *cis*-**3**, and *trans*-**3**, however, none of these barriers were found to be energetically lower than **INT-2**, nor their *anti*- analogs, **EXT-1**, *cis*-**EXT-2**, and *trans*-**EXT-2**, discussed in the previous section.

Lastly, we considered the possibility that *cis*-**3** could undergo a water-catalyzed inner-sphere nucleophilic attack. In this process an explicit solvent water deprotates the bound-water in *cis*-**3** as it transfers to form **10** + $\mathbf{H_3O^+}$. The barrier for this process, **INT-3**, is only +18.0 kcal/mol.

Observant readers may now be puzzled with this result. If our calculations were in error and **INT-3** actually was the rate-determining step of the Wacker process, then *syn*-products would be formed according to a rate law that is neither (3.2) nor (3.3). If **INT-3** were not the RDS of the Wacker process, then a subsequent barrier after **10** would need to be the RDS. Hence, we deduce that the most feasible pathway for internal nucleophilic attack leading to *syn*-products is inner-sphere attack by water with a simultaneous deprotonation.[2]

[2]Readers may recall that we dismissed the barrier of **EXT-3** as erroneously calculated too low while **INT-3**, which was essentially isoenergetic with **EXT-3**, has just been accepted as feasible. It should be stated that experimental observations based on the rate laws (3.2) and (3.3) direct our conclusions made from our computational studies. One might make the argument that a fully consistent explanation would involve **INT-3** being calculated too low in energy and the actual RDS is **INT-2**, however we calculated it too high in energy. While this would violate *Occam's Razor*, it is an entirely possible conjecture that should not entirely be ruled out.

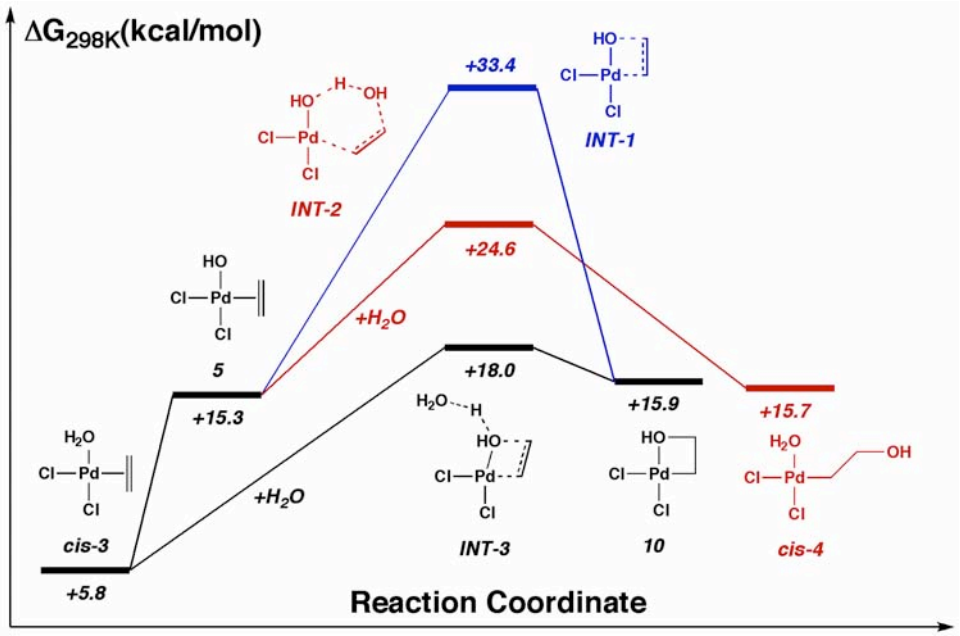

Figure 3.7: *Syn*-nucleophilic attack pathways

3.4.5 A unified model explaining concentration effects

To recapitulate, our calculations identify the lowest energy pathway for internal nucleophilic attack as going through non-rate determining **INT-3**, which is +18.0 kcal/mol. A higher-energy transition state following **INT-3** would result in the observed rate law in (3.2).

We also identify the lowest energy pathway for external nucleophilic attack as *cis*-**EXT-2**, however if this pathway were accessible under industrial Wacker conditions, one would see *anti*-products rather than actually observed *syn*-products, and this is not the case. While not consistent with our calculations on *trans*-**EXT-2**, **EXT-1** being the RDS at non-industrial conditions is consistent with the rate law in (3.3) in addition to observations from all previous experimental findings and our calculations.

One additional component besides [Cl^-] needs to be addressed. The role of $CuCl_2$ is a feature of the Wacker process that is rarely discussed in experimental and theoretical studies alike. We summarize the experimental observations of the four possible reaction conditions for olefin oxidation as follows:

- **LL conditions (industrial conditions:** Reactions utilizing low [Cl^-] (< 1M) and low [$CuCl_2$] (< 1M) yield only aldehyde products, via internal *syn*-addition according to the rate law shown in (3.2).

- **HH conditions:** Reactions utilizing high [Cl^-] (> 3.0M) and high [$CuCl_2$] (> 2.5M) yield *both* aldehyde and chlorohydrin products, via external anti-nucleophilic addition according to the rate law in (3.3)[68].

- **HL conditions:** Reactions utilizing high [Cl^-] and low [$CuCl_2$] yield no oxidation. Instead, reagents using substituted olefins isomerize according to the rate law in (3.3)[64].

- **LH conditions:** Reactions utilizing low [Cl^-] and high [$CuCl_2$] yield both *syn*- and *anti*- products with a combined rate law involving (3.2) and (3.3)[82].

Regardless of the conditions, H/D mixing is never seen in products when reactions are run in D_2O. This fact leads us to believe that the product formation pathway of the innersphere *syn*-pathway will share several intermediates as the product formation pathway of the outersphere *anti*-pathway. It is reasonable to imagine that both innersphere and outersphere pathways could rely on a single pathway starting from intermediate **6-Cl**, which would then form Pd-H intermediates such as **7a-Cl** and then form oxidized products (see Figure 3.8).

We believed intermediate **8-Cl** was a reasonable intermediate through which oxidized products were formed, and we backtracked from **8-Cl** to decide that **7a-Cl** (+15.4 kcal/mol) and **6-Cl** (+17.0 kcal/mol) were reasonable intermediates that would all lie on the mechanistic pathway after nucleophilic attack. The remaining question was how the innersphere and outersphere mechanisms may unite into **6-Cl**. In order for the innersphere *syn*-pathway to reach **6-Cl**, an intramolecular isomerization, **TS-ISO**, would need to take place after **10**. This isomerization is simply a

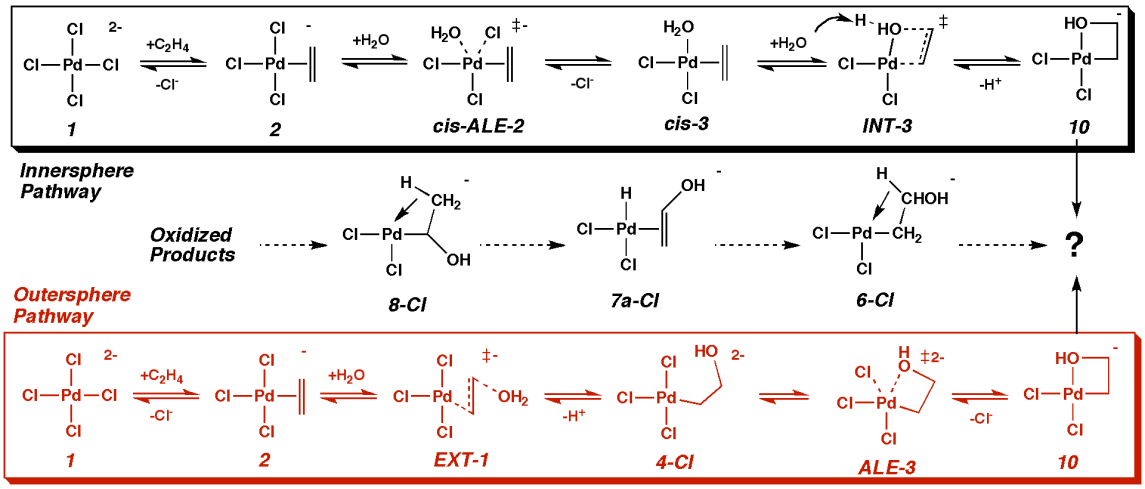

Figure 3.8: Toward a unifying mechanism

120° rotation about the C-C bond. The barrier for this process is +23.2 kcal/mol, high enough to be considered the RDS of the *syn*-pathway, and the resulting rate law would also coincide with that in (3.2).

For the outersphere mechanism, assuming that **4-Cl** were formed via **EXT-1**, **4-Cl** would need to dissociate one of its Cl^- ions in order to become monoanionic like **6-Cl**. One possible process is **ALE-3**, where the alcohol group of **4-Cl** undergoes an associative ligand exchange to form **10**, which then would pass through **TS-ISO** to reach **6-Cl**, the β-agostic complex. The barrier for **ALE-3** is +17.8 kcal/mol – low enough to not be considered a feasible RDS.[3]

With our calculated results, we present the following mechanistic pathways that center around three key transition states: *cis*-**ALE-2**, **EXT-1**, and **TS-ISO**.

- *syn*-addition pathway: The sequence [**1** → **2** → *cis*-**-ALE-2** → *cis*-**3** → **TS-INT3** → **10** → **TS-ISO** → **6-Cl**] would yield oxidized products from *syn*-nucleophilic attack with a rate law corresponding to (3.2) if **TS-ISO** were the RDS.

[3]Alternatively, calculations also show that a step-wise variant to this process should also be possible. Also, since this stepwise process follows the presumed outer-sphere RDS, it would have no effect on the rate equation.

- *anti*-addition pathway: The sequence [**1** → **2** → **EXT-1** → **4-Cl** → **ALE-3** → **10** → **TS-ISO** → **6-Cl**] would yield oxidized products from *anti*-nucleophilic attack with a rate law corresponding to (3.3) if **EXT-1** were the RDS.

In order for this model to be valid, two issues with our calculations would need to be resolved. (1) Our calculated value of **EXT-1** would be calculated too low, as **EXT-1** should be > **TS-ISO**. (2) Our calculated value of *cis*-**ALE-2** is slightly too high, as it should be < **TS-ISO**. These differences are well within the calculated margin of error, however.

Adding explicit $CuCl_2$ to our calculations gives a refreshingly clear view of this mechanism. $CuCl_2$ stabilizes **TS-ISO** by -6.0 kcal/mol, **EXT-1** by -1.9 kcal/mol, but destabilizes *cis*-**ALE-2** by +2.7 kcal/mol. This causes the key barrier on the outer-sphere pathway, **EXT-1** to become accessible and a key barrier on the inner-sphere pathway, *cis*-**ALE-2** to be impassible, selectively favoring the *anti*-addition pathway.

Thus, at **LL** conditions, our calculations can correlate to a pathway that would result in the correctly observed product with the correct rate law, within a small degree of error. At **LH** conditions, our model qualitatively predicts that both pathways will be accessible as both **EXT-1** and *cis*-**ALE-2** will be at or under the activation energy needed for oxidation. At **HH** conditions, the inner-sphere process will be halted at the barrier for *cis*-**ALE-2**, allowing only the opened path through **EXT-1**, which would then lead to acetaldehyde and chlorohydride products. Lastly, at **HL** conditions both pathways will be shut off due to the preference of Cl^- to bind to Pd.

The implications of these changes would also result in an observation not yet experimentally found—that the rate law in (3.3) is not completely adequate in describing **HH** concentrations, but rather a new expression showing the rate of *formation* of

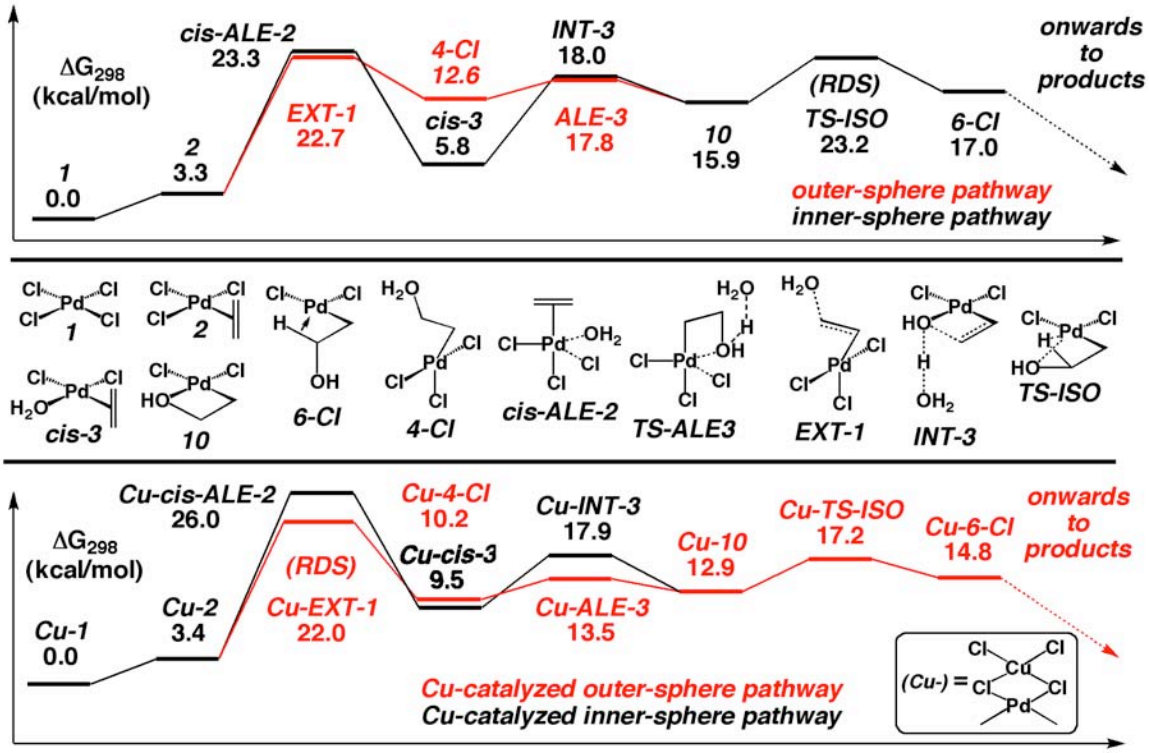

Figure 3.9: Calculation summary of Wacker process reactions with and without $CuCl_2$

products would lead to (3.4).

$$\text{Rate} = \frac{k_{acetaldehyde}[PdCl_4^{2-}][\text{olefin}][CuCl_2]}{[Cl^-]} + \frac{k_{chlorohydrin}[PdCl_4^{2-}][\text{olefin}][CuCl_2]^2}{[Cl^-]} \tag{3.4}$$

This new rate expression takes into account not only the reliance on $CuCl_2$, but also the fact that the rate of chlorohydrin formation increases with increasing concentrations of $CuCl_2$[45].

A summary of calculated results can be seen in Figure 3.9.

3.4.6 Product formation processes

After nucleophilic attack, a series of isoenergetic rearrangements take place to shuttle one of the H atoms from the olefin from one carbon to the other. We find that the proposed mechanism by Bäckvall and coworkers is feasible. Starting from **6-Cl**, β-hydride

elimination (**7-Cl**) is +18.1 kcal/mol and formation of the immediate vinyl-alcohol species is +15.4 kcal/mol (**8a-Cl**). Interestingly, this vinyl-alcohol species appears to prefer having its C-C bond eclipsed with the Pd-H bond, suggesting substantial overlap with the π-system of the vinyl-alcohol is stabilizing this intermediate. A 180° rotation about the η-2 bond of **8a-Cl** leads to **8b-Cl**, which is slightly higher in energy, +17.3 kcal/mol.

It was from this point the one might imagine keto-enol tautomerization occurring. However, since experiments found that all four H-atoms from the olefin remain on the final oxidized product, this would be impossible. To verify why this is the case, Siegbahn identified the barrier for keto-enol tautomerization to be > 25 kcal/mol.[74] Likewise, our calculated value, +29.1 kcal/mol (**KETO**) is in accordance with this value. On a lower energy intermediate, keto-enol tautomerization would surely be facile. It is the fact that the Pd-H intermediate is relatively unstable by ~ 15 kcal/mol that makes this process prohibitive.

Dating back to Henry's original kinetics experiments on the Wacker process, Henry proposed a mechanism for product formation that involved coupling between the Pd-H bond and the deprotonation of the vinyl-alcohol. The difference between this mechanism and the hydride reinsertion step is that the former process involves a reduction, which presumably might be facilitated by deprotonation with a solvent water. We find this barrier (**Prod-1**) similarly high in energy as **KETO**, +31.7 kcal/mol. Therefore, we rule that it is not a feasible process.

From the vinyl-alcohol species, **8b-Cl**, hydride reinsertion (**9-Cl**) has a barrier of +18.0 kcal/mol, essentially identical to the barrier of the first β-hydride transfer. The product of this reaction, **10-Cl** is another β-agostic complex, however, this complex is substantially lower in energy with the formation of the methyl group. It was speculated that β-hydride elimination from an -OH functional group might be the process for oxidized product formation. This pathway was investigated (**BHE**), and

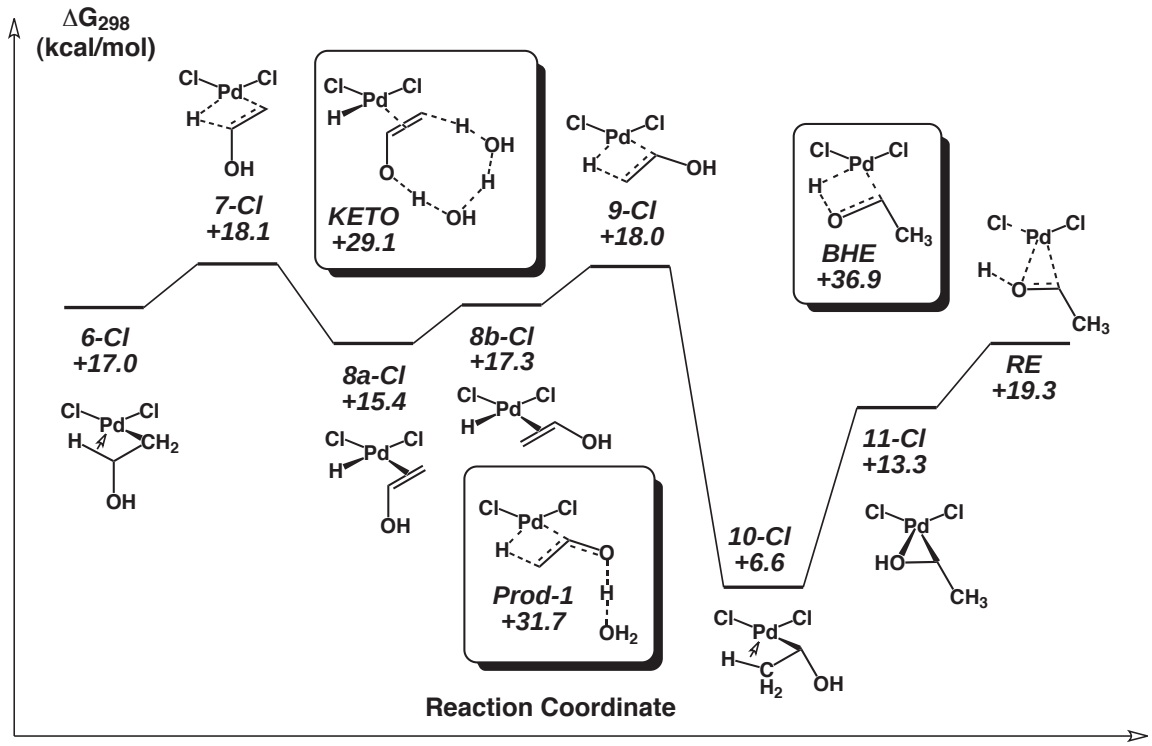

Figure 3.10: Product formation processes in the Wacker process

it was +36.9 kcal/mol. The very high energy of this transition state appears to be the result of two main factors: (1) the electronegativity of O prevents a *hydride* transfer, and instead causes a proton transfer, and (2) a stable intermediate can form where the lone pair on the O atom can bond to the metal (as is the case in **11-Cl**), it is unlikely that the O-H bonding orbital will displace the more diffuse O lone pair.

However, rather than β-hydride elimination, we find another route to form products. This process, characterized by transition state **RE**, is a reductive deprotonation with the capacity to be water-catalyzed. Under the presence of solvent water which can bridge the vacant space between the dissociating Cl^- and proton, this barrier reduces from +19.6 kcal/mol to $\sim$ 10 kcal/mol.

A summary of calculated results can be found in Figure 3.10.

3.4.7 Conclusions from calculations

With the aid of computational simulations, it appears that the multiple questions about the nature of the Wacker process are more completely addressed. Although our mechanistic analysis required simultaneous recognition of experiment, we have presented the first full model of the olefin oxidation cycle in the Wacker process. This model was based on awareness of both the capacity and limitations of both the experiments and the theoretical calculations that were employed over the past half-century. Although subtle details remain (such as experimental confirmation that **INT-3** is an equilibrium process), the freshly identified role of $CuCl_2$ brings a new dimension to the already complicated Wacker mechanisms. Computational studies are underway to investigate the extent that $CuCl_2$ may play a role in other aspects of this reaction, including chlorohydrin formation and reprocessing of Pd(0).

Chapter 4

The Enantioselective Tsuji Allylation Reaction

4.1 Abstract

We propose a mechanism explaining the unique performance of the Tsuji-asymmetrical allylation reaction for prochiral nucleophiles and non-prochiral allyl groups, consistent with experimental findings. Using first principles quantum mechanics (density functional theory), we find that the pathway for this reaction involves the formation of a 5-coordinate Pd-species followed by enantioselective ligand-rearrangement and reductive elimination before generating the product and a Pd(0) complex. This reductive elimination occurs via a seven-centered transition state that contrasts dramatically from the traditional three-centered C-C reductive elimination paradigm. This inner-sphere pathway is more favorable than external nucleophilic attack but is competitive with another inner-sphere pathway, which, when both are accessible, lead racemic mixtures of products. Energetic profiles of several feasible pathways are presented.

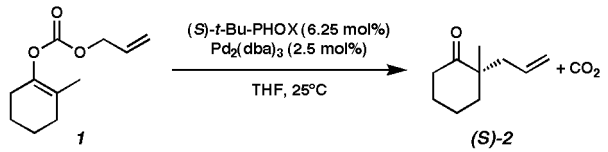

Figure 4.1: The enantioselective Tsuji allylation reaction

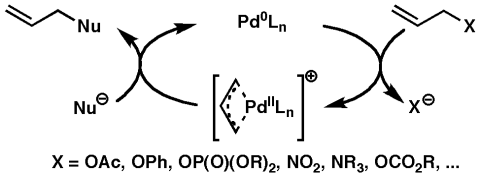

Figure 4.2: The canonical Tsuji allylation reaction

4.2 Experimental background

4.2.1 Allylation reactions

Asymmetric homogeneous catalysis and its roles in the synthesis of natural products and pharmaceuticals has driven organic and organometallic chemistry for decades[83, 84, 85, 86]. A particular challenge has been creation of quaternary stereocenters without the need for chiral reagents.

Recently, we described a new method for the preparation of quaternary stereocenters of high ee[87] based on an enantioselective version of the Tsuji decarboxylation allylation[88]. This catalytic process involves the allylated compound **1** undergoing oxidative addition with a Pd(0) complex. The resulting Pd(II) complex then reacts with carbonucleophiles forming an allylic alkylated product, **2**. This process was found to be particularly useful in asymmetric alkylations, specifically in terms of direct allylation of malonates by prochiral electrophiles by Trost[89, 90, 91, 92, 93], Helmchen[94], and Pfaltz[85].

4.2.2 The enantioselective Tsuji allylation reaction

Mechanistic studies on these asymmetric processes have established that they proceed via an external nucleophilic attacks[95]. This contrasts with several symmetric allylic alkylation mechanisms that are well understood, many of which involve an inner-sphere mechanism terminated with C-C coupling by traditional reductive elimination at the 1 and 1' positions of the nucleophile and allyl fragment[96, 97, 98, 99]. A recent collaboration between our groups have determined that the process we presented likely reacts via an inner-sphere mechanism that is terminated though a non-traditional reductive elimination[100].

Our original study reported the formation of asymmetric quaternary stereocenters from unstabilized ketone enolate nucleophiles and allyl fragment electrophiles[87]. The 2-allyl-2-methyl cyclohexanone products are distinct from the vast majority of asymmetric allylic alkylation products. In contrast to previous works that utilized prochiral electrophiles[85, 88, 89, 90, 91, 92, 94, 95, 101, 102, 103, 104, 105], we demonstrated enantioselective Tsuji allylation using non-prochiral electrophiles and prochiral ketone enolate nucleophiles. This has allowed the regiospecific formation of quaternary centers having two or more acidic sites alpha to the ketone. The products form in high yields and high enantioselectivities, and this process has found success in two other investigations: the total synthesis of (+)-dicroanone[106] and the catalytic enantioselective decarboxylative protonation reaction[107].

The best-performing ligand studied in this system was (*S*)-*t*-Bu-phosphinooxazoline (PHOX) ligand[108, 109] (see Figure 4.3) that provided variants of **2** with yields from of 80–99% and ee's from 79–92%. Although this level of enantioselectivity is useful for many applications, it would be valuable to achieve ee's above 95%, and understanding the intimate details of the mechanism would be a step in the right direction for improving this catalyst system.

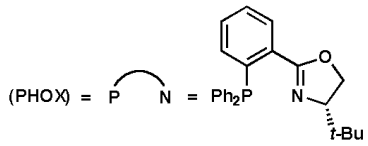

Figure 4.3: The (*S*)-*t*-Bu-phosphinooxazoline (PHOX) ligand

Traditional stereochemical probes with cyclohexenyl electrophiles were employed to elucidate this reaction mechanism, however, experimental yields, dr's, and ee's all dropped considerably in these experiments, suggesting that this reaction is sensitive to these cyclic substrates and a different reaction path was taken. Substantial efforts to develop other experimental tests to elucidate this mechanism have not been successful, thus motivating us to investigate details of the mechanism with quantum chemical simulations.

The observation that this reaction is particularly versatile under enol carbonates, silyl enol ethers, and β-keto allyl esters, while still effective for a variety of reagents and substrates[87, 110] suggested to us that they might share a common intermediate. Additionally, since some reactions performed equally well in polar solvents such as THF and non-polar solvents such as benzene, the mechanism likely was not strongly dependant on electrostatic effects of solvation. Furthermore, we obtained an x-ray crystal structure for a synthesized allylated Pd(II) complex prior to reaction with the nucleophile, suggesting to us that the allylated complex (**3**, see Figure 4.4) is a likely intermediate in the reaction.

Two experiments within our group[100] suggested that we consider just one **Pd-(PHOX)** complex in investigating the mechanism: (1) experiments varying the ee of the catalyst from 0 to 100% showed no non-linear effects in the ee of the product formed, and (2) simple kinetic studies showed that the reaction was roughly zero-order in **Pd(PHOX)** and starting material.

Given the current understanding of the Tsuji allylation mechanism and information stated above, we investigate the mechanism for Tsuji allylation, as illustrated

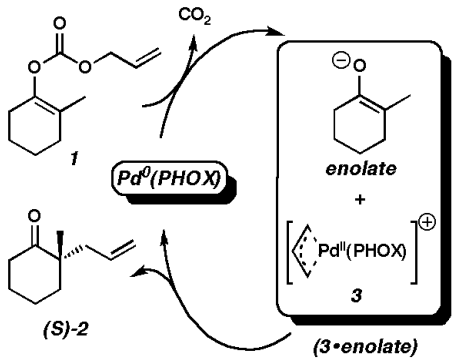

Figure 4.4: Towards a mechanistic hypothesis: The enantioselective Tsuji allylation cycle

by Figure 4.4, using first principles quantum mechanics including effects of solvation (in this study, the effects of the reaction in THF). Our calculations find an inner-sphere mechanism that explains current experimental observations. Additionally, we find results that suggest the enantiodetermining step for this reaction with quantitative agreement with experimental observations. Key to this mechanism, we find a reductive pericyclic rearrangement process that is an alternative to the traditional three-centered process seen commonly in other C-C coupling reactions mentioned previously. Based on the mechanism, we suggest strategies for optimizing the catalyst and the reaction conditions for the process.

4.3 Computational insight

4.3.1 Computational methods utilized

Calculations we report in this study were taken by using Jaguar version 6.5[23], except single-point control calculations which were calculated with Jaguar version 7.0[4]. Simulations involved the full 82-atom system, as reduced model systems were found to not adequately describe steric effects of the PHOX backbone. Molecular geometries were obtained with the B3LYP hybrid DFT method and double-zeta basis set qual-

ity. The B3LYP density functional method[6] utilizes the Becke generalized gradient approximation (GGA) in conjunction with a component of exact Hartree-Fock exchange (hybrid DFT) with the Lee, Yang, and Parr correlation functional, and it has been shown to be quite effective in elucidating important aspects of organometallic reaction mechanisms[62, 79, 80, 81].

In order to expedite simulations, preliminary geometry optimizations were run with a mixed-basis set approach. In this method, the LACVP[77, 78] electronic core potential (ECP) including 18 explicit electrons was used on Pd; the 6-31G* basis set was used on N, P, and the six atoms in the allyl- and enol- fragments; and the MIDI! basis set[16] was used on all other atoms. Vibrational frequencies and consequent thermodynamic contributions were calculated with the mixed basis set as these values were negligibly different from values obtained from more expensive B3LYP/(LACVP*,6-31G**) frequencies. The resulting Hessian was used in geometry optimizations where the LACVP* ECP was used on Pd and the 6-31G** basis set was used on all other atoms. The number of basis functions used in the mixed-basis and full-basis methods were 506 and 782, respectively. We report B3LYP/(LACVP*,6-31G**) geometries.

Although we consider B3LYP geometries calculated from double-zeta basis sets suitably accurate for making structural predictions, predictions on enantioselectivities require at least triple-zeta basis sets to accurately describe electronic energies. Additional single point energy calculations of triple-zeta quality (LACV3P, a decontracted version of LACVP, on Pd with 6-311G**++ on all other atoms) were taken at these B3LYP geometries with hybrid B3LYP, and compared with single-point energies from the hybrid *m*PW1PW91 method[13]. For critical barriers we also report calculations with the highly-parameterized designer DFT method, M05[111, 112]. Lastly, all calculations include electronic relaxations due to THF solvation (basis set = (LACV3P**,6-311G**), probe radius = 2.527 Å, ϵ = 7.52) from single-point

self-consistent Poisson-Boltzmann implicit solvation calculations[14, 15].

To estimate the free energies and enthalpies at reaction temperature, we calculated the analytic vibrational frequencies for the key intermediates. These frequencies were used to calculate the partition function, which was then used to derive the other thermodynamic functions. We only use the calculated vibrational partition function and not the calculated translation or rotation for solvated species. In order to prevent spurious results due to low vibrational entropy energy associated with low vibrational frequencies, we engineered a solution by recalculating the ZPVE and the partition function where all vibrational frequencies lower than 50 cm^{-1} are substituted with values of 50 cm^{-1}. All calculated energy terms are found in the supporting information. Unless explicitly noted, all reported energies in the text are B3LYP ΔG_{298} values including solvation with a triple-zeta quality basis set.

For ease of reading, the figures show only relevant internal coordinate distances for each intermediate. The illustrated atoms are also the nine atoms that were treated with the double-ζ quality basis set in the mixed-basis set calculations. Ball and stick molecular illustrations were made from VMD[113].

4.3.2 Theoretical validation

We calculate the reaction thermodynamics for enol-allyl carbonate converting to 2-allyl-2-methyl cyclohexanone (Figure 4.1) as exothermic by ΔG_{298} = -33.7 kcal/mol in THF. Of this, -15.2 kcal/mol of that energy is associated with the entropy of CO_2 gas in the product. Experimental thermochemical data is not available for this reaction, however these values correspond very well with those calculated from additivity tables (-35 kcal)[114]. All calculated relative energies henceforth will be relative to the final products, (*S*)-**2** + **Pd(PHOX)** + $\mathbf{CO_2}$.

The experimental isolation of $\mathbf{3{\cdot}PF_6}$ and the demonstration that it is a competent catalyst motivated us to start our mechanistic investigation at the ion pair involving

the cationic allyl intermediate, **3·enolate**. The crystal structure of **3·PF$_6$** contained a superposition of two conformers, *exo*-**3** and *endo*-**3**, each labeled based on the orientation its allyl fragment with respect to the metal-center plane. This notation was presented by Helmchen, and we use it to distinguish relevant structures. The isolated product contained nearly equal amounts of *endo*-(49%) and *exo*-(51%) conformations. The C-C-C angle of the allyl fragment is an unrealistic 136.6°, and is most likely due to the unresolvable superpositioning of structures. A Boltzmann distribution of these occupations corresponds to a miniscule energy difference of +0.02 kcal/mol. As shown in Figure 4.5, the predicted structure is in good agreement with experiment, with an RMSD of 0.03 Å with respect to non-CH bond distances and 2.1° for bond angles. The error in bond angles reduces to 1.3° when omitting the C-C-C angle of the allyl fragment (calculated = 119.4°). *Exo*-**3** and *endo*-**3** calculations show they differ by a small energy of only -0.15 kcal/mol (ΔG_{298}(*exo*-**3**) > ΔG_{298}(*endo*-**3**)). This corresponds to an *endo*:*exo* ratio of 56:44 and its error (0.22 kcal/mol), is well within the expected error for our calculations (ca. 2–3 kcal/mol).

4.3.3 Decarboxylation processes

The beginning of this catalytic cycle is expected to begin with **Pd(PHOX)** undergoing oxidative addition with **1**. We find a stable intermediate, **4**, where the reactant, **1**, is coordinated to **Pd(PHOX)** by an η-2 bond from the allyl functional group. This intermediate is +32.6 kcal/mol, suggesting only a 1 kcal/mol η-2 bond energy.

It is noteworthy that the calculated Pd-P bond (R = 2.36 Å) is similar to that in intermediate **3** (2.34 Å), however the Pd-N bond is longer in the Pd(0) species (R = 2.34 Å) versus in the cationic Pd(II) species (R = 2.16 Å). The bond lengths of the allyl fragment: C_1-C_2 and C_2-C_3, are unequal corresponding to the fact the C_1-C_2

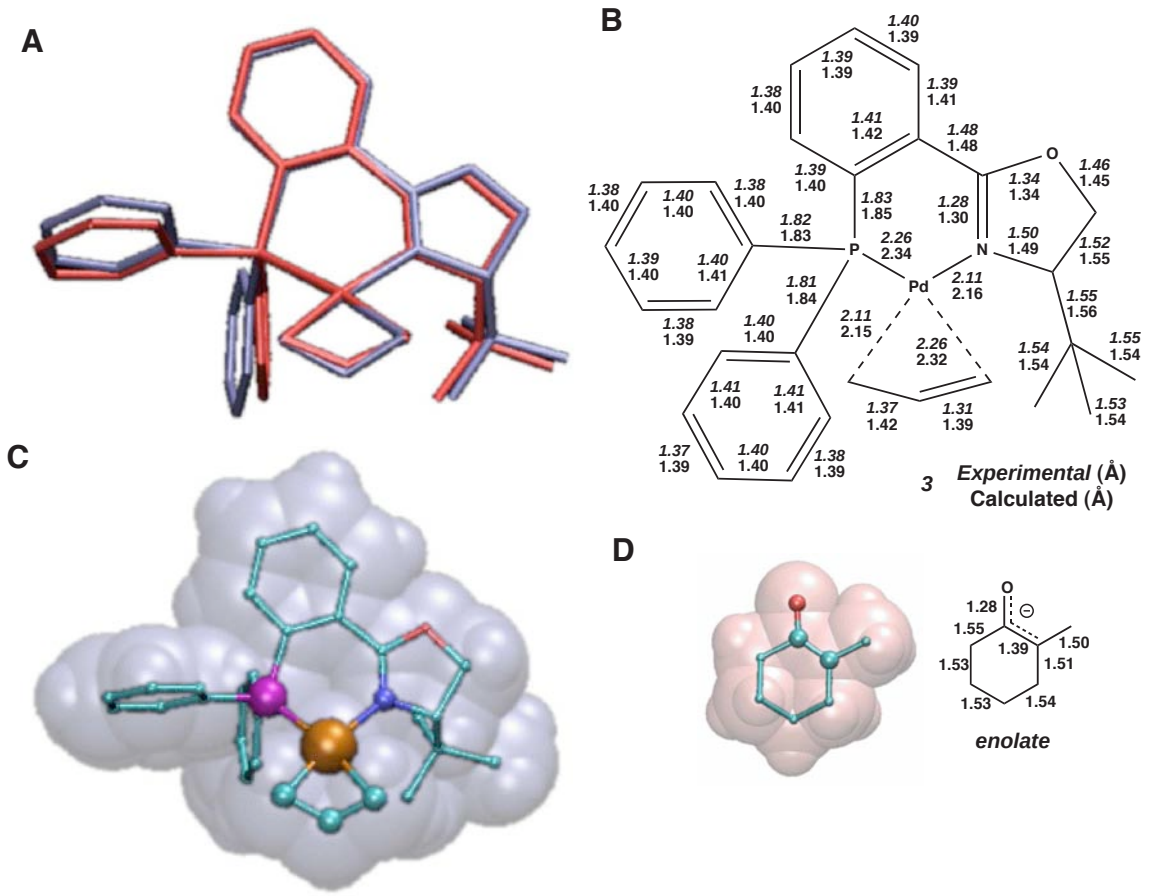

Figure 4.5: (A): Superimposed experimental (red) and calculated (silver) structures of intermediate **3**. (B): Experimental and calculated bond lengths. (C): An illustration of intermediate *exo*-**3**. (D): An illustration of the intermediate **enolate** with calculated bond lengths. All reported bondlengths are in Å.

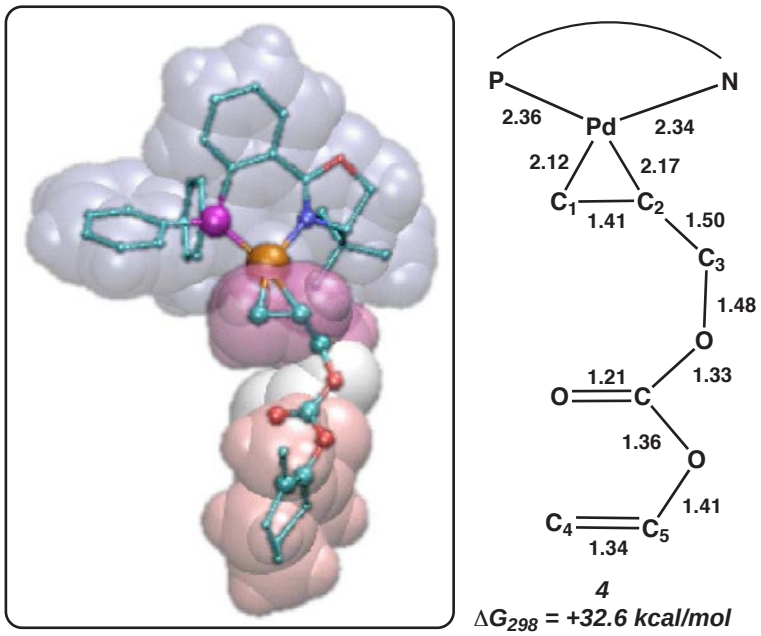

Figure 4.6: Intermediate **4**: η-2 coordinated reactant **1** with **Pd(PHOX)**

is an η-2 coordinated double bond (R = 1.41 Å) while C_2-C_3 is a single bond (R = 1.50 Å). The CO_2 fragment is clearly still isolated within the η-2 bound **1**. The C-O bonds about the carbon of CO_2 show that one distinct C-O double bond is present (R = 1.21 Å).

From intermediate **4**, oxidative addition is possible through one of two transition states: (*exo*/*endo*)**-5**. We find that the preferred oxidative addition mechanism, *exo*-**5** has an overall barrier of +41.9 kcal/mol. We find that this is 3.6 kcal/mol less energetic than *endo*-**5**. Despite this energetic difference, the bond lengths about the Pd metal center show no difference between the two transition states (*exo*/*endo*)-**5**. This energetic difference does seem to be attributed to the fact that when the allyl fragment is *exo*, the CO_2 group can nestle closer to the stereocenter of **Pd(PHOX)** and obtain slightly better non-bonding interactions with the catalyst.

The bond lengths of the two transition states show that the allyl fragment is almost entirely formed where the C_1-C_2 and C_2-C_3 bond lengths have become equivalent (R = $\sim$ 1.41 Å), and the Pd-C_3 bond is slightly longer than the same bond in intermediate

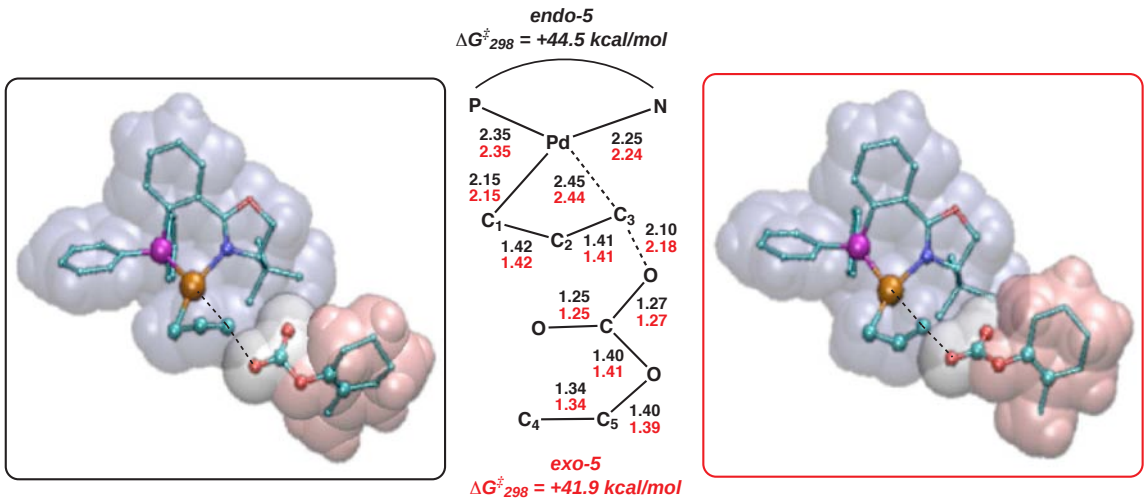

Figure 4.7: Transition states (*endo*/*exo*)**-5**: Oxidative addition leading to allylated **Pd(PHOX)**

3. The Pd-N bond has shrunken slightly to a value (R = $\sim$ 2.25 Å) that is intermediate between the Pd-N bonds of the immediately preceding intermediate **4**. Also of note is that the C-O bonds of the CO_2 group are now essentially equivalent (R = $\sim$ 1.26 Å). All these geometric observations point to the fact that oxidative addition is a late transition state for these complexes.

Post oxidative addition, newly formed cationic intermediate **3** will likely form into an ion pair with the anionic CO_2-bound enolate. We found the most stable ion pair formation was actually a single 5-coordinate complex, *exo*-**6**, where the CO_2-bound enolate was bound at an axial position to the Pd of **3**. This intermediate is +33.5 kcal/mol, and roughly isoenergetic with the reactants **1** + **Pd(PHOX)**.

The Pd-O bond of this 5-coordinate intermediate is relatively long (R = 2.62 Å), but all other bond lengths about the Pd atom are consistent with those in **3**. The C-O bonds in the CO_2 fragment are equivalent to those from the transition states (*exo*/*endo*)**-5**. Experiments with carboxylate reagents find a release of CO_2 as the reaction proceeds, and so a decarboxylation reaction needs to be identified. From *exo*-**6**, the O atom residing on the enolate can approach the Pd of **3**. In the process

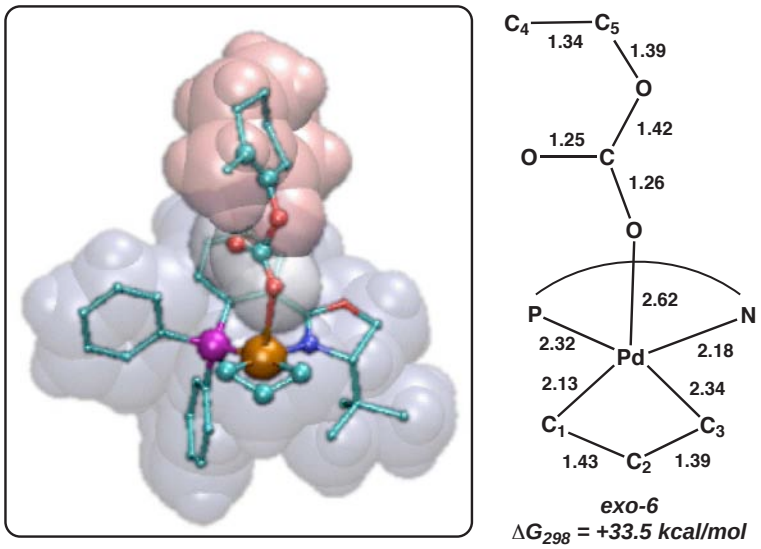

Figure 4.8: Intermediate *exo*-**6**: Coordinated ion pair post oxidative addition

of doing so, the CO_2 can vacate the axial position for the enolate with a barrier of +40.4 kcal/mol. The transition state relating to the process is *exo*-**7**. Although we calculate this barrier to be 1.5 kcal/mol lower in energy with the B3LYP DFT method, *m*PW1PW91 calculations suggest these two barriers are isoenergetic. Since these values are within the margins of our calculated errors, we cannot distinguish which process may be rate determining through calculations alone, but experimental evidence suggests that decarboxylation is rate determining.

Here, we see that C-O bond that was originally tethering the carboxylate ligand to Pd is now fully dissociated (R = 4.07 Å), while a new Pd-O bond is forming (R = 2.90 Å). The C-O bond lengths of the CO_2 group have shrunken slightly to free CO_2 bond lengths, showing it is about to be released. Likewise, the CO_2 group was bound to the enolate with a bond length of 1.33 Å in **4** and lengthened to 1.42 Å in *exo*-**6** is now clearly breaking (R = 2.00 Å).

Post decarboxylation, we find the lowest energy conformation of **3·enolate** occurs when anionic enolate is axially bound to the Pd in **3** forming the five-coordinate species *exo*-**8a** (ΔG_{298} = +26.3 kcal/mol) showing the Pd-O bond binds with an

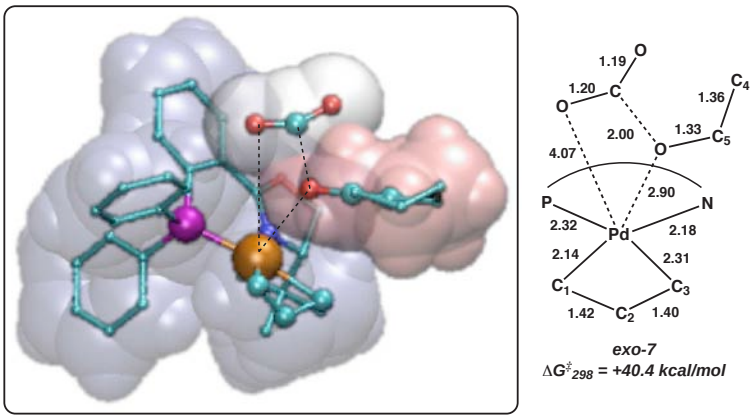

Figure 4.9: Transition state *exo*-**7**: Decarboxylation reaction

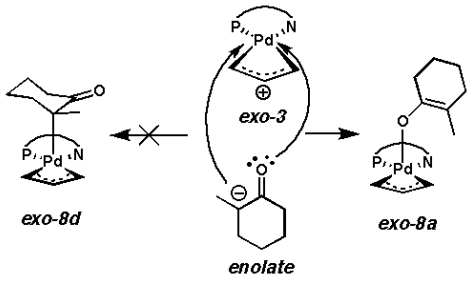

Figure 4.10: C-bound axial enolates (*exo*-**8d**) invariably relaxed to intermediates *exo*-**8a**

energy of 4.6 kcal/mol in THF. Calculations on two other variants of *exo*-**8a**, *exo*-**8b** (ΔG_{298} = +27.0 kcal/mol) and *exo*-**8c** (ΔG_{298} = +27.6 kcal/mol), yielded different orientations of the enolate species that are only slightly higher in energy than *exo*-**8a**, thus making *exo*-**8b** and *exo*-**8c** feasible intermediates as well. *Endo*-**8a** (ΔG_{298} = +30.2 kcal/mol), *endo*-**8b** (ΔG_{298} = +29.3 kcal/mol), and *endo*-**8c** (ΔG_{298} = +30.2 kcal/mol), the related *endo*-analogs were all higher energy intermediates likely due to steric influences at the metal center. Figure 4.11 contains a summary of these relative energies. Attempts at finding another isomeric intermediate, *exo*-**8d**, which has an axially bound carbon invariably failed, and all relaxations of this potential intermediate resulted in a variant of *exo*-**8a** (see Figure 4.10). The axial Pd-O bond distance of *exo*-**8a**, *exo*-**8b**, and *exo*-**8c** is long (R = 2.54–2.69 Å) compared

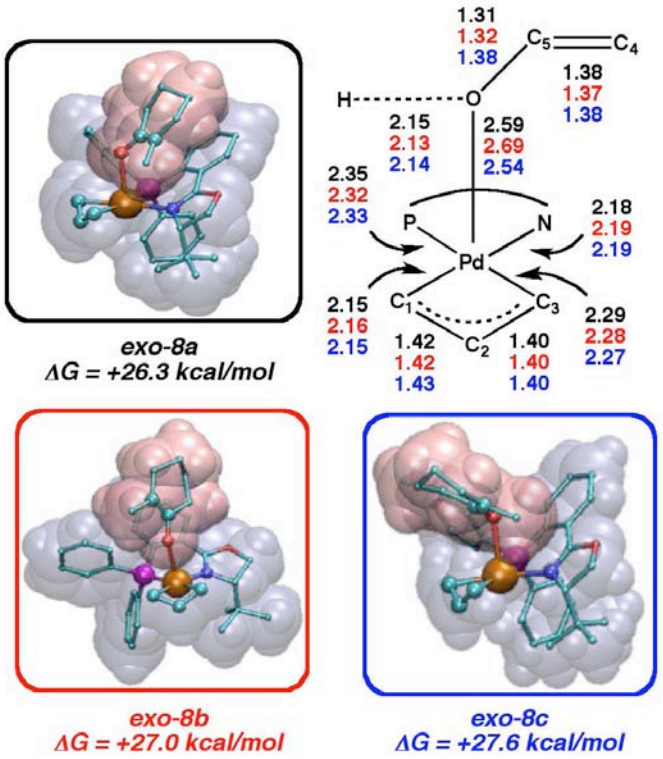

Figure 4.11: Intermediates *exo*-**8(a/b/c)**

to dative bonds involving water ligands and square planar Pd(II) complexes (R = $\sim$ 2.1 Å). The Pd-P bond lengths (R = 2.32–2.35 Å), Pd-N bond lengths (R = 2.18–2.19 Å), and Pd-C_1 bond lengths (R = 2.15–2.16 Å) are comparable to those in **3**. The Pd-C_3 bond lengths are slightly shorter (R = 2.27–2.29 Å) suggesting that the Pd-O bond stabilizes this bond. Favorable electrostatic energy appears to also come from an interaction involving the oxygen on enolate and an *o*-phenyl H from the phenyl-phosphine group (R = 2.13–2.15 Å). The bond angles about the metal center are roughly 90°—(O-Pd-C_1 = 73.5–95.3°), (O-Pd-C_3 = 75.1–92.6°), (O-Pd-P = 87.8–95.7°), (O-Pd-N = 85.1–106.7°)—showing that all three structures can be considered as square pyramidal complexes. All other bond distances are consistent with those shown in Figure 4.5. Lastly, the calculated dipole moments of *exo*-**8a**, *exo*-**8b**, and *exo*-**8c** are 7.4 Db, 11.1 Db, and 8.5 Db, respectively. We interpret these results to mean that *exo*-**8b** will be more stabilized in highly polar solvents due to

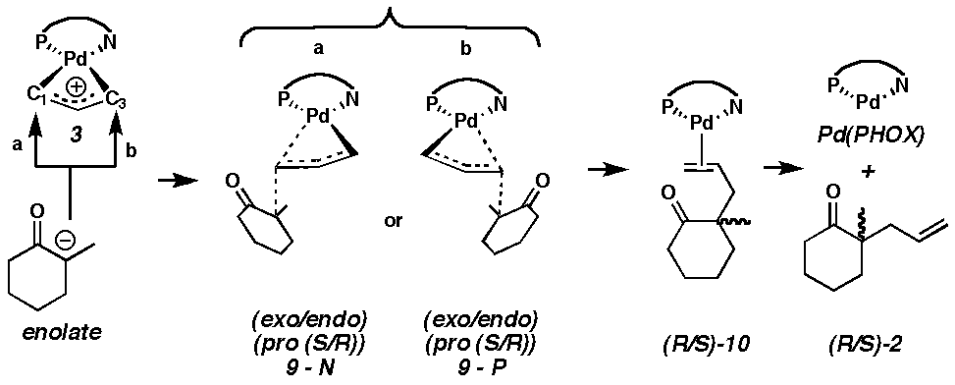

Figure 4.12: External nucleophilic attack pathways

its orientation that permits a larger dipole, however we find that all are very similar in energy after the effects of solvation are taken into account.

4.3.4 Outersphere product formation reactions

As mentioned in the introduction, asymmetric allylation reactions using PHOX ligands are usually regarded as an external nucleophilic attack as in Figure 4.12. Here, enolate can couple to intermediates (*endo*/*exo*)**-3** producing the complexes (*R*/*S*)**-10**, thus forming products (*R*/*S*)**-2** while eschewing direct coupling to the Pd center seen in stable compounds *exo*-**8(a/b/c)**. We see that the allyl-fragment of (*endo*/*exo*)**-3** has two reactive carbons (C_1 or C_3) that may undergo nucleophilic attack. Attack at these carbons would result in one of eight different transition states: (*endo*/*exo*)-**(pro-**(*S*/*R*)**)-5-(N/P))** and each would eventually form products **Pd(PHOX)** and (*R*/*S*)**-2**. We successfully identified 6 of 8 of these transition states and found no significant energy preference between *endo*- and *exo*- confirmations, attacks that occurred at C_1 rather than at C_3, nor attacks that would form *R* products rather than *S* products. (Although we were not able to sufficiently characterize two transition states with only one imaginary frequency, preliminary calculations showed no reason to believe different energies would be expected.) This is not entirely surprising since chemical intuition suggests that in the absence of the protecting groups, symmetric

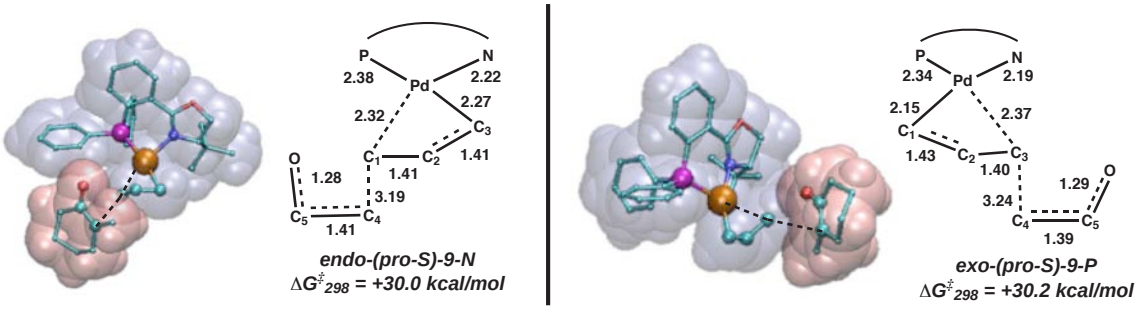

Figure 4.13: Transition states *endo*-**(pro-**S**)-9-N** and *exo*-**(pro-**S**)-9-P**

products would form via external nucleophilic attacks.

We report the structures of the two lowest energy transition states, *endo*-**(pro-**S**)-5-N** and *exo*-**(pro-**S**)-5-P** in Figure 4.13. Both have similar energies and interatomic bond distances. All non-reacting bonds remain essentially constant with respect to those in *exo*-**8a**. The reacting bonds show intermediate bond lengths, and the breaking Pd-C bonds and forming C-C bonds are nearly the same (R = 2.32 Å and 2.37 Å) and (R = 3.19 Å and 3.24 Å), respectively. The calculated dipole moments of the six transition states were all between 11.9–12.7 Db, substantially higher than the dipole moment of *exo*-**8a** and suggesting that these transition states will be more stabilized in more polar solvents. We reiterate, the fact we find a multitude of iso-energetic transition states relating to outer-sphere mechanisms is not surprising since there are no directing groups on the electrophilic allyl fragment. What is intriguing is the fact that experiments show high ee's and high-level calculations affirm the chemically intuitive expectation that external attacks would show no enantioselective preference. Therefore, there is room to improve our understanding of asymmetric allylation mechanisms.

Based on experimental understanding and our trust in these calculation results, we are confident that these external nucleophilic attack pathways are not traversed under enantioselective Tsuji allylation reaction processes. However, the products of these pathways will result in a realistic intermediate that involves the final observed

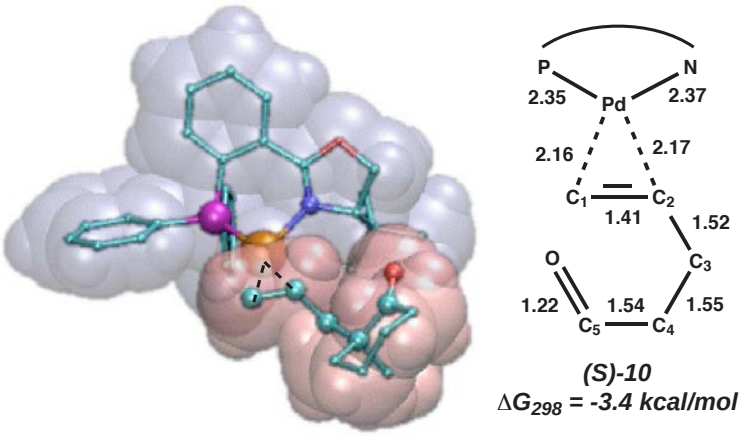

Figure 4.14: Intermediate (*S*)**-10**

product, (*S*)**-2** + **Pd(PHOX)**. Following reductive C-C coupling, a stable intermediate is formed, (*S*)**-10** (Figure 4.14), that is described as (*S*)**-2** coordinated to **Pd(PHOX)** via an η-2 bond from the terminal alkene. This intermediate is the most stable complex identified and is a likely resting state for this catalyst (ΔG_{298} = 3.4 kcal/mol).

The calculated bond distances of (*S*)**-10** shares similar traits as **4** – most noticeably, the Pd-N bond is longer (R = 2.37 Å). Gas phase calculations on Pd(0) complexes typically result in complexes with coordination numbers of 2. Indeed, gas phase calculations on isolated **Pd(PHOX)** show Pd is only bound to the phosphine ligand (R = 2.37 Å) and has no bond to the oxazoline (R = 3.27 Å). However, in the presence of either a polar solvent or a strongly backbonding ligand, i.e., an ethene fragment, electron density can draw away from Pd and result in 3-coordinate trigonal complexes. That Pd prefers to be bound to the phosphine identifies that the Pd-P bond is stronger than the Pd-N. The short C_1-C_2 (R = 1.41 Å) and O-C_5 (R = 1.22 Å) bond distances in (*S*)**-10** are consistent with representative double bond lengths.

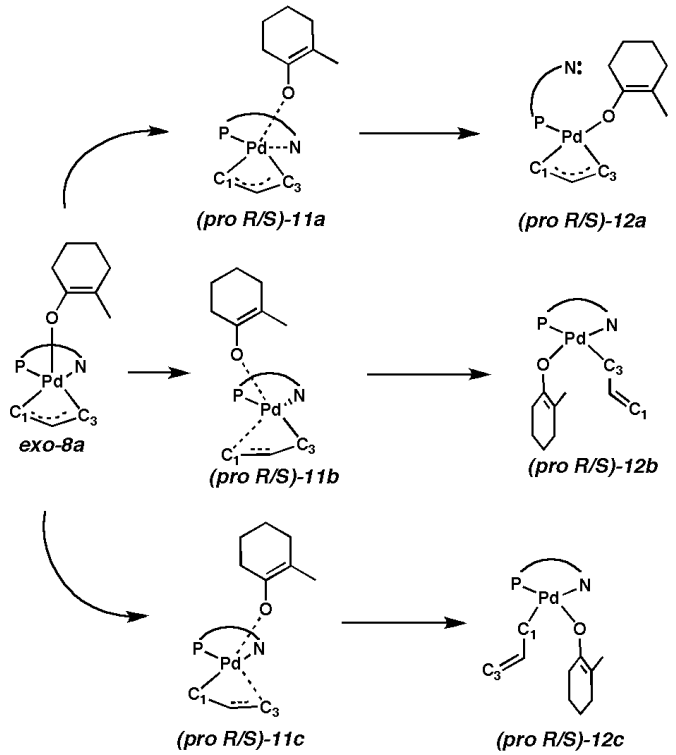

Figure 4.15: Internal rearrangement pathways leading to 4-coordinate complexes

4.3.5 Innersphere rearrangements

To this point, the mystery about the enantioselective Tsuji allylation reaction pathway remained unsolved. To investigate further, we sought pathways that form intermediates where C-C coupling might easily occur. Specifically, we wanted pathways to convert 5-coordinate *exo*-**8a** to 4-coordinate species that are common for d^8 transition metal complexes.

We considered three different rearrangements from square pyramidal *exo*-**8a**, 5-coordinate trigonal bipyramidal **11(a/b/c)**, where each forms different 4-coordinate square-planar complexes, **12(a/b/c)**. We considered (pro-R/S) internal rearrangement pathways in each pathway. See Figure 4.15 for a summary of the investigated internal rearrangement pathways.

Rearrangement exchanging N with O: Two transition states were identified, **(pro-(R/S))-11a**. The calculated energies of these species were +34.4 and +32.3 kcal/mol,

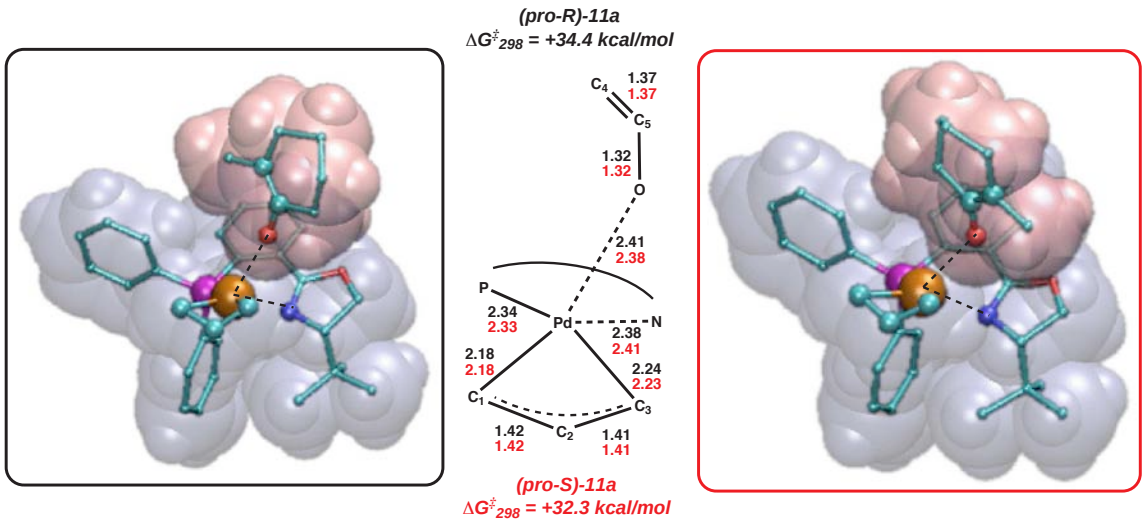

Figure 4.16: Transition states **(pro-(R/S))-11a**

respectively, showing a 2.1 kcal/mol preference towards **(S)-10** formation in this mechanistic step. Although we identify an enantioselective process, it is not likely feasible realistically since non-enantioselective external attack barriers were all under +32.0 kcal/mol.

Relevant bond distances for **(pro-R/S)-11a** are nearly identical (see Figure 4.16), and non-reacting bonds show no significant differences from *exo*-**8a**. In these transition states, the oxazoline bond is breaking (R = 2.38 Å and 2.41 Å, respectively), while the enolate fragment is becoming more tightly bound while moving from an axial position to an equatorial position (R = 2.41 Å and 2.38 Å, respectively). We note that both reacting bond lengths are nearly identical between pro-R and pro-S structures despite the $\sim$ 2 kcal/mol difference. This fact signifies that this energy difference is dominated by electrostatic and vdW interactions rather than bonding orbital overlap with the Pd-center in these transition states. Although the energies of the **(pro-R/S)-11a** transition states limit their likelihood of being crossed, we note that resulting products from these transition states, **(pro-R/S)-12a**, are substantially more stable than *exo*-**8a**, +18.7 and +18.5 kcal/mol, respectively. The interatomic distances of **(pro-R/S)-12a** are very similar (Figure 4.17). In these in-

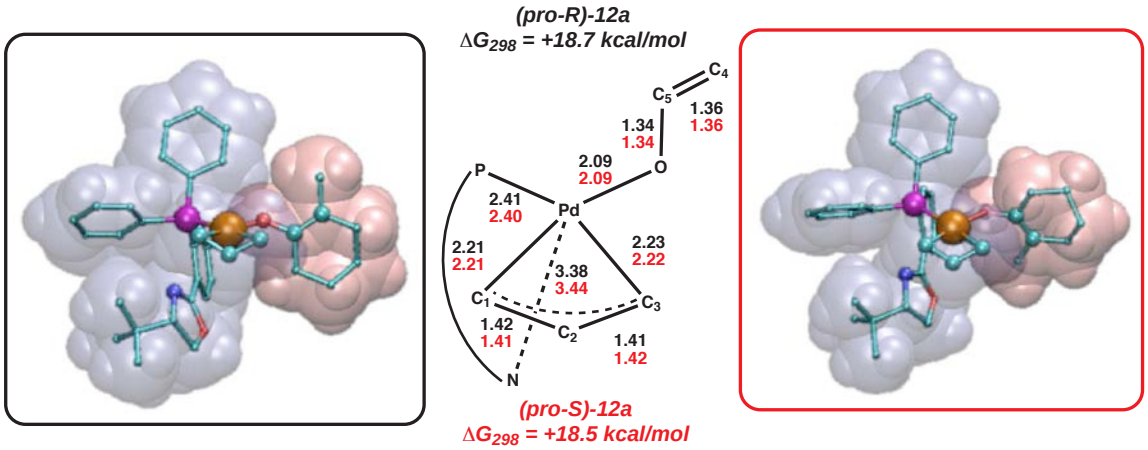

Figure 4.17: Intermediates **(pro-**(R/S)**)-12a**

termediates, the Pd-O bond has shortened substantially to 2.09 Å in both structures while the oxazoline fragment has clearly left the bonding sphere of the Pd center, (R = 3.36 Å and 3.44 Å). We find that axial bonding by the oxazoline was unfavorable, and attempts relaxed back to structures **(pro-**R/S**)-8a**. This is likely the result of poor overlap resulting from both the steric restrictions of the oxazoline ligand associated with the nearby stereocenter and the conjugated PHOX backbone.

In conclusion, we found the energetics of transition states **(pro-**R/S**)-11a** were close to those associated with external attack, however we found no feasible transition states that exited **(pro-**R/S**)-12a** to form products. Thus, we deem internal rearrangements of this kind to be unlikely.

Rearrangement exchanging C_1 with O: Another possible rearrangement involves substituting the Pd-C_1 bond from the allyl fragment with an equatorial Pd-O bond from the enolate fragment. In contrast to the rearrangement described above, this rearrangement is feasible because we substitute the η-3 allyl-fragment and a weakly bonding axial Pd-enolate bond with a stronger equatorial Pd-O bond, an η-1 alkyl bond, and an additional C-C π-bond at the terminus of the allyl fragment.

We find the transition states for these rearrangements, **(pro-**R**)-11b** and **(pro-**S**)-11b**, were even higher than the barriers displacing the oxazoline from the metal

center, +35.5 and +34.5 kcal/mol, respectively. The 1 kcal/mol difference in energies is enough to suggest that passage over these transition states may lead to enantioselective products, however both pathways are substantially higher in energy than external attack pathways, so they are unlikely to contribute significantly.

The geometries of **(pro-*R*/*S*)-11b** are summarized in Figure 4.18. We see no significant differences between the internal coordinates of **(pro-*R*/*S*)-11b**, and non-reacting bonds are similar to previous intermediates. Both reacting bonds, Pd-O (R = $\sim$ 2.32 Å for both isomers) and Pd-C_1 (R = $\sim$ 2.68 Å for both isomers), show intermediate bond lengths compared to those in *exo*-**8a**. The disparity between C_1-C_2 bonds (R = $\sim$ 1.37 Å for both isomers) and C_2-C_3 bonds (R = $\sim$ 1.45 Å for both isomers) show that this transition state involves π-bond formation over the C_1-C_2 bond. The 1.0 kcal/mol energy difference is attributed to steric interactions between the enolate fragment and the catalyst. The smaller ΔG value compared to **(pro-*R*/*S*)-11a** shows that the orientation of the enolate fragment has less severe consequences to relative energies on these transition states.

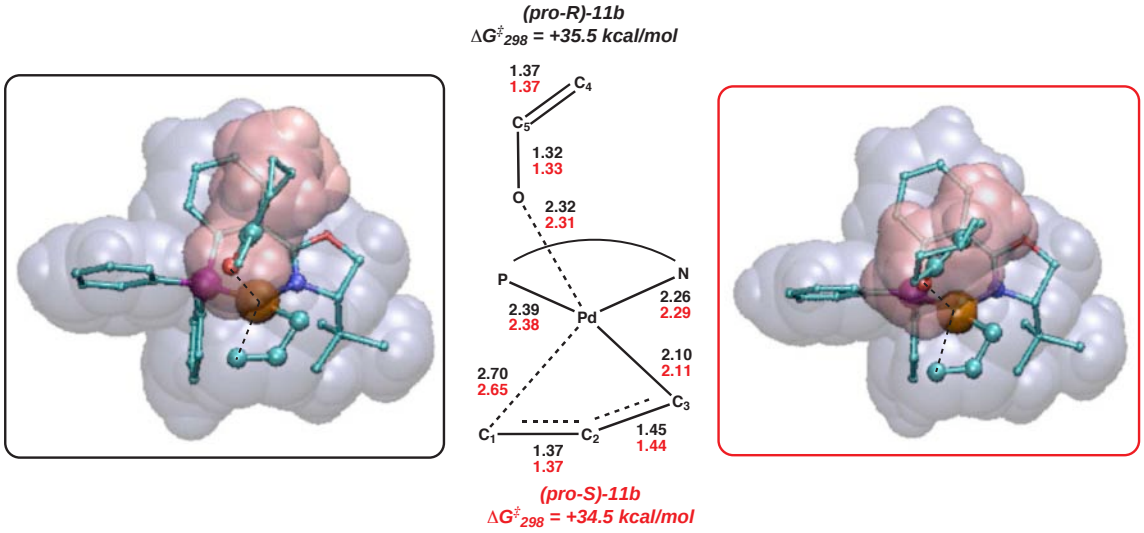

Figure 4.18: Transition states **(pro-*R*/*S*)-11b**

The resulting products of **(pro-*R*/*S*)-11b** are **(pro-*R*/*S*)-12b**. These intermedi-

ates are slightly more stable than *exo*-**8a**, -3.2 and -1.5 kcal/mol, respectively, though not as stable as the intermediates that maintain the allyl fragment in an η-3 bond. Additionally, **(pro-***R*/*S***)-8b** share very similar interatomic distances. Bonds between Pd and the PHOX ligand have lengthened (Pd-P, R = $\sim$ 2.52 Å for both isomers) and shortened (Pd-N, R = $\sim$ 2.16 Å for both isomers) according to the relative trans-influences of ligands directly opposite to those bonds. The Pd-C_3 bond has shortened slightly (R = $\sim$ 2.11 Å for both isomers) on account of slipping from an η-3 bond to an η-1 bond. The C_1-C_2 bonds (R = $\sim$ 1.47 Å for both isomers) and C_2-C_3 bonds (R = $\sim$ 1.35 Å for both isomers) show expected single-bond and double-bond character, respectively. The O-C_5 bonds (R = $\sim$ 1.34 Å for both isomers) and C_4-C_5 bonds (R = $\sim$ 1.36 Å for both isomers) show conjugation of the enol fragment.

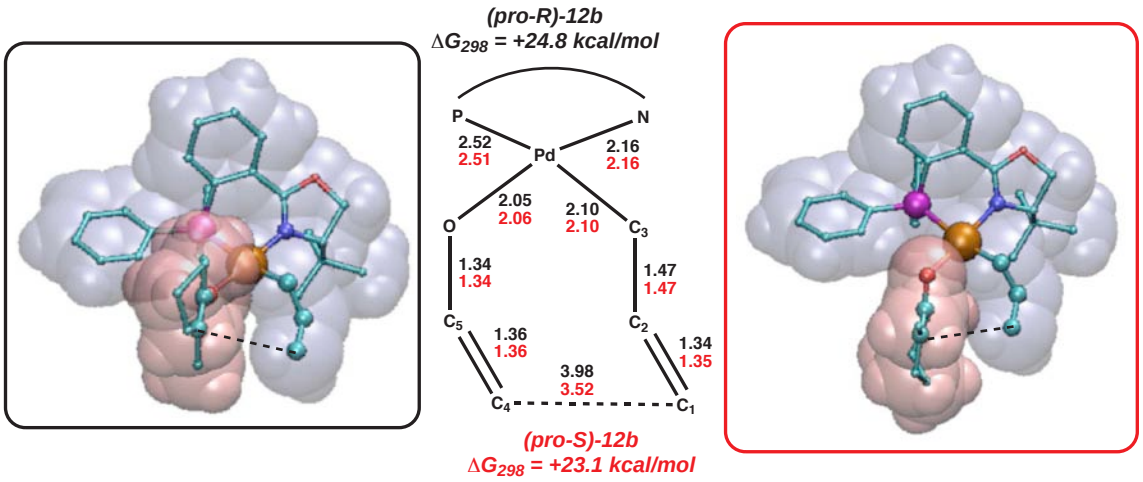

Figure 4.19: Intermediates **(pro-***R*/*S***)-12b**

In conclusion, these barriers are prohibitively high in energy compared to previous external-attack processes, so we considered one more possible rearrangement that would lead to a stable 4-coordinate intermediate.

Rearrangement about O and C_3: The third internal rearrangement pathway we present was originally regarded as the most feasible since it involved substituting the metal-

ligand bond opposite the more *trans*-influencing P atom. This rearrangement process involves replacing the η-3 allyl fragment and the weak axial Pd-enolate bond with an η-1 Pd-C_1 bond trans to the oxazoline ligand and a stronger equatorial Pd-enolate bond occupying site that was occupied by C_3. Note that this complex has the strongest *trans*-influencing ligands opposite the two weakest trans-influencing ligands.

Two transition states are possible for this process, **(pro-*R*)-11c** and **(pro-*S*)-11c**, and both were found be lower in energy than any previous barriers (+29.1 and +28.1 kcal/mol, respectively). This pathway is deemed the most likely pathway of those shown in Figure 4.15 and also preferred over external attack pathways as it shows qualitative enantioselectivity for observed products **(*S*)-2**.

A Boltzmann distribution of this 1.0 kcal/mol difference correlates to an expected ee of ~ 70. Experimentally, we see this substrate yields ee's in the low 90s, signifying an energy difference in the enantiodetermining step of 1.7 kcal/mol. This value is well within the margin of error in our calculations, but we also note that control calculations with the *m*PW1PW91 functional, a hybrid DFT method considered better suited for vdW interactions, find a promising energy difference of 1.6 kcal/mol.

Figure 4.20 contains relevant internal coordinates of transition states **(pro-*R*/*S*)-11c**. Unlike in previous transition states, there is one interatomic distance, the Pd-C_3 bond length, that is substantially different between the two structures: R = 2.61 Å in **(pro-*R*)-11c** and R = 2.37 Å in **(pro-*S*)-11c**. Since this bond is breaking in a state more resembling the reacting intermediate, *exo*-**8a**, **(pro-*S*)-11c** is an earlier transition state than **(pro-*R*)-11c**. Through a similar comparison, we find both **(pro-*R*/*S*)-11c** are earlier than the trans-N analogs of these transition states, **(pro-*R*/*S*)-11b**.

Structures of the resulting products of these transition states, **(pro-*R*/*S*)-12c**, are

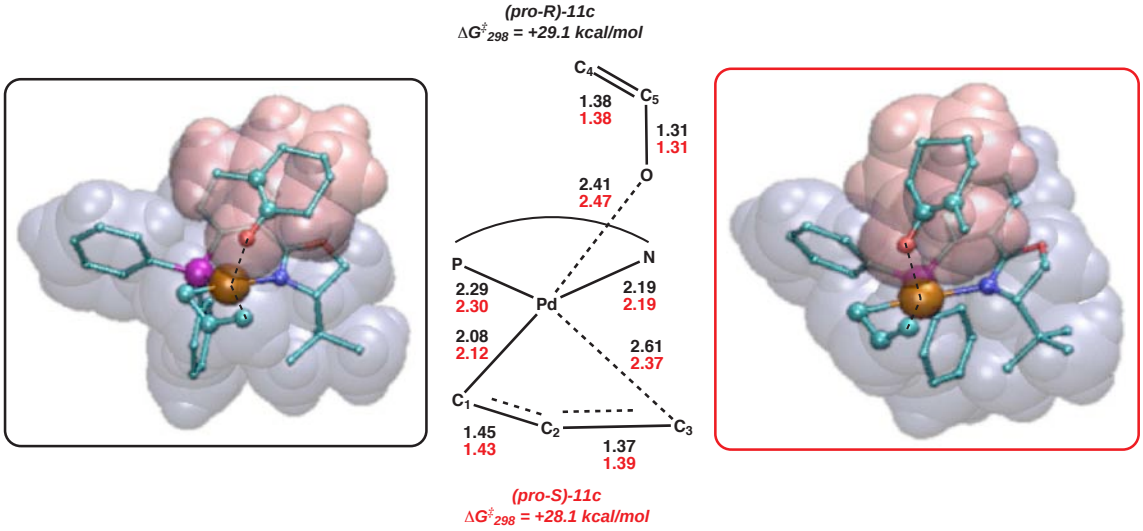

Figure 4.20: Transition states **(pro-R/S)-11c**

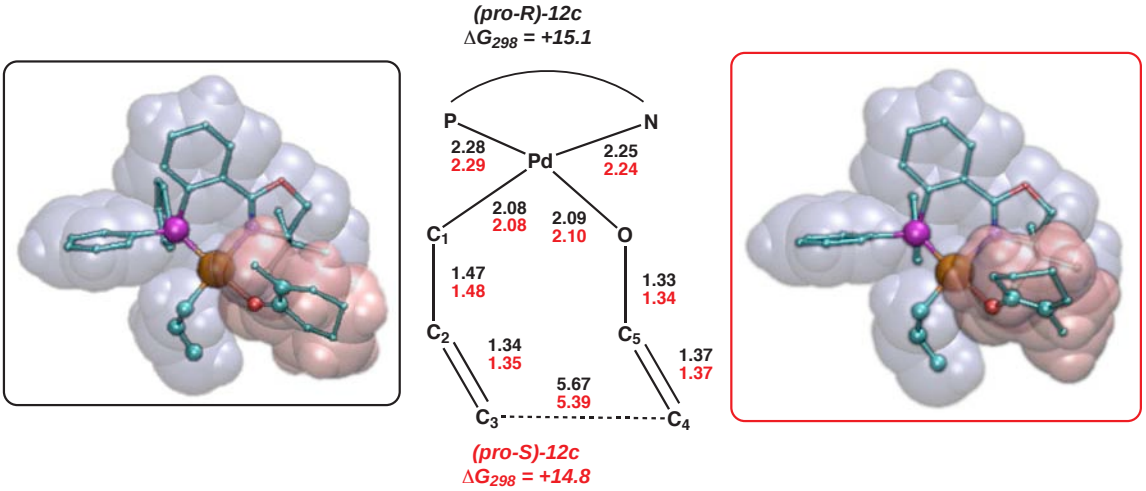

Figure 4.21: Intermediates **(pro-R/S)-12c**

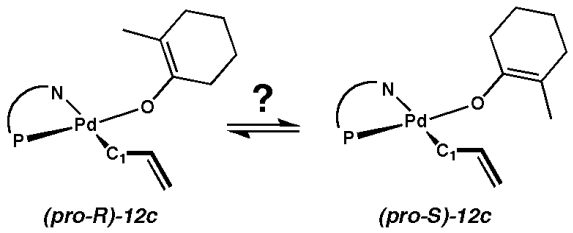

Figure 4.22: Isomerization of intermediate **(pro-R)-12c**

summarized in Figure 4.21. These 4-coordinate species are 11.2 and 12.5 kcal/mol more exothermic with respect to *exo*-**8a**. The interatomic distances of **(pro-R/S)-12c** closely resemble those of **(pro-R/S)-12b** with the exception of bonds involving Pd. Indeed, the Pd-P bond (R = $\sim$ 2.29 Å in both isomers) and the Pd-N bond (R = $\sim$ 2.25 Å in both isomers) more closely resemble the bond distances in the reactant *exo*-**8a**. The Pd-C_1 bond (R = $\sim$ 2.08 Å in both isomers) and the Pd-O bond (R = $\sim$ 2.10 Å in both isomers) are equivalent to those in **(pro-R/S)-12b**.

A multitude of geometric isomers were found that closely resemble both of these structures in terms of interatomic distances, the orientations of the allyl and enol fragments, and their free energies. A 2-dimensional scan across the C_1-Pd-O-C_5 and Pd-O-C_5-C_4 torsion angles found that these intermediates speckle a flat potential energy surface that contains one noticeable barrier. This barrier is associated with the conversion between **(pro-R)-12c** and **(pro-S)-12c**, (Figure 4.22). While we could not identify a transition state whose frequencies yielded with one imaginary normal mode, our best estimates on this barrier are between +6–7 kcal/mol with respect to **(pro-S)-12c** and +20–21 kcal/mol overall.

In conclusion, we find this pathway to be the best at matching observations of products in addition being the lowest-energy pathway leading to products. However, we find a modest barrier for interconversion between two intermediates whose implication is to wash out by the racemizing intermediates **(pro-R/S)-12c**. Thus, for our results to thoroughly depict the enantioselectivity of this reaction, we must find

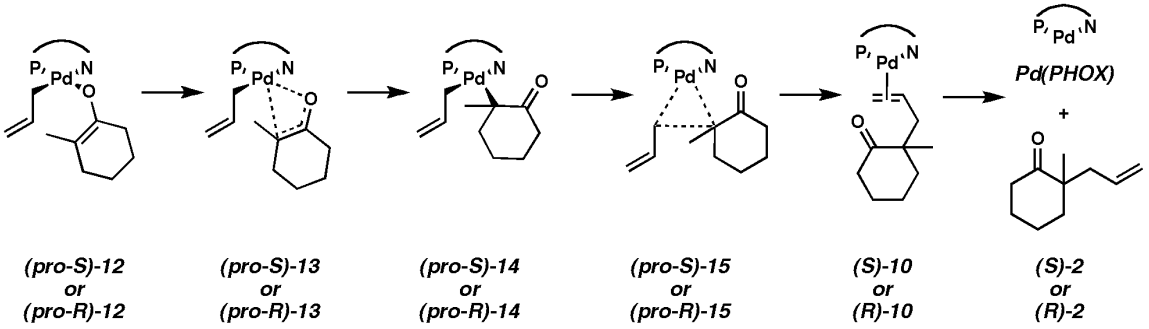

Figure 4.23: Pathways for traditional C-C coupling

a pathway for C-C coupling where products are formed with barriers lower than this interconversion barrier. We proceed with our investigation of C-C coupling reactions.

4.3.6 C-C coupling reactions

A critical question about this reaction process is how the C-C bonds are formed. Previously mentioned studies reported evidence for external nucleophilic attacks whose enantio-determining barriers are presumably the C-C coupling barriers. In these inner-sphere processes, however, we find evidence that at least some of the enantioselectivity may be determined from through conversion of *exo*-**8a** to **(pro-**S**)-12c** via **(pro-**S**)-11c**. Since other reports of inner-sphere allylic alkylation involved processes with traditional modes of reductive elimination, we investigated the pathways presented in Figure 4.23.

In order to form a Pd complex with two Pd-C bonds as required in traditional reductive elimination, a pathway must be found to convert the Pd-O bond in **(pro-**R/S**)-12c** to a Pd-C_4 bond in **(pro-**R/S**)-14**. We found one of two transition states that could provide this interconversion, **(pro-**R**)-13** (Figure 4.24), and we find this barrier higher in energy than external attack barriers (+36.9 kcal/mol), and thus unfeasible to account for observed products.[1]

[1]Although we only find a barrier for the R-forming process, preliminary calculations on the S-forming process suggest its energy will be even higher as the cyclohexyl ring on the enolate must

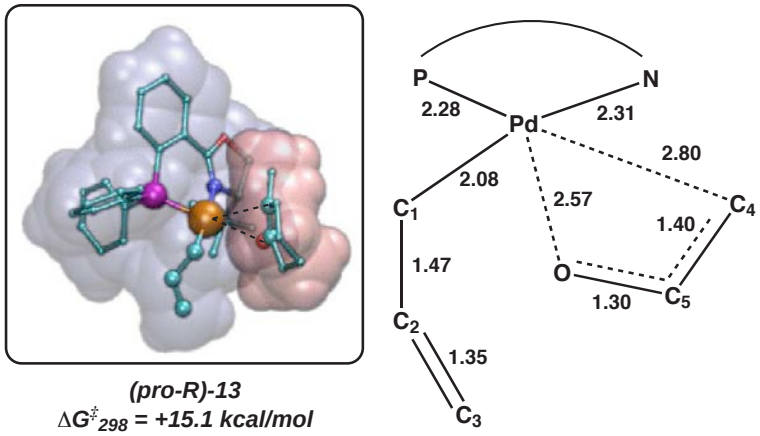

Figure 4.24: Transition state **(pro-*R*)-13**

The structure of **(pro-*R*)-13** displays several descriptive characteristics. As expected, the reacting Pd-O bond (R = 2.57 Å) and the Pd-C_4 bond (R = 2.80 Å) are both substantially longer than their optimal distances, showing significant steric strain in bringing the enolate close to the metal. We also expected to see the O-C_5 bond (R = 1.30 Å) and the C_4-C_5 bond (R = 1.40 Å) are now dissimilar to account for the formation of an sp^3 C_4 and an O-C_5 double bond. Additionally, the C_1-C_2 and C_2-C_3 bonds remain unchanged from **(pro-*R*)-12c**, while the bonds involving the Pd are slightly longer to accommodate for the steric bulk of the enolate rearranging. As noted earlier, if **(pro-*S*)-13** indeed exists, it likely has an even higher barrier as the steric interactions of the enolate ligand are even more unfavorable than in **(pro-*R*)-13**.

The resulting products of these transition states are intermediates **(pro-*R*/*S*)-14** (Figure 4.25), both of which are the higher in energy than all previously calculated intermediates (+28.2 and +26.0 kcal/mol, respectively). Like transition state **(pro-*R*)-13**, these intermediates show substantial steric crowding. We note that the trans-influence of C_4 on P (Pd-P bond: R = $\sim$ 2.45 Å for both isomers) is less than it was in the case of C_1 on P in **(pro-*R*/*S*)-12b** (where Pd-P bond: R = $\sim$ 2.50 Å).

point directly into the allyl-fragment in order to transition from **(pro-*S*)-12c**.

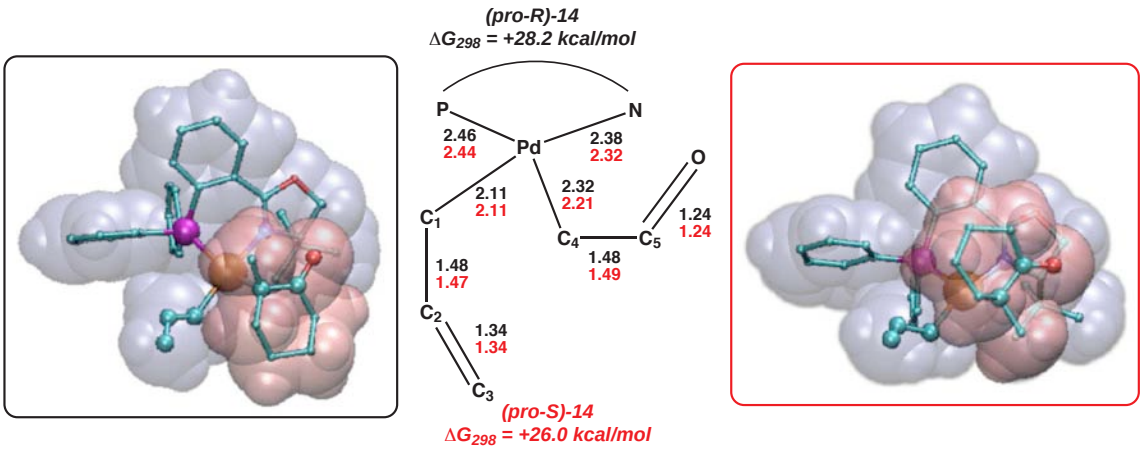

Figure 4.25: Intermediates **(pro-R/S)-14**

Additionally, the *trans*-influence of C_1 on N appears to be substantially large, (Pd-N bond: R = $\sim$ 2.35 Å for both isomers), but this is even longer than the Pd-N bond length in **(pro-R/S)-12c** (R = $\sim$ 2.25 Å), thus showing this bond lengthening is mainly due to steric crowding of the enolate. As expected, the C_2-C_3 bonds (R = 1.34 Å for both isomers) and O-C_5 bonds (R = 1.24 Å for both isomers) relate to double bonds while the C_1-C_2 bonds (R = $\sim$ 1.48 Å for both isomers) and C_4-C_5 bonds (R = $\sim$ 1.49 Å for both isomers) relate to single bonds.

The relatively high energies and clearly unfavorable steric interactions strongly suggested that traditional reductive elimination was not a preferred process. However, we still identified barriers, **(pro-R/S)-15**, for completeness and found these processes to be extremely high in energy: +68.3 and +64.4 kcal/mol, respectively (Figure 4.26).

These transition states exhibit very unfavorable structures as an explanation for their high energies. The most striking structural feature in **(pro-R/S)-15** is the fully broken Pd-N bond (R = $\sim$ 3.38 Å for both isomers). Recall that in the external attacks we identified slight lengthening of the Pd-N bond as the Pd(II) was reduced to Pd(0). In these transition states, all stabilizing contributions of the Pd-N bond are effectively trumped by the high steric strain in both maintaining intermediate distances for the Pd-C_4 bond (R = $\sim$ 2.41 Å in both isomers) and also the Pd-C_1

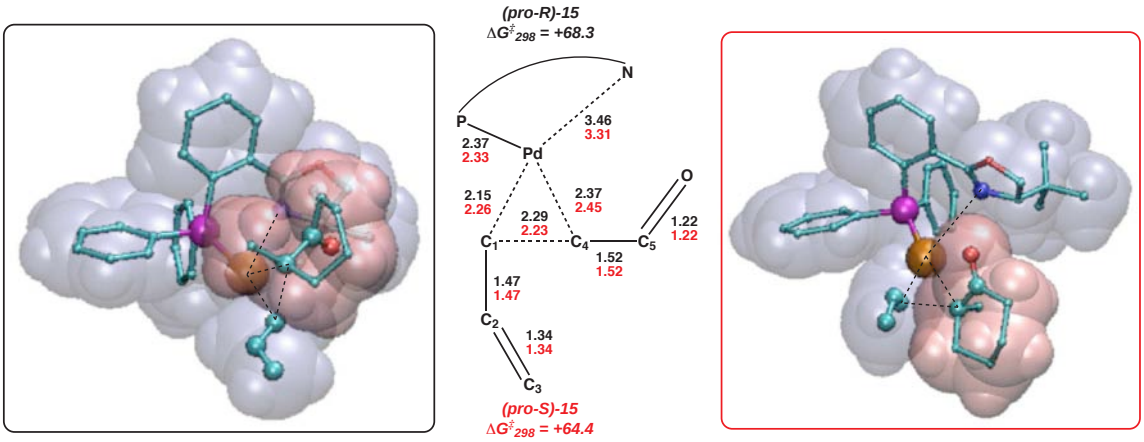

Figure 4.26: Transition states **(pro-R/S)-15**

bond (R = $\sim$ 2.21 Å in both isomers). The C_1-C_4 bond is forming with a large intermediate distance (R = $\sim$ 2.26 Å in both isomers). Interestingly, the Pd-P bond distance (R = $\sim$ 2.35 Å) decreases slightly from its values in **(pro-R/S)-14** (R = $\sim$ 2.45 Å), giving this bond the distinction of being the only bond capable of relaxing to a preferred equilibrium distance in these transition states.

In conclusion, we are confident that this reaction does not proceed via the traditional form of reductive elimination that previously described C-C coupling reactions likely follow. The distinction between these transition states and those associated with favorable 3-membered reduction elimination processes are the atoms that are directly bound to the Pd. It was previously found that reductive eliminations from two sp^3 carbons was highly unfavorable for Pd(II) complexes[115, 116]. The rational for this was that substantial orbital overlap was required to permit reductive eliminations and the directional character of two sp^3 orbitals prevented this from being feasible for Pd(II) complexes. However, reactions involving traditional C-C coupling all involved at least one sp^2 or sp^1 carbon, both of which contain substantially more s character in their hybrid orbitals, permitting enough overlap to make these processes allowed.

Since the traditional reductive elimination clearly cannot explain observed prod-

ucts, another reductive process must be involved. Starting from intermediates **(pro-R/S)-12c**, we found a pathway for a novel process that involves reductive C-C coupling from the 3 and 3' positions of the allyl and enol fragments forming transition states **(pro-R/S)-16**. This reductive pericyclic rearrangement has precedent as an all-carbon analog in theoretical studies by Echavarren and coworkers[117], and has recently been used in explaining several applied mechanisms[118, 119, 120, 121, 122]. Whereas the previously presented mechanism was a hybrid of the Cope rearrangement along with a cheletropic rearrangement[123], this process is a hybrid of a Claisen and reductive cheletropic rearrangement (Figure 4.27).[2]

Transition states undergoing this form of reductive elimination are distinguished according to the boat-like or chair-like orientation made by the allyl and enol fragments during C-C coupling. Considering both *S*- and *R*- products, we considered a total of four transition states: **(boat/chair)-(pro-(R/S))-16**.

The lowest energy *R*- and *S*- forming transition states found were those involving chair-like orientations, consistent with the results of Echavarran. The barriers for these transition states: **chair-(pro-S)-16** = +26.1 kcal/mol, **chair-(pro-R)-16** = +26.0, **boat-(pro-R)-16** = +27.0 kcal/mol, and **boat-(pro-S)-16** = +28.3 kcal/mol. Since these two energies are essentially equivalent, we predict that enantioselectivity will not be affected by passage over these barriers. The two lowest barriers are presented in Figure 4.28.

Similar processes using **(pro-(S/R))-12b** as reactants were found to be much higher in energy (by $\sim$ 34 kcal/mol). Although these barriers are too high to be considered feasible, we do note that we find mild enantioselective preference towards forming **(S)-2** products with these reactions while we find no enantioselective preference in **chair-(pro-(R/S))-16**.

[2]Interestingly, the Cope rearrangement has also been found in the tandem Wolff-Cope form[124, 125].

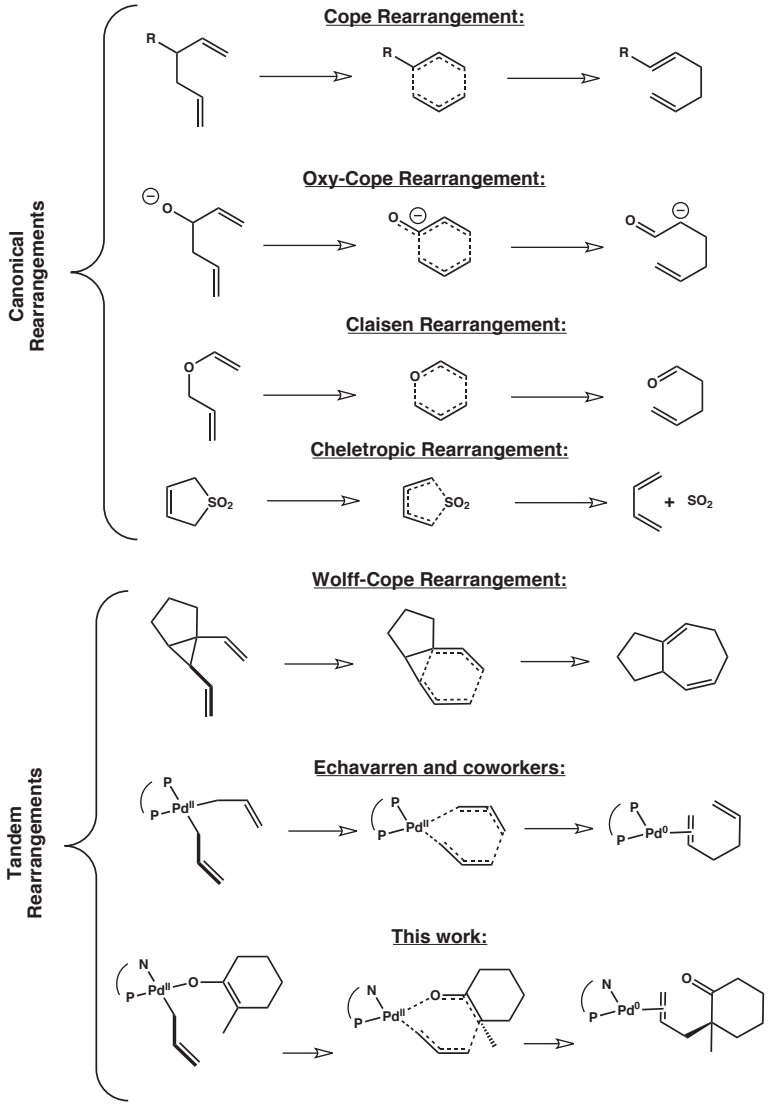

Figure 4.27: Canonical and tandem pericyclic reactions

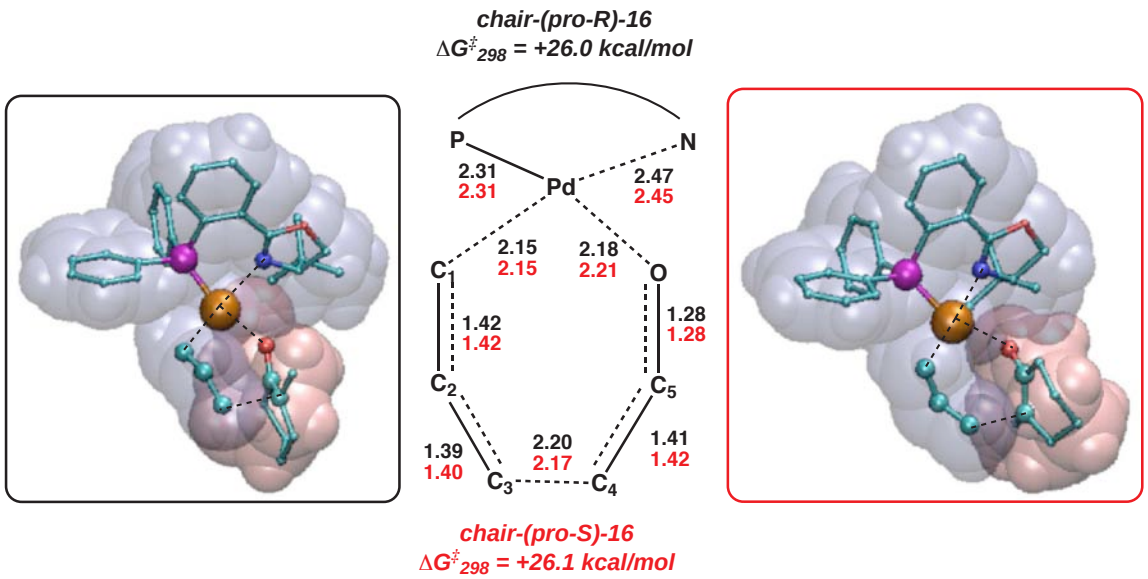

Figure 4.28: Transition states **chair-(pro-R/S)-16**

The interatomic distances (see Figure 4.28) of these transition states show large conjugation across a 7-member system of Pd, C_1-C_5, and O. The C_3-C_4 bond distance is substantially smaller (R = $\sim$ 2.19 Å for both isomers) than its values in intermediates **(pro-(S/R))-12c**, (R > 5.0 Å in both isomers). The Pd-N bond is long, (R = 2.46 Å for both isomers), showing that it is breaking while Pd(II) is reduced to Pd(0).

The lack of an enantioselective product forming pathway from **pro-(S)-12c** is surprising, as we had found an approximate barrier for interconversion between **pro-(S)-12c** and **pro-(R)-12c** to be only +20.8 kcal/mol while this reductive pericyclic rearrangement is +26.1 kcal/mol. Control calculations with other DFT methods found nearly equivalent energy separations with the exception of the M05 functional, which found the two barriers isoenergetic in solvent. Numerous attempts at finding other pathways, including a concerted conversion from *exo*-**8a** to S-**10**, were all found to be too high in energy.

While a relatively facile barrier for interconversion is found, a facile barrier would conflict with experimental observations that products form with relatively good enan-

tioselectivities. We acknowledge that our simulations have errors of $\sim$ 2 kcal/mol, however, the fact that three different flavors of hybrid DFT all find no noticeable energetic difference between **chair-(pro-S)-16** and **chair-(pro-R)-16** make us believe that this reductive pericyclic rearrangement is not an enantiodetermining process. Since it is not, the immediately reacting intermediates must not be capable of racemizing in order to be consistent with experiment, i.e., via the internal rearrangement associated with **(pro-S)-8c**.

4.4 Conclusions

Based on our computational results, we propose an illustrative model to describe the unique performance of the enantioselective Tsuji allylation reaction. A complete pathway explaining the unique performance of the enantioselective Tsuji allylation reaction is presented in Figure 4.29. In order for this reaction to perform well, it is crucial that the substrate undergoing allylation is a hard ketone nucleophile. The ketone oxo-group is capable of forming the 5-coordinate intermediate, *exo*-**8a**.

We believe a competition between R- forming and S- forming products then ensues, and its preference is guided by the topology of the PHOX catalyst. An illustration of this topology is shown in Figure 4.30. The faces of intermediate *exo*-**3** are used to visualize the space enolate may use to form transition states **(pro-(R/S))-8c**. Projecting these faces of *exo*-**3** onto a 3x3 cube, we can readily strike out regions of where enolate may and may not bind. With these regions in mind, one can readily determine how to make **(pro-S)-8c** even more preferred than **(pro-R)-8c**. We see the methyl group of enolate interacts more with a proximal phenyl group in **(pro-R)-8c** than in **(pro-S)-8c**. A straightforward synthetic solution is to make subtle substitutions at the ortho-positions of the phenyl groups on the phosphine ligand to further obstruct the **(pro-R)-8c** transition state while leaving **(pro-S)-8c** unaffected.

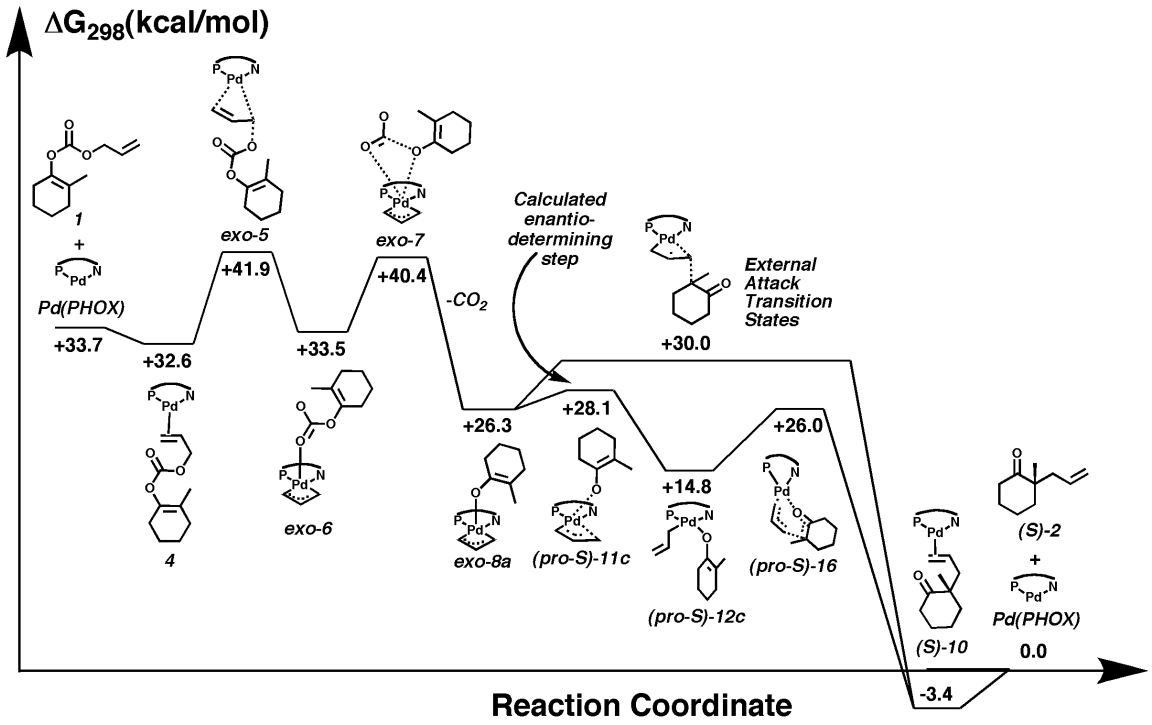

Figure 4.29: The enantioselective Tsuji allylation mechanism with allyl enol carbonates and PHOX ligands

Too large of a substitution runs the risk of interfering too much with the stability of *exo*-**8a**, and thus completely shutting both inner-sphere pathways, leaving only outer-sphere pathways possible. We believe this is why traditional stereochemical probes have failed as the steric bulk of the substituted allyl fragment likely prevents intermediate *exo*-**8a** from forming. Investigations are underway to determine ways to further improve the performance of these catalysts.

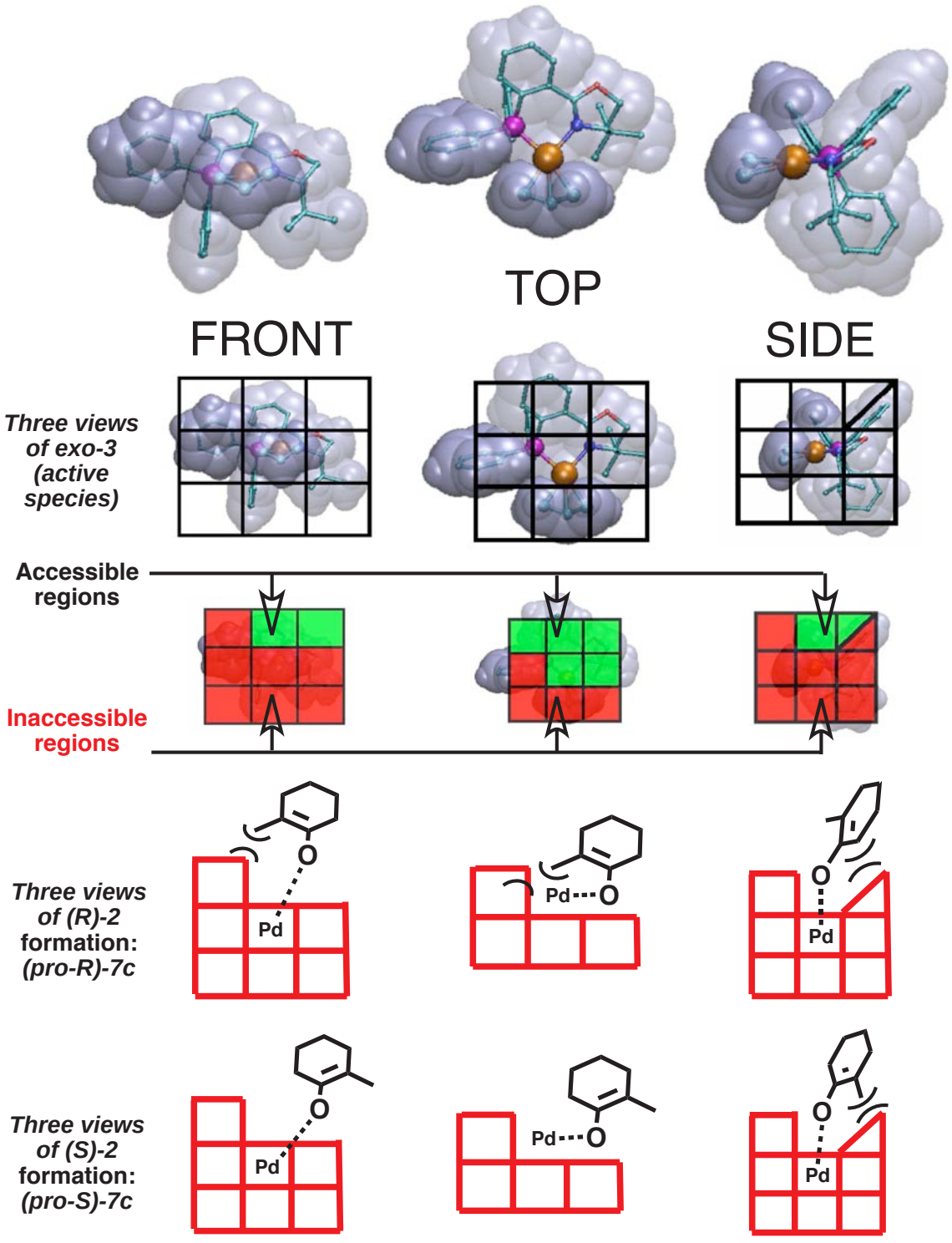

Figure 4.30: Schematic to identify topology of PHOX catalysts. Three views of intermediate **3** are presented. Digitization into a 3x3 grid on each face provides a simple representation for regions where a substrate can bind. Our hypothesis is that R-products are more disfavored than S products due to steric hindrances at the transition states for internal rearrangment, **(pro-R/S)-8c**. Design of more efficient catalysts could exploit unfavorable interactions in **(pro-R)-8c** while having little impact on **(pro-S)-8c**.

Chapter 5

Conclusions

This thesis presented an overview of some of the capabilities quantum chemical calculations have in the field of organopalladium catalysis.

After a brief presentation of computational techniques in Chapter 1, it was shown in Chapter 2 that through careful attention to relevant free energy contributions, various DFT methods can achieve chemical accuracy for relative thermodynamics and respectable accuracies for barrier heights of complicated transition metal reactions including implicit solvation. It was also presented that these same calculations have grave problems in calculating relative free energies of deprotonation reactions. However, it was also shown that these errors could possibly be treated with an empirical correction determined from a test set of molecules similar to those whose information is desired. Before a solution can be made so that simulations methodology can improve, much more work needs to be done to investigate the magnitude of these problems. Unfortunately, little experimental data is available for these types of reactions. Additional contributions from the experimental community of simple and mundane thermochemical data would be greatly appreciated by developers of new and improved QM models for organometallic and inorganic chemistry simulation. With larger test sets the true values of computational methods would be realized.

Chapter 3 addressed the current understanding of the Wacker process. Modern computational techniques have developed a new understanding of the complicated

mechanisms and the seemingly contradictory theoretical and experimental observations. The best correspondence between theory and experiment suggests that internal nucleophilic attack by hydroxide is *not* rate determining under standard industrial conditions, but an internal isomerization reaction would be. This pathway would become prohibitive under increased $[Cl^-]$, but an outer-sphere nucleophilic attack pathway becomes accessible in the presence of $CuCl_2$. For this to be the case, the rate law for the creation of *products* would have a rate law:

$$\text{Rate} = \frac{k[PdCl_4^{2-}][\text{olefin}]}{[H^+][Cl^-]^2}$$

under low $[Cl^-]$ and low $[CuCl_2]$, but

$$\text{Rate} = \frac{k_{acetaldehyde}[PdCl_4^{2-}][\text{olefin}][CuCl_2]}{[Cl^-]} + \frac{k_{chlorohydrin}[PdCl_4^{2-}][\text{olefin}][CuCl_2]}{[Cl^-]}$$

under high $[Cl^-]$ and high $[CuCl_2]$. It is of great interest to see if these models can predict the role of $CuCl_2$ as both the reprocessing catalyst for Pd(0) and in the mechanism of chlorohydrin formation.

Chapter 4 addressed the current understanding of the enantioselective Tsuji allylation reaction. This reaction has been shown to perform asymmetric allylations with high yields and high ee's under a large range of different substrates and solvents. Surprisingly, a mechanistic model for how this process occurs is in dramatic conflict with other asymmetric allylations that require prochiral electrophiles in order to yield enantiomeric products. Simulations show that this pathway indeed proceeds via an inner-sphere mechanism, and simulations also provide arguments for the identity of the rate-determining step (decarboxylation) and enantiodetermining steps (internal rearrangment from a 5-coordinate to a 4-coordinate Pd complex). More simulations on reacting substrates will provide more concreteness in this mechanism, and will possibly lead to improved catalysts. Key to this mechanism is tandem pericyclic re-

arrangement that appears to have characteristics of both reductive cheletropic and Claisen rearrangements. That mechanisms such as this are facile provides more ways for creative methodologies for C-C bond formations.

As evidenced by this work, modern computational simulation techniques have made great strides in improvements to make hard problems easier and impossible problems worth considering. In less than a decade, implicit solvation models have improved to the degree that it is possible to obtain chemically accurate results that would serve as useful tools in understanding homogeneous reaction mechanisms. Naturally, there is still room for improvements in methodology. Even though sometimes tantalizingly desirable, simulation results are not yet at a point of making predictions one can comfortably rely on being true. We are close, however.

Bibliography

[1] C. J. Cramer. *Essentials of Computational Chemistry.* John Wiley & Sons, Inc., Hoboken, NJ, 2nd edition, 2004.

[2] I.N. Levine. *Quantum Chemistry.* Prentice Hall, Upper Saddle River, NJ, 5th edition, 2000.

[3] A. Szabo and N.S. Ostlund. *Modern Quantum Chemistry: Introduction to Advanced Electronic Structure Theory.* Dover, Mineola, NY, 1996.

[4] Jaguar, version 7.0. *Schrödinger, LLC*, 2007.

[5] K. Andersson, P.-Å. Malmqvist, and B.O. Roos. *J. Chem. Phys.*, 100:1218–1226, 1992.

[6] P. J. Stephens, F.J. Devlin, C.F. Chabalowski, and M. J. Frisch. *J. Phys. Chem.*, 98:11623–11627, 1994.

[7] A. D. Becke. *J. Chem. Phys.*, 98:5648–5652, 1993.

[8] A.D. Becke. *Phys. Rev. A*, 38:3098–3100, 1988.

[9] S.H. Vosko, L. Wilk, and M. Nusair. *Can. J. Phys.*, 58:1200–1211, 1980.

[10] C. T. Lee, W. T. Yang, and R. G. Parr. *Phys. Rev. B*, 37:785–789, 1988.

[11] J.P. Perdew, K. Burke, and M. Ernzerhof. *Phys. Rev. Lett.*, 77:3865–3868, 1996.

[12] J.P. Perdew, K. Burke, and M. Ernzerhof. *Phys. Rev. Lett. (Erratum)*, 78:1396, 1997.

[13] C. Adamo and V. Barone. *J. Chem. Phys.*, 108:664–675, 1998.

[14] D. J. Tannor, B. Marten, R. Murphy, R. A. Friesner, D. Sitkoff, A. Nicholls, M. Ringnalda, W. A. Goddard, and B. Honig. *J. Am. Chem. Soc.*, 116:11875–11882, 1994.

[15] B. Marten, K. Kim, C. Cortis, R. A. Friesner, R. B. Murphy, M. N. Ringnalda, D. Sitkoff, and B. Honig. *J. Phys. Chem.*, 100:11775–11788, 1996.

[16] R. E. Easton, D. J. Giesen, A. Welch, C. J. Cramer, and D. G. Truhlar. *Theo. Chim. Acta*, 93:281–301, 1996.

[17] M.W. Palascak and G.C. Shields. *J. Phys. Chem. A*, 108:3692–3694, 2004.

[18] D.M. Camaioni and C.A. Schwerdtfeger. *J. Phys. Chem. A*, 109:10795–10797, 2005.

[19] J.P. Perdew. *Phys. Rev. B*, 33:8822–8824, 1986.

[20] H.L. Schmider and A.D. Becke. *J. Chem. Phys.*, 109:8188–8199, 1998.

[21] H.L. Schmider and A.D. Becke. *J. Chem. Phys.*, 109:9624–9631, 1998.

[22] Y. Zhao and D. G. Truhlar. *J. Chem. Phys.*, 125:194101–194119, 2006.

[23] Jaguar, version 6.5. *Schrödinger, LLC*, 2005.

[24] J.S. Coe. In *MTP International review of science. Inorganic chemistry*, pages 45–62. 1974.

[25] D.D. Wagman, W.H. Evans, V.B. Parker, R.H. Schumm, I. Halow, S.M. Bailey, K.L. Churney, and R.L. Nuttall. The NBS tables of chemical thermodynamic properties. *J. Phys. Chem. Ref. Data*, 11, Suppl. 2, 1982.

[26] M.W. Chase. NIST-JANAF thermochemical tables. *J. Phys. Chem. Reference Data*, (Monograph 9):1–1951, 1998.

[27] M.D. Tissandier, K.A. Cowen, W.Y. Feng, E. Gundlach, E. Cohen, M.H. Earhart, J.V. Coe, and T.R. Tuttle. *J. Phys. Chem. A*, 102:7787, 1998.

[28] L.I. Elding. *Inorg. Chim. Acta*, 6:683–688, 1972.

[29] R.G. Pearson and M.J. Hynes. *K. Tek. Hoegsk. Handl.*, 248-296:459–469, 1972.

[30] L.I. Elding. *Acta Chem. Scand.*, 24:1527–1540, 1970.

[31] G.W. Parshall and S.D. Ittel. *Homogeneous Catalysis: The Applications and Chemistry of Catalysis by Soluble Transition Metal Complexes.* Wiley-Interscience, New York, NY, 1992.

[32] G.O. Spessard and G.L. Miessler. *Organometallic Chemistry.* Prentice Hall, Upper Saddle River, NJ, 1997.

[33] R.M. Trend, Y.K. Ramtohul, and B. M. Stoltz. *J. Am. Chem. Soc.*, 127:17778–17788, 2005.

[34] C.N. Cornell and M.S. Sigman. *Org. Lett.*, 8:4117–4120, 2006.

[35] J. M. Lee, D. S. Ahn, D. Y. Jung, J. Lee, Y. Do, S. K. Kim, and S. K. Chang. *J. Am. Chem. Soc.*, 128:12954–12962, 2006.

[36] F.C. Phillips. *Am. Chem. J.*, 16:225, 1894.

[37] J. Smidt, W. Hafner, R. Jira, J. Sedlmeier, R. Sieber, R. Rüttinger, and H. Kojer. *Angew. Chem.*, 71:176–182, 1959.

[38] J. Smidt, W. Hafner, R. Jira, R. Sieber, J. Sedlmeier, and A. Sabel. *Angew. Chem.*, 74:93–102, 1962.

[39] J. Smidt, W. Hafner, R. Jira, R. Sieber, J. Sedlmeier, and A. Sabel. *Angew. Chem. Int. Ed.*, 1:80–89, 1962.

[40] H. Nord. *Acta Chem. Scand.*, 9:430–437, 1955.

[41] E. Abel. *Monatsh.*, 87:354–358, 1956.

[42] A.S. Jhaveri and M.M. Sharma. *Chem. Eng. Sci.*, 22:1–6, 1967.

[43] B.C. Gates, J.R. Katzer, and G.C.A. Schuit. *Chemistry of Catalytic Processes*. McGraw-Hill Book Company, San Francisco, CA, 1979.

[44] P. M. Henry. *Palladium Catalyzed Oxidation of Hydrocarbons*. Catalysis By Metal Complexes. D. Reidel Publishing Company, Boston, MA, 1980.

[45] P.M. Henry. In E-I Negishi, editor, *Handbook of Organopalladium Chemistry for Organic Synthesis*, volume 1, pages 2119–2139. John Wiley & Sons, Inc., New York, NY, 2002.

[46] J. M. Takacs and X.T. Jiang. *Curr. Org. Chem.*, 7:369–396, 2003.

[47] J.-E. Bäckvall, B. Åkermark, and S.O. Ljunggren. *J. Chem. Soc. Chem. Comm.*, 8:264–265, 1977.

[48] B. Åkermark, B.C. Söderberg, and S.S. Hall. *Organometallics*, 6:2608–2610, 1987.

[49] V.V. Grushin. *Chem. Rev.*, 96:2011–2033, 1996.

[50] M.S. Sigman and M.J. Schultz. *Org. Biomol. Chem.*, 2:2551–2554, 2004.

[51] R. H. Crabtree. *The Organometallic Chemistry of the Transition Metals*. Wiley-Interscience, New York, NY, 3rd edition, 2001.

[52] P. M. Henry. *J. Org. Chem.*, 38:2415–2416, 1973.

[53] P. M. Henry. *J. Am. Chem. Soc.*, 86:3246–3250, 1964.

[54] M.N. Vargaftik, I.I. Moiseev, and Ya.K. Syrkin. *Izv. Akad. Nauk SSSR Ser. Khim.*, page 1144, 1963.

[55] I.I. Moiseev, O.G. Levanda, and M.N. Vargaftik. *J. Am. Chem. Soc.*, 96:1003–1007, 1974.

[56] H. Stangl and R. Jira. *Tetrahedron Lett.*, 41:3589–3592, 1970.

[57] J. K. Stille and R. Divakaruni. *J. Am. Chem. Soc.*, 100:1303–1304, 1978.

[58] J. K. Stille and D. E. James. *J. Organomet. Chem.*, 108:401–408, 1976.

[59] J. K. Stille and L. William. *J. Organomet. Chem.*, 169:239–248, 1979.

[60] D. E. James and J. K. Stille. *J. Am. Chem. Soc.*, 98:1810–1823, 1976.

[61] J.-E. Bäckvall, B. Åkermark, and S.O. Ljunggren. *J. Am. Chem. Soc.*, 101:2411–2416, 1979.

[62] J. A. Keith, J. Oxgaard, and W. A. Goddard. *J. Am. Chem. Soc.*, 128:3132–3133, 2006.

[63] W. K. Wan, K. Zaw, and P. M. Henry. *Organometallics*, 7:1679–1683, 1988.

[64] N. Gregor, K. Zaw, and P. M. Henry. *Organometallics*, 3:1251–1256, 1984.

[65] J.W. Francis and P. M. Henry. *Organometallics*, 10:3498–3503, 1991.

[66] C.M. Dumlao, J.W. Francis, and P.M. Henry. *Organometallics*, 10:1400–1405, 1991.

[67] J.W. Francis and P. M. Henry. *Organometallics*, 11:2832–2836, 1992.

[68] O. Hamed, C. Thompson, and P. M. Henry. *J. Org. Chem.*, 62:7082–7083, 1997.

[69] O. Eisenstein and R. Hoffmann. *J. Am. Chem. Soc.*, 103:4308–4320, 1981.

[70] H. Fujimoto and T. Yamasaki. *J. Am. Chem. Soc.*, 108:578–581, 1986.

[71] P. E. M. Siegbahn. *Struct. Chem.*, 6:271–279, 1995.

[72] P. E. M. Siegbahn. *J. Am. Chem. Soc.*, 117:5409–5410, 1995.

[73] Nelson D.J., R.B. Li, and C. Brammer. *J. Am. Chem. Soc.*, 123:1564–1568, 2001.

[74] P. E. M. Siegbahn. *J. Phys. Chem.*, 100:14672–14680, 1996.

[75] D.D. Kragten, R.A. van Santen, M. Neurock, and J.J. Lerou. *J. Phys. Chem. A*, 103:2756–2765, 1999.

[76] D.D. Kragten, R.A. van Santen, and J.J. Lerou. *J. Phys. Chem. A*, 103:80–88, 1999.

[77] P.J. Hay and W.R. Wadt. *J. Chem. Phys.*, 82:299–310, 1985.

[78] P. J. Hay and W. R. Wadt. *J. Chem. Phys.*, 82:270–283, 1985.

[79] J. M. Keith, R. J. Nielsen, J. Oxgaard, and W. A. Goddard. *J. Am. Chem. Soc.*, 127:13172–13179, 2005.

[80] R. J. Nielsen and W. A. Goddard. *J. Am. Chem. Soc.*, 128:9651–9660, 2006.

[81] R. J. Nielsen, J. M. Keith, B. M. Stoltz, and W. A. Goddard. *J. Am. Chem. Soc.*, 126:7967–7974, 2004.

[82] J.W. Francis and P. M. Henry. *J. Mol. Cat. A*, 112:317–326, 1996.

[83] B. Cornils and W.A. Herrmann, editors. *Applied Homogeneous Catalysis with Organometallic Compounds: A Comprehensive Handbook in Three Volumes.* Wiley-VCH, Weinheim, Germany, 2002.

[84] E.N. Jacobsen, A. Pfaltz, and H. Yamamoto, editors. *Comprehensive Asymmetric Catalysis*. Springer, New York, NY, 1999.

[85] A. Pfaltz and M. Lautens. In E.N. Jacobsen, A. Pfaltz, and H. Yamamoto, editors, *Comprehensive Asymmetric Catalysis*, volume 2, pages 833–884. Springer, New York, NY, 1999.

[86] I. Ojima, editor. *Catalytic Asymmetric Synthesis*. Wiley-VCH, New York, NY, 2000.

[87] D. C. Behenna and B. M. Stoltz. *J. Am. Chem. Soc.*, 126(46):15044–15045, 2004.

[88] J. Tsuji and I. Minami. *Acc. Chem. Res.*, 20:140–145, 1987.

[89] B. M. Trost. *Acc. Chem. Res.*, 29:355–364, 1996.

[90] B. M. Trost. *Chem. Pharm. Bull.*, 50:1–14, 2002.

[91] B. M. Trost. *J. Org. Chem.*, 69:5813–5837, 2004.

[92] B. M. Trost and C. Lee. In I. Ojima, editor, *Catalytic Asymmetric Synthesis*, pages 593–649. Wiley-VCH, New York, NY, 2000.

[93] B. M. Trost and D. L. VanVranken. *Chem. Rev.*, 96:395–422, 1996.

[94] G. Helmchen. *J. Organomet. Chem.*, 576:203–214, 1999.

[95] H. Steinhagen, M. Reggelin, and G. Helmchen. *Angew. Chem. Int. Ed.*, 36:2108–2110, 1997.

[96] D. K. Rayabarapu and J. A. Tunge. *J. Am. Chem. Soc.*, 127:13510–13511, 2005.

[97] F. K. Sheffy, J. P. Godschalx, and J. K. Stille. *J. Am. Chem. Soc.*, 106:4833–4840, 1984.

[98] F. K. Sheffy and J. K. Stille. *J. Am. Chem. Soc.*, 105:7173–7175, 1983.

[99] Y. Tsuji, M. Funato, M. Ozawa, H. Ogiyama, S. Kajita, and T. Kawamura. *J. Org. Chem.*, 61:5779–5787, 1996.

[100] J. A. Keith, D. C. Behenna, J. T. Mohr, S. Ma, S. M. Marinescu, B. M. Stoltz, and W. A. Goddard. *J. Am. Chem. Soc. ASAP*, 2007.

[101] G. Helmchen, H. Steinhagen, M. Reggelin, and S. Kudis. In H. Werner and P. Schreier, editors, *Selective Reactions of Metal-Activated Molecules*, pages 205–215. Vieweg Verlag, Wiesbaden, Germany, 1998.

[102] B. M. Trost and G. M. Schroeder. *Chem. Eur. J.*, 11:174–184, 2004.

[103] T. Hayashi, K. Kanehira, T. Hagihara, and M. Kumada. *J. Org. Chem.*, 53:113–120, 1988.

[104] R. Kuwano and Y. Ito. *J. Am. Chem. Soc.*, 121:3236–3237, 1999.

[105] M. Sawamura, H. Nagata, H. Sakamoto, and Y. Ito. *J. Am. Chem. Soc.*, 114:2586–2592, 1992.

[106] R. M. McFadden and B. M. Stoltz. *J. Am. Chem. Soc.*, 128:7738–7739, 2006.

[107] J. T. Mohr, T. Nishimata, D. C. Behenna, and B. M. Stoltz. *J. Am. Chem. Soc.*, 128:11348–11349, 2006.

[108] G. Helmchen and A. Pfaltz. *Acc. Chem. Res.*, 33:336–345, 2000.

[109] J. M. J. Williams. *Synlett*, pages 705–710, 1996.

[110] J. T. Mohr, D. C. Behenna, A. M. Harned, and B. M. Stoltz. *Angew. Chem. Int. Ed.*, 44:6924–6927, 2005.

[111] Y. Zhao, N. E. Schultz, and D. G. Truhlar. *J. Chem. Theory Comput.*, 2:364–382, 2006.

[112] Y. Zhao, N. E. Schultz, and D. G. Truhlar. *J. Chem. Phys.*, 123:161103–161107, 2005.

[113] W. Humphrey, A. Dalke, and K. Schulten. *J. of Mol. Graphics*, 14:33–38, 1996.

[114] N. Cohen and S. W. Benson. *Chem. Rev.*, 93:2419–2438, 1993.

[115] J. J. Low and W. A. Goddard. *J. Am. Chem. Soc.*, 108:6115–6128, 1986.

[116] J. J. Low and W. A. Goddard. *Organometallics*, 5:609–622, 1986.

[117] M. Méndez, J. M. Cuerva, E. Gómez-Bengoa, D. J. Cárdenas, and A. M. Echavarren. *Chem. Eur. J.*, 8:3620–3628, 2002.

[118] A. Ariafard and Z.Y. Lin. *J. Am. Chem. Soc.*, 128:13010–13016, 2006.

[119] M. García-Iglesias, E. Buñuel, and D. J. Cárdenas. *Organometallics*, 25:3611–3618, 2006.

[120] J. D. Sieber, S. B. Liu, and J. P. Morken. *J. Am. Chem. Soc.*, 129:2214–2215, 2007.

[121] S. R. Waetzig, D. K. Rayabarapu, J. D. Weaver, and J. A. Tunge. *Angew. Chem. Int. Ed.*, 45:4977–4980, 2006.

[122] O. A. Wallner and K. J. Szabo. *Chem. Eur. J.*, 12:6976–6983, 2006.

[123] R.P. Lutz. *Chem. Rev.*, 84:205–247, 1984.

[124] R. Sarpong, J.T. Su, and B. M. Stoltz. *J. Am. Chem. Soc.*, 125:13624–13625, 2003.

[125] J.T. Su, R. Sarpong, B. M. Stoltz, and W. A. Goddard. *J. Am. Chem. Soc.*, 126:24, 2004.